Journal of Pyrotechnics

Table of Contents - Issue 23, Summer 2006

Computer Modeling of Flying Star Ballistics

Dayu Ding, Morimasa Higaki, Yozo Ooki and Tadao Yoshida*

Ashikaga Institute of Technology,
268-1 Omae-cho, Ashikaga-shi, Tochigi 326-8558, KAPAN
Tel: +81-284-62-0605
Fax: +81-284-62-0976
E-mail yoshida@ashitech.ac.jp
*To whom all correspondence should be addressed.

Abstract*: The burning time of stationary and flying fireworks stars was measured, the trajectories of flying stars were observed and the results were analyzed in this work. It was found that the difference in burning time between the stationary and flying burning stars was dependent on the kind of star. Modeling of flying star ballistics was applied to the trajectory of stars with shorter burning times and was found valid for this case.*

Keywords*: fireworks, burning time, exterior ballistics, modeling*

Introduction

Firework stars with short burning times are used for warimono aerial shells giving spherical fire flowers, katamono aerial shells giving various burst shapes, Roman candles, and so on. The ballistics of stars with short burning times are important for designing warimono and katamono shells, Roman candles and others.

The present authors have suggested a computer model for estimating the trajectory of the burning star expelled from a mortar using a star with longer burning time.[1] In the present work, the model is applied to a flying star with a shorter burning time and the results are analyzed.

Computer modeling of aerial shells has been done by Kosanke and Kosanke,[2] and Mercer.[3] In the case of an aerial shell, the drag coefficient (C_D) can be assumed constant before the bursting of the shell in the air. But, in the case of a burning star, the above assumption is not valid, and an approximate approach was adopted in our previous work.[1]

Experimental

Materials

The silver peony stars for no. 2, 2.5, 3, 4 and 5 shells (a Japanese no. 2.5 shell corresponds to a Western 3 inch shell), lifting charge and electric matches were supplied by Sunaga Fireworks Co. Ltd. at Ashikaga City.

Grain black powder made by Nippon Kayaku Co. Ltd. was used as the lifting charge in our experiments. The standard and particle distribution of the lifting charge were described in our previous paper.[5]

Apparatus

The three kinds of mortar used for firing stars were made of steel, and the inner diameters were 12 mm, 15 mm and 20 mm, and depths were 216 mm, 270 mm and 360 mm, respectively.

The burning time and trajectories of stars were measured and recorded using a high-speed video camera (Phantom VR-V4.2).

Procedure

In stationary burning experiments, a star was placed on a heat resistant board and ignited by a torch. The stationary burning time of the star was determined using a high-speed video camera.

In star shooting experiments, the mortar was set on the ground vertically. An electric match was placed on the bottom of the mortar, the lifting charge was poured into the mortar from the muzzle, and then a star was placed on the lifting charge. The electric match was ignited by turning on an electric current. The star was shot into the air after the lifting charge burned.

The trajectory of the star was recorded by the high-speed camera. Each frame of the video was

reproduced on a video screen, and the burning time and the relationship between flying time and flying height of the star were determined.

Computer modeling of flying star ballistics[1]

Theory

The motion of a burning star expelled vertically in the air can be expressed as follows.

$$\frac{du}{dt} = -g - \frac{3\rho_{air}}{4\rho_{star}} \cdot \frac{C_D}{D_{star}} \cdot |u| \cdot u \qquad (1)$$

or

$$\frac{du}{dt} = -g - \frac{3\rho_{air}}{4\rho_{star}} \cdot K \cdot |u| \cdot u \qquad (2)$$

Here, u, t, g, ρ_{air}, ρ_{star}, D_{star} and C_D are star velocity, time, acceleration of gravity, air density, star density, diameter of the star and drag coefficient of air, respectively. The velocity u is positive when the star moves upward.

And

$$K = \frac{C_D}{D_{star}} \qquad (3)$$

It is assumed that the mass and cross sectional area of a burning star change but the density of the star does not change with time. Therefore, the second term of the right hand side of equation (1) for the air drag is proportional to the air drag coefficient C_D and inversely proportional to the diameter of the star D_{star} as expressed in equation (3).

K is obtained by the step by step calculation of the increment of the trajectory using equation (2). The diameter D_{star} of the star is a function of the flying time of the star and is calculated from the linear burning rate of the star:

$$D_{star} = D_{star0} - 2r_{star}t \qquad (4)$$

Here, D_{star0} and r_{star} are the initial diameter and the linear burning rate of the star, respectively.

Then, C_D is calculated from K and D_{star} using equations (3) and (4). It was found that C_D is nearly a linear function of time in the earlier stages of the trajectory and a scattered complex function of time in the later stages.[1] It was also found that in the low velocity range C_D of firework shells has little effect on the air drag.[4]

In our modeling of flying star ballistics, C_D is approximated as the linear function of time and expressed in equation (5):

$$C_D = at + b \qquad (5)$$

a and b in equation (5) are determined from the star shooting experiments and are used for estimating the trajectory of a burning star.

Results and Discussion

Stationary and flying burning times of stars

The mean burning time of the stationary and flying stars is listed in Table 1. In the previous experiments,[1,6] t_f/t_s were much larger than 1.0, but in this experiment, values of t_f/t_s were nearly 1.0. The differences may be attributable to the nature of the stars used.

Experimental and calculated results of the trajectories of stars

The experimental and calculated results of the trajectories of stars are listed in Table 2. The relative standard deviations of observed data were below 10% except for the initial velocity of the stars. The absolute values of the relative standard deviation of a are large because the mean values of a are very small. In this case the relative standard deviation has less meaning.

Fit of the calculated to the observed trajectory

All of the calculated trajectories were fitted to the observed ones. Examples are shown in Figure 1.

Effect of the kind of stars on *a* and *b*

In our previous work,[1] different values of a and b in equation (5) were obtained with the silver crown stars for no. 4 and no. 5 shells compared to those with silver peony stars in this work as listed in Table 3. The burning behavior may be different with different kinds of stars.

Table 1 *Mean burning times of the stationary and flying stars.*

Star	Stationary				Flying				t_f/t_s
	D_{star0} (mm)	Burning time(t_s) (ms)	SD	RSD	D_{star0} (mm)	Burning time (t_f) (ms)	SD	RSD	
Silver peony for									
No. 2 shell	10.27	2608	163	0.06	10.33	2751	126	0.05	1.05
No. 2.5 shell	11.19	2833	42	0.01	11.29	3311	197	0.06	1.17
No. 3 shell	12.13	3340	115	0.03	12.38	3389	318	0.09	1.01
No. 4 shell	13.30	3659	102	0.03	13.37	3464	153	0.04	0.95
No. 5 shell	14.91	3809	828	0.22	15.01	3967	138	0.03	1.04
No. 5 shell*	14.38	3822	195	0.05					1.00
Silver crown for									
No. 4 shell	16.57	4198		0.04	16.84	5701		0.05	1.4[1]
No. 5 shell	17.64	4646		0.04	17.62	6761		0.03	1.5[1]
Blue peony, silver peony and silver crown for No. 2–6 shells									1.6[6]

*Half the ignition promoter was scraped off and covered by an inhibitor. SD is standard deviation, and RSD (=SD/mean) is relative standard deviation.

Effect of the size and initial velocity of stars on *a* and *b*

The calculated results for stars from no. 2 (smallest) and no. 5 (largest) shells are shown in Figure 2. Values of C_D for the smallest star from a no. 2 shell increased with time and C_D of the largest from a no. 5 shell decreased with time. b in equation (5) was 0.46–0.53 with the smallest star from a no. 2 shell, while it was 0.55–0.63 for the largest star from a no. 5 shell.

Plots of a and b against the initial size and velocity of the stars are shown in Figure 3. The scatter of a of the stars for a no. 2 shell (runs 1–5) is abnormally large and the value for run 19 is also abnormally small. These data were excluded from the statistical consideration.

The correlations of a and b with D_{star0} and u_0 do not appear significant. Therefore, the mean values of a and b calculated from original data were −0.010 and 0.57, respectively.

The estimated trajectories of the burning silver peony stars using the above values of a and b are plotted against time in Figure 4 along with the observed trajectories.

Acknowledgement

The authors wish to gratefully acknowledge the experimental assistance of Sunaga Fireworks Company, Showa Rika Company, and the undergraduate students of Higaki Laboratory: Kashiwa, Arima, Ariga, Hukazawa and Morooka.

Table 2 *Experimental and calculated results on the trajectories of the silver peony stars.*

Run No.	ID of mortar (mm)	Lift charge (g)	Shell	Mass (g)	D_{star0} (mm)	u_0 (m s^{-1})	Burning time t_f (ms)	r_{star} (mm s^{-1})	$C_D = at + b$	
									a	b
1	12	0.5	No. 2	1.12	10.2	81		2.12	0.069	0.526
2	12	0.5	No. 2	1.05	10.2	61	2772	1.95	0.056	0.455
3	12	0.5	No. 2	0.94	9.8	61	2736	1.86	0.036	0.492
4	12	0.5	No. 2	1.16	10.9	62	2594	2.12	−0.001	0.528
5	12	0.5	No. 2	1.18	10.5	85	2901	1.87	0.036	0.512
Mean				1.09	10.3	70	2751	1.99	0.039**	0.503
SD				0.10	0.4	12	126	0.13	0.026	0.030
RSD				0.09	0.04	0.17	0.05	0.07	0.669	0.060
6	12	0.5	No. 2.5	1.46	11.3	87	3041	1.85	−0.001	0.490
7	12	0.5	No. 2.5	1.45	11.3	92	3478	1.62	−0.003	0.510
8	12	0.5	No. 2.5	1.40	11.2	100	3436	1.63	−0.006	0.571
9	12	0.5	No. 2.5	1.52	11.7	80	3288	1.78	−0.012	0.531
10	12	0.5	No. 2.5	1.36	11.0	86		1.74	−0.004	0.530
Mean				1.44	11.3	89	3311	1.73	−0.005	0.526
SD				0.06	0.3	8	197	0.10	0.004	0.030
RSD				0.04	0.02	0.09	0.06	0.06	−0.835	0.057
11	15	1	No. 3	2.02	12.6	76		2.30	0.000	0.610
12	15	1	No. 3	1.95	12.5	87	3808	1.85	−0.009	0.561
13	15	1	No. 3	1.90	12.5	93	3110	2.10	0.000	0.490
14	15	1	No. 3	1.89	12.3	95	3462	2.15	0.000	0.530
15	15	1	No. 3	1.85	12.1	94	3176	2.04	−0.008	0.571
Mean				1.92	12.4	89	3389	2.09	−0.004	0.552
SD				0.06	0.2	8	318	0.16	0.005	0.045
RSD				0.03	0.01	0.09	0.09	0.08	−1.327	0.082
16	15	1	No. 4	2.43	13.1	111	3300	2.09	−0.033	0.624
17	15	1	No. 4	2.61	13.6	86	3604	1.99	−0.014	0.612
18	15	1	No. 4	2.49	13.6	102		2.13	−0.005	0.601
19	15	1	No. 4	2.38	13.3	108	3488	2.15	−0.071*	0.595
20	15	1	No. 4	2.34	13.3	103		1.84	−0.003	0.590
Mean				2.45	13.4	102	3464	2.04	−0.014	0.604
SD				0.10	0.2	10	153	0.13	0.028	0.014
RSD				0.04	0.02	0.10	0.04	0.06	−1.110	0.023
21	20	2	No. 5	3.46	15.2	79	3950	2.20	−0.013	0.612
22	20	2	No. 5	3.36	14.7	91	3916	2.01	−0.015	0.592
23	20	2	No. 5	3.58	15.5	115	4198	2.01	−0.014	0.611
24	20	2	No. 5	3.34	14.7	88	3826	2.03	−0.024	0.635
25	20	2	No. 5	3.46	15.1	92	3944	2.04	−0.019	0.553
Mean				3.44	15.0	93	3967	2.06	−0.017	0.600
SD				0.10	0.3	13	138	0.08	0.005	0.031
RSD				0.03	0.02	0.14	0.03	0.04	−0.269	0.051
Overall mean									−0.010	0.560

* These data are omitted from the mean calculation. ** These data are omitted from the overall mean calculation.

Table 3 *Values of a and b in equation (5) for different stars.*

Kind of star	Mean diameter (mm)	Mean u_0 (mm s^{-1})	*a*	*b*
Silver crown star for				
No. 4 shell	16.8	159	0.359	0.259
No. 5 shell	17.5	167	0.352	0.275
Silver peony star for				
No. 4 shell	13.4	102	0.014	0.604
No. 5 shell	15.0	93	0.017	0.600

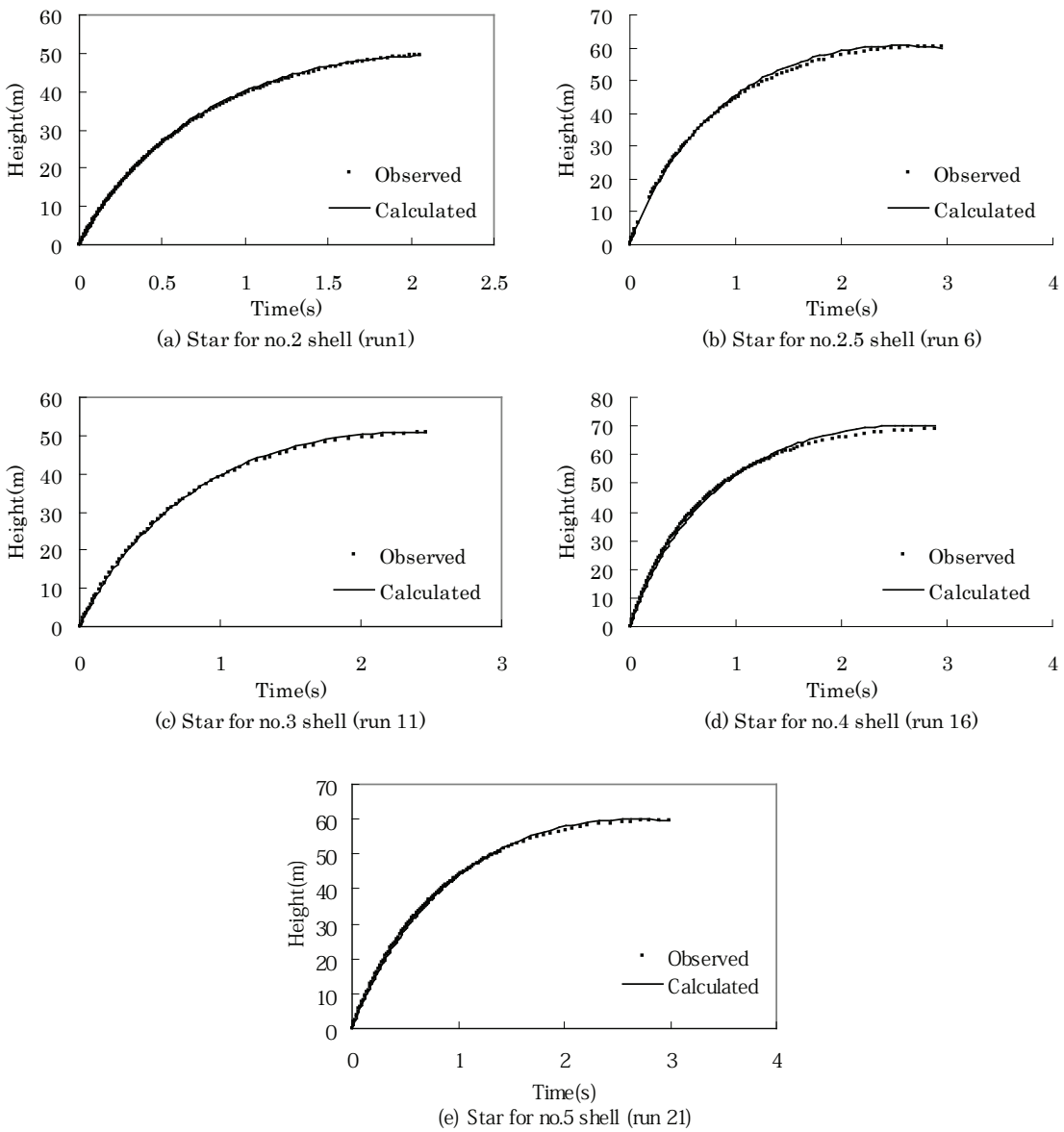

Figure 1 *Examples of the observed and calculated trajectories of burning stars.*

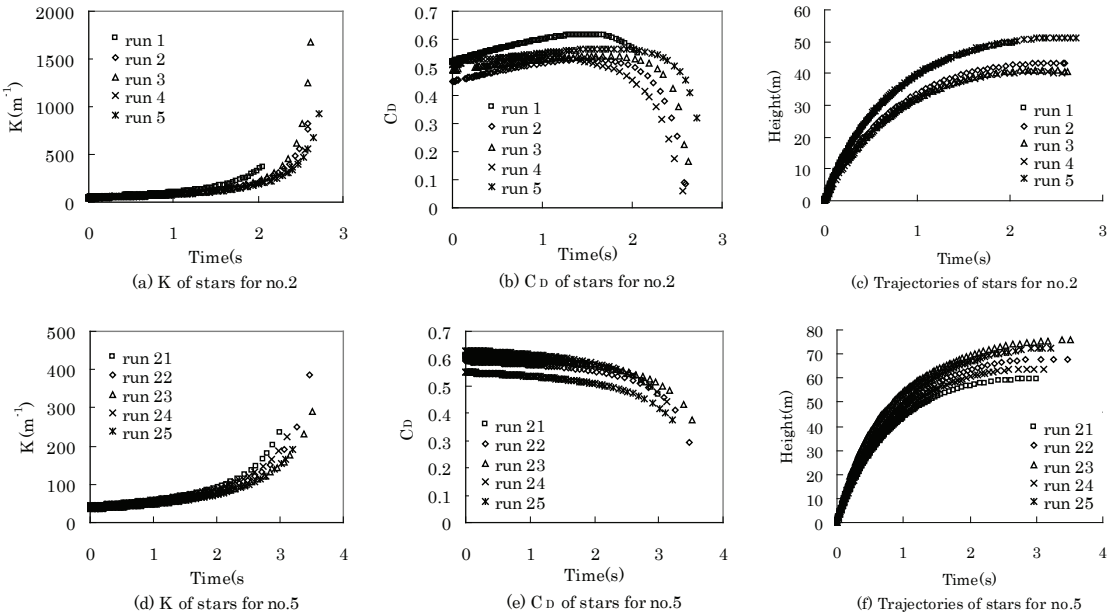

Figure 2 *Calculated K, C_D and flying height vs. flying time for no. 2 and no. 5 shells.*

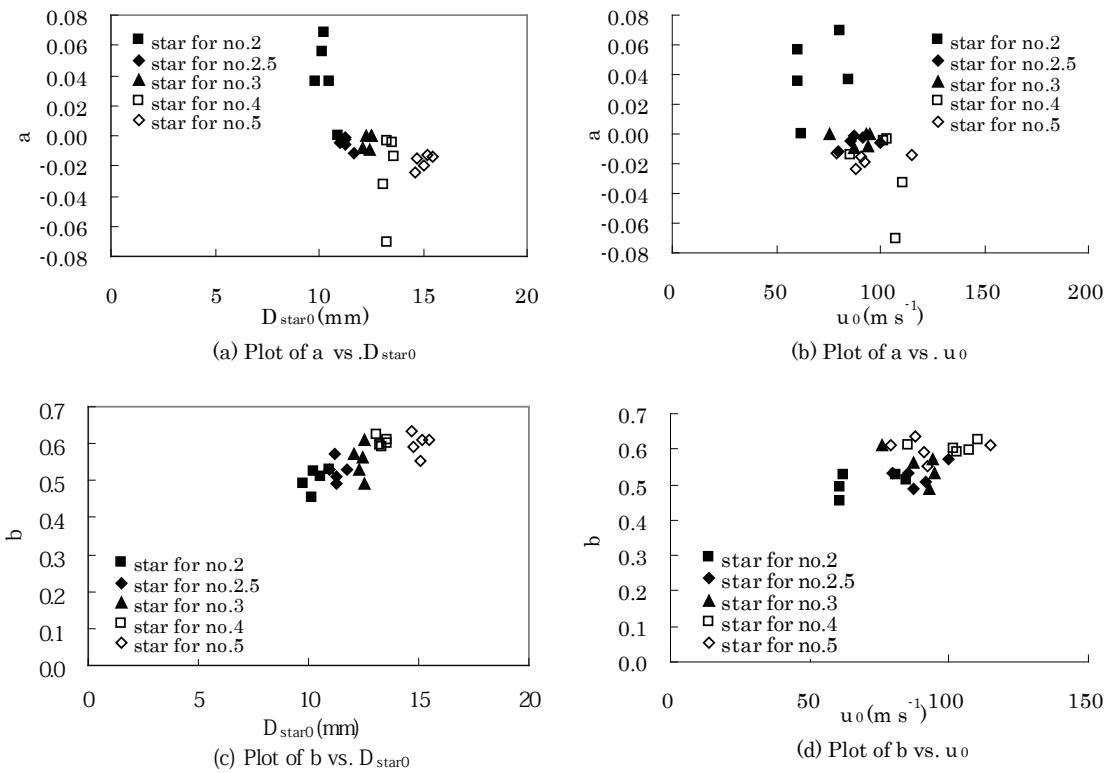

Figure 3 *Plots of a and b vs. the initial size and velocity of burning silver peony stars.*

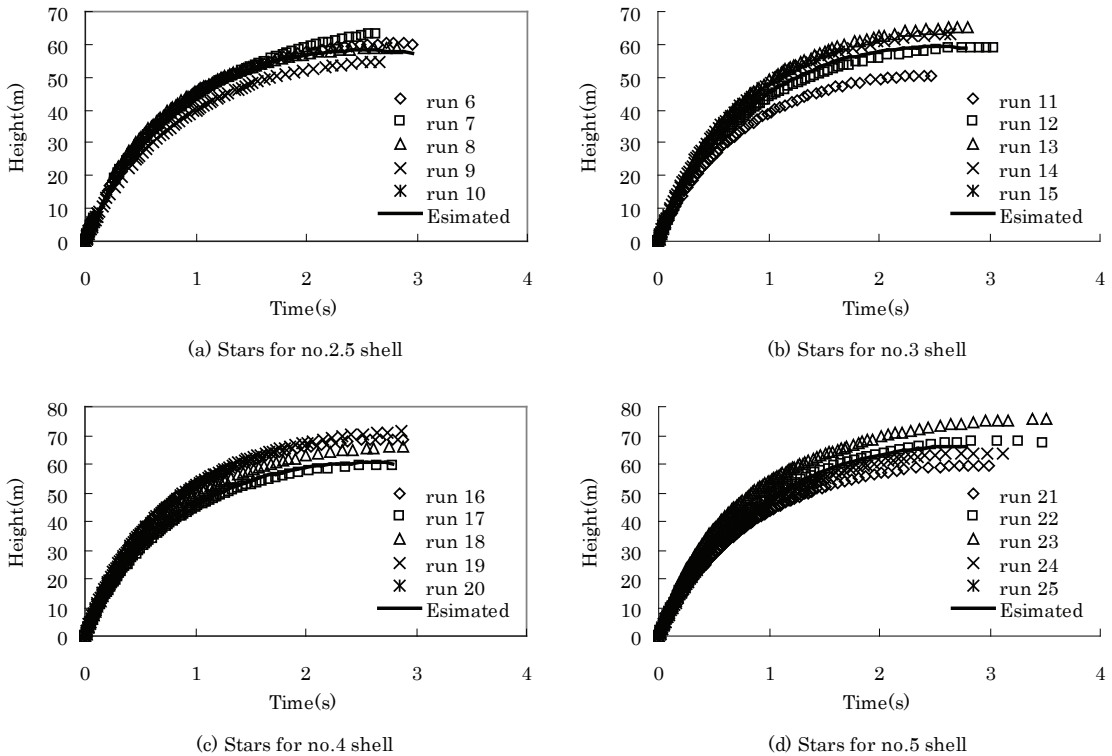

Figure 4 *Estimated and observed trajectories of burning stars.*

References

1 Y. Ooki, D. Ding, M. Higaki and T. Yoshida, "Trajectory of Stars with Long Burning Time", *Journal of Pyrotechnics*, in press.

2 K. L. Kosanke and B. J. Kosanke, "Computer Modeling of Aerial Shell Ballistics ", *Pyrotechnica*, XIV, 1992, p. 2.

3 J. E. Mercer, "Thermodynamics of Black Powder and Aerodynamics of Propelled Aerial Shells", *Journal of Pyrotechnics*, Issue 16, Winter 2002, p. 37.

4 Y. Ooki, D. Ding, M. Higaki and T. Yoshida, "Air resistance of Spherical Fireworks Shells", *Science and Technology of Energetic Materials*, in press.

5 D. Ding, M. Higaki, Y. Ooki and T. Yoshida, "Pressure in a Mortar and Estimation of Muzzle Velocity of Expelled Stars", *Journal of Pyrotechnics*, Issue 22, Winter 2005, p. 50.

6 Y. Ooki, D. Ding, M. Higaki and T. Yoshida, "Burning and Air Resistance of Fireworks Stars", *Science and Technology of Energetic Materials*, in press.

Temperature measurements within the luminous region of a burning $Ba(NO_3)_2$/Al mixture

P. J. Disimile, R. Prasad and N. Toy
UC-FEST, Department of Aerospace Engineering, University of Cincinnati, Ohio 45221, USA

Abstract: *Knowledge of the local temperature field associated with a pyrotechnic event has numerous implications, especially in the field of safety and survivability. These implications involve the development of sensors that are capable of detecting pyrotechnic events and that are used in part to eliminate or reduce a fire hazard. However, in order to be able to predict a possible fire scenario from a pyrotechnic event the temperature distributions and the thermal heat transfer are prerequisites. This experimental study discusses the temperature measurement methodology required to evaluate the transient temperatures associated with a small, commercially available, pyrotechnic device. Furthermore, the temperature distribution close to the surface of two devices, one commercial, the other fabricated, has been obtained, and shows that the temperature distribution away from the event is not uniform.*

Keywords: *Temperature distribution, thermocouples, pyrotechnic facility*

Introduction

The use of pyrotechnic compositions can be found in numerous fields like rocket propellants, highway flares, entertainment and other high-energy applications. Due to the release of a large amount of thermal energy, the burning composition and the events occurring around a pyrotechnic device are saturated by the intensity of emitted light. Hence a uniform region of light is observed which gives the impression of a fireball of constant temperature throughout. This is even more prominent when considering transient pyrotechnic events such as in the use of fireworks and incendiary devices. The measurement of the high temperatures that are produced by such near instantaneous chemical reaction is difficult to achieve and challenging to understand, and the ability to measure the temperature of a dynamic and transitory thermal field is far from trivial.

In order to be able to measure the expected high temperatures within the flash/fireball of a short duration pyrotechnic event a number of different techniques were considered. Of these, the most notable that have been used are optical pyrometers whereby the brightness of a flame has been compared to the brightness of an incandescent filament in order to determine the flame temperature.[1] Other types of pyrometers have also been used, but have not been successful, for example, cinephoto pyrometer, photoelectric photometer and a color photometer.[1] In comparison, temperature measurements of complex combustion within non-uniform temperature zones have been used successfully using a line-reversal methodology. However, this method only provides intermediate temperature distributions within the various zones of a flame and is dependent upon the emission of characteristic spectral lines from the flame as viewed by a spectroscope.[2] However, even in this latter method, the temperature measurements only accounted for the average temperature across a flame region and the variations within the inner zones were unaccounted for. Although temperature fields with relation to flame height have been measured using a cinephoto pyrometer,[1] detailed temperature distributions were unattainable since this method could not provide measurements at intervals less than 10 mm.

In order to satisfy the goals of the present study, it was considered necessary to adopt an approach of using high-speed thermocouples to capture the temperature distribution. Such temperature measurements have been performed earlier at a single fixed position in a closed system on different pyrotechnic materials, notably Sb/$KMnO_4$ (antimony/potassium permanganate),[3] and Pd/Al (palladium/aluminum) mixtures.[4] Temperature profiles have also been measured using W/Re (tungsten/rhenium) thermocouples for temperatures above 2000 ºC in Mo/$KClO_4$ (molybdenum/potassium perchlorate) material,[5]

and W/$KClO_4$/$BaCrO_4$ (tungsten/potassium perchlorate/barium chromate) material,[6] but again only at a fixed position in the system. Although bare bead W/Re type thermocouples are capable of measuring temperatures in excess of 2000 ºC, they are very prone to oxidation that can lead to large errors and have to be used within inert environments to prevent the tungsten from oxidizing.

The ability to measure and to analyze the dynamic thermal events surrounding a short duration pyrotechnic is problematical but it was not considered impractical if the temperature range of the apparatus could be obtained and if the thermal response was fast enough to record the event. Given these complications, it was decided to examine the capability of miniature high-speed thermocouples to observe the temperature distribution close to the surface of a pyrotechnic event. Two types of thermocouple were initially chosen for this study, an R- and a K-type which have the ability to measure maximum temperatures up to 1750 ºC and 1250 ºC respectively. A pyrotechnic event was created using, in the first instance, a common sparkler, and secondly a laboratory made device containing a chemical mixture similar to that of a commercial pyrotechnic material (CPM).

Experimental Strategy

Since thermocouples are available in different combinations of metals or calibrations it was necessary to select ones that were favorable to this study. The four most common types are J, K, T and E, with each type having a different temperature range and environmental usage, although the maximum temperature that each may record depends on the diameter of the wire used in the thermocouple. Given the harsh environment of the present studies, the following criteria were used in selecting a suitable thermocouple:

(1) Temperature range: The operating range of a thermocouple is the temperature range over which the thermocouple will perform satisfactorily, with negligible error in the output signal. For the current set of experiments, a temperature range with a high upper measuring limit was desirable.

(2) Thermocouple junction selection: Each thermocouple must utilize a measuring junction and a reference junction at two different temperatures. The measuring junction is generally at the higher of the two temperatures and the reference junction is at ambient. The measuring junction is placed near or on whatever is to be measured and the reference junction is connected either to a controller or a temperature indicator. Different kinds of measuring junctions are used with respect to measuring requirements as shown in Table 1. From this table it may be observed that for the present study an exposed bead weld, with a low thermal mass and corresponding fast response time, would be the most acceptable geometry for a thermocouple.

(3) Response time using first order response criteria: The time constant is the time required for the measured temperature to reach 63.2%

Table 1 *Effect of different thermocouple constructions.*

Type of junction		Response time	Advantages	Disadvantages
Sheathed	Ungrounded	Slow	Reliable and rugged construction	Sluggish response time
	Grounded	Normal	Useful for electrically conductive metallic sheaths	Noise injection
Exposed	Bead weld	Fast	Low thermal mass increases response time	Prone to damage in a corrosive environment
	Butt weld	Fastest	Useful in high speed measurements	Corrosive failure and physical or mechanical damage

of a step change in the temperature of the surrounding media. Five time constants are required for the sensor to approach 100% of the step change value. Typical response time for thermocouples range from milliseconds to seconds, depending on the size of the thermocouple, the fluid thermal conditions and the junction employed.

(4) Operating environment: The operating temperature and external environment can affect the performance of the thermocouple. The present test conditions required thermocouples whose output signals were not affected by any particulate from the flash/fireball scenario.

In order to record the temperature measurement from the selected thermocouple a dedicated acquisition system was used. This consisted of a 16-channel analog to digital data acquisition system with 12-bit resolution (National Instruments PXI - E6040E) that was connected to a stand-alone personal computer. LabVIEW software controlled the data acquisition program in such a way that different types of thermocouples could be accommodated using a single input channel. This approach was adopted so that the two types of thermocouple (R & K) could be tested through the same channel. Since the pyrotechnic event has to be captured within a short time period the data acquisition rate was set at 100 samples per second, with more than 1500 samples being recorded, depending on the test procedure.

It should be noted that initially a C-type thermocouple was also selected along with the R- and K-types because of their ability to withstand temperatures up to 2320 ºC. The material used in the construction of these different types of thermocouples consists of two wires of:

(a) platinum and the other platinum/rhodium alloy for the R-type,

(b) tungsten and rhenium alloy for the C-type, and

(c) chromel (a nickel chromium alloy) and alumel (a combination of nickel, aluminum, manganese and silicon) for the K-type.

However, from an initial investigation on the usage of a 0.217 mm (36-gauge) R-type thermocouple for measuring the surface temperature of a common sparkler both the C- and R-type thermocouples were discarded in favour of the K-type. The reason for this decision may be considered from the following study where a 40 mm length of a standard 2.8 mm diameter sparkler has been mounted horizontally on an aluminum support. A second aluminum plate supports an R-type thermocouple such that the thermocouple bead is in contact with the surface of the sparkler, Figure 1.

However, it should be noted that once a sparkler is ignited, Figure 2, the visible sparkling is created by the release of small iron particles that are distributed throughout its body and which may also be observed as physical protuberances

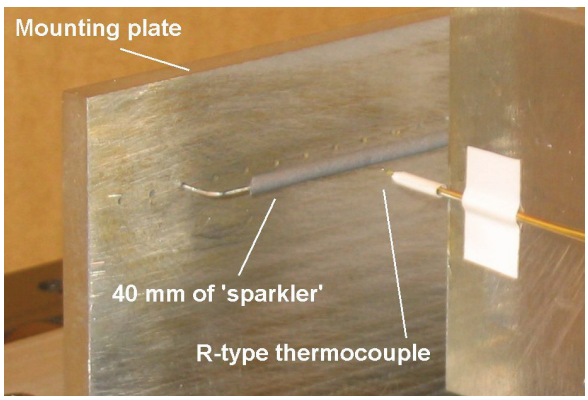

Figure 1 *An R-type thermocouple touching the surface of a horizontally held sparkler.*

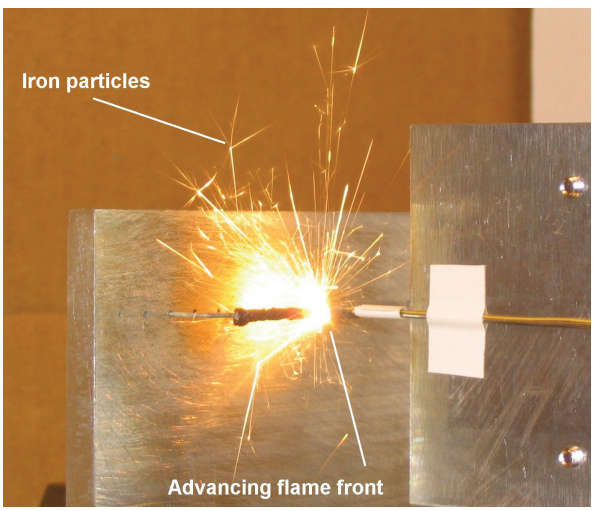

Figure 2 *An advancing flame front passes over the R-type thermocouple bead.*

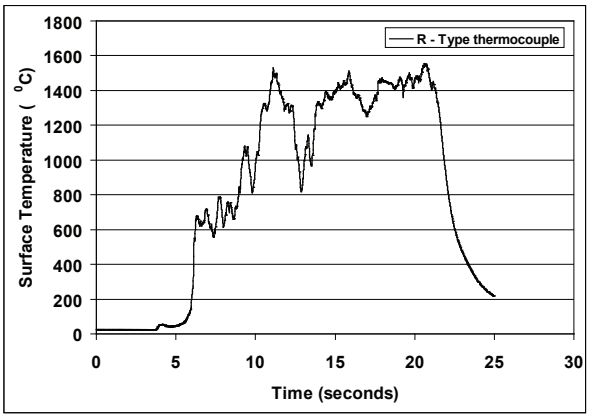

Figure 3 *Surface temperature of a sparkler using an R-type thermocouple.*

on its surface. In order that the thermocouple sensor could be located accurately against the sparkler surface these protrusions were removed before mounting the specimen in the supporting plate. As the flame front passes the thermocouple bead, the local surface temperature was recorded and a typical temperature–time plot is shown in Figure 3.

Here it is shown that as the flame front approaches the bead there is a rapid increase in temperature followed by series of temperature perturbations, reaching a maximum temperature of approximately 1575º C, before falling rapidly once the flame front has passed. These perturbations were considered related to the release of the small iron particles that, on their own, do not add to the heat generation but are likely to cause a local temperature fluctuation on their discharge. After considering the potential for large temperature errors to occur due to the contamination of the measuring bead at these high temperatures where the hot gases produced by the reaction cannot be controlled, a decision was made to discard their use in favour of the K-type thermocouple.

Similarly, a 0.217 mm (36-gauge) bare bead, unsheathed, C-type thermocouple was also examined, and not selected. Every attempt to sheath the bare wires resulted in damage to the thermocouple near the bead, due to the brittle nature and associated difficulty in handling of the wires. Furthermore, the tungsten wire required an inert atmosphere, since it also quickly oxidized at high temperatures.

The thermocouple eventually chosen was a 0.0787 mm diameter (40 gauge) K-type with an exposed bead weld junction. This thermocouple consists of two wires, which are insulated from each other except in the region of the bead, placed inside a sheath of 0.0762 mm thickness. The positive wire is made of chromel, which is a composition of 90% nickel and 10% chromium, and the negative wire is made of alumel, a composition of 95% nickel, 2% aluminum, 2% manganese and 1% silicon. The advantages of using the K-type thermocouples are:

(1) They have the highest temperature range (−200 ºC to 1250 ºC) among the most commonly used types of thermocouples.

(2) They could be fabricated within the laboratory. This was achieved by using pre-insulated wire and removing a 15 mm length of insulation from each. The exposed wires were then twisted and welded into a small bead in a thermocouple welder.

When the welded connection (bead) of a thermocouple is heated, a voltage across the two junctions is produced. A polynomial equation is then used to convert the thermocouple voltage (E) to a temperature (T/ºC) over a wide range of temperatures and is given by the equation based on the International Temperature Scale (ITS–90) standard:

$$T_{90}(E) = \sum_{i=0}^{N} d_i E^i$$

where the coefficients, d_i are as given by the National Bureau Standards in Table 2 below for K-type thermocouples.[7]

Time response evaluations of the K-type thermocouple

In order to be able to determine the time response of the chosen thermocouple a 50 mm × 50 mm square shock tube arrangement was used. The shock tube consisted of two sections, a closed high-pressure driver section and an open ambient pressure driven section, with a thin plastic diaphragm separating the two sections. By filling the driver section with high-pressure air until the plastic diaphragm bursts a shock, or blast, wave is produced that may travel at speeds greater than

Table 2 *Polynomial coefficients for ITS-90 standard.*

Type K polynomial coefficients	Value
i	d_i
0	0.226584602
1	24152.10900
2	67233.4248
3	2210340.682
4	−860963914.9
5	4.83506×10^{10}
6	-1.18452×10^{12}
7	1.38690×10^{13}
8	-6.33708×10^{13}

the speed of sound (approximately 330 m s^{-1} in air at standard temperature and pressure) through the driven section of the tube. At the exit of the driven section of the shock tube a small heat source (flame) is positioned with the test thermocouple situated close to its core such that it measures the local flame temperature. When the shock wave exits the driven section the flame is extinguished and the thermocouple experiences a step change in temperature from that of the flame (approximately 466 ºC) to that of the ambient temperature (approximately 21 ºC), Figure 4. The response time of the thermocouple is the time taken for the temperature to drop from the maximum temperature (T_{max}) to 63.2% of the final temperature. Several 0.0785 mm (40-gauge) K-type thermocouples were evaluated and their time constants determined to be approximately 10 ms.

Sparkler temperature profile analysis

Initially, tests were performed on commercially available sparklers that had a nominal diameter of 2.8 mm and prepared to a length of 40 mm, and located horizontally in the apparatus shown in Figure 1. Since the surface temperature was known to be as high as 1575 ºC, as measured previously with an R-type thermocouple, the locations of the K-type thermocouple were examined and it was concluded that they should be positioned no closer than 1.2 mm from the sparkler surface, and a typical temporal profile is shown in Figure 5. Here, it may be observed that as the flame approaches the thermocouple bead there is a steady rise in temperature until the flame is adjacent to the thermocouple where the maximum temperature is recorded. Once the flame passes the thermocouple the temperature falls to ambient conditions. However, due to the instability and pulsating nature of the flame an oscillation in the temperature profile can also be noted in this Figure.

Wasmann[8] previously observed this fluctuating behavior of a pyrotechnic system and provided the explanation that two major factors were responsible for this action:

(1) The competition between the various chemical reactions within the pyrotechnic composition.

(2) Physical factors like heat loss, heat accumulation, and the intermittent vaporization

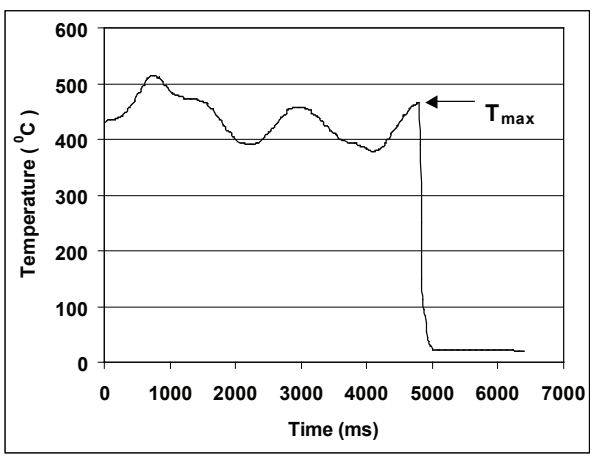

Figure 4 *Thermal time response for a 40-gauge K-type thermocouple.*

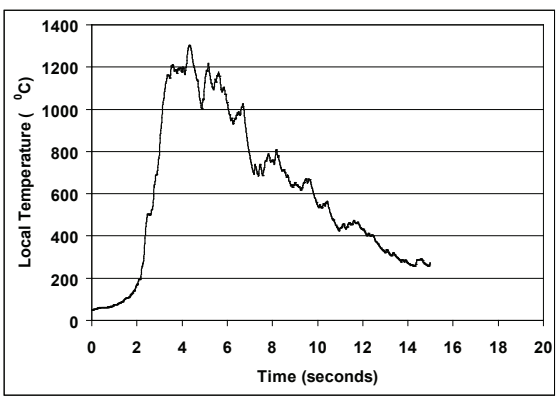

Figure 5 *Temperature profile taken 1.2 mm away from a sparkler surface.*

processes in the test composition.

In the first case, the pulsating flame behavior occurs as a result of competition in the chemical reaction and this may be explained as oscillations between light and dark cycles that occur when the composition consists of two or more different fuels. The quick reacting fuel reacts with the oxidizer releasing little energy in the form of light, hence representing a relatively dark cycle, whereas the light cycle is caused by large energy releases from the oxidation of the slow reacting fuel thereby producing large quantities of visible light. The rate of oxidation of the slow reacting component increases rapidly after the dark cycle due to the increase in the reaction surface area, and also due to the presence of oxidative gases from the dark cycle, trapped in the micro-porous structure of the surface. This dual cycle process seems to cause the pulsations in reactions with multiple fuel components, and with variable rates of reaction. In the case of sparklers, clear dark and light zones were not observed; however, the intensity of the emitted light could be seen to vary, and this pulsating behavior is observed as a change in emitted light intensity. In the chemical composition of the sparkler, the effect of the minor components has not been considered although these minor components may also affect the reaction rate by reacting with the oxidizer, thereby resulting in the dark phase of the pulsation cycle.

In the second case, the undulating nature of the temperature profile may be explained by the rapid heat loss from the surface following the release of an iron particle. This rapid thermal change would be sufficient to instantaneously lower the local temperature. Once the particle was released the surface temperature would again return to a quasi-steady state where the local temperature would attempt to return to its original value, albeit lower in value because of the passing of the flame front, before the release of another iron particle. The rate of release of the iron particles would provide the fluctuations in the temperature profile.

Although other physical properties like viscosity and volatility can also affect the burning process to create a pulsation effect as explained by Gol'binder and Goryachev,[9] they were not considered in this study since there are no volatile components involved in the formation of the standard sparkler.

In order to determine the temperature distribution around the surface of the sparkler, measurements were taken of the maximum attainable temperature at discrete locations in the $+x$, and $+z$ and $-z$ directions, where $+x$ refers to the horizontal distance radially away from the sparkler surface, and the $+z$ and $-z$ directions refer to the upper and lower vertical distances away from the sparkler surface respectively. Figure 6 shows diagrammatically the coordinate system adopted for these sets of measurements. These maximum temperatures were obtained in the three directions from more than 120 individual tests for a range of positions, from 1.15 mm to 2.5 mm in increments of 0.05 mm in the $+x$ direction and 0.10 mm in the $+z$ and $-z$ directions, Figures 7 and 8.

Although there is a large amount of scatter in the results, mainly due to the small differences in the composition of the charges, and the location of the thermocouple in relation to the sparkler surface, there is a distinct trend in the temperature distribution. From Figures 7 and 8, it may be observed that a drop in temperature occurs between 1.2 mm to 2.5 mm in both the x and z directions. Comparing the curve-fitted temperature profiles in the x and z directions, it may also be observed that the drop in the temperature in the z (vertical) directions is estimated to be some 170 ºC mm^{-1},

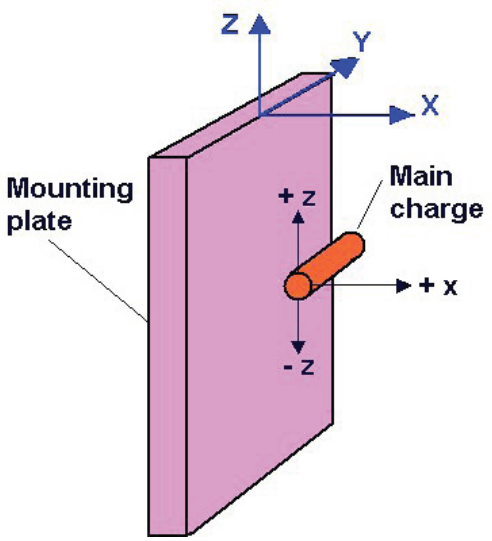

Figure 6 *Coordinate system for the measurement of temperatures from the main charge (sparkler).*

whereas in the x (horizontal) direction the fall in temperature is approximately 3 times greater. Furthermore, the temperature profiles shown in Figure 8 suggest that the thermal gradient in the $+z$ direction is less than that in the $-z$ direction, and may be explained by the following:

(1) As the pyrotechnic materials melt in the reaction zone they tend to flow producing a downward shift in the sparkler's position due to its weight before complete combustion can occur. This effect reduces the distance between the thermocouple and the reacting pyrotechnic surface becoming more pronounced when the linear burning speed of the reaction zone, as it moves along the test sample, is low. In the current condition a burn speed of 2 mm s^{-1} was recorded.

(2) Effect of natural convection on the thermal field; similar to that observed around a heated horizontal cylinder by a Schlieren technique.

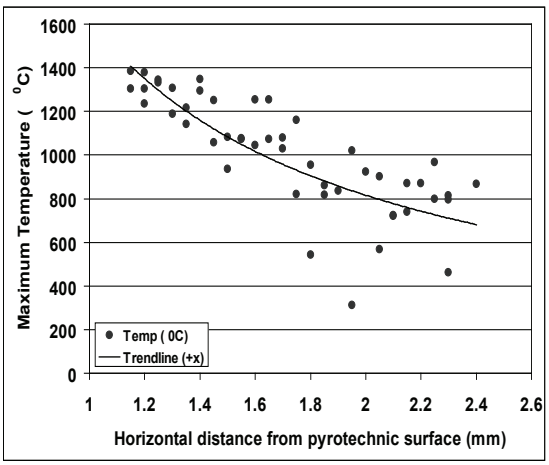

Figure 7 *Temperature distribution in the horizontal + x direction.*

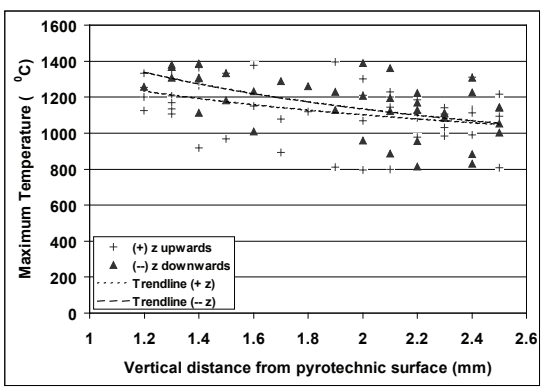

Figure 8 *Maximum temperatures above and below the sparkler surface.*

One of the difficulties of using standard sparklers was that of igniting the specimen accurately at a preset time. To overcome this obstacle, an electric match was formulated from two pyrotechnic components and attached to a main charge fabricated from sparkler material.

Test charge composition

The pyrotechnic material used in the main charge was obtained from commercial sparklers without the addition of the iron particles. The reason for removing these particles was to reduce the fluctuations in the temperature measurements previously observed and shown in Figures 3 and 5. This was achieved by crushing the sparklers into a fine powder and removing the iron particles with an electric magnet. The powder was then mixed with a chemical binder (dextrin) and moulded into a test charge, referred to as a commercial pyrotechnic material (CPM), The composition of this charge is given in Table 3: barium nitrate makes up 74% of the charge, and aluminum 24%, with 2% taken up with a chemical binder (dextrin).

Since it was intended to ignite the test charge in a more systematic manner, an electric match was fabricated with the main test charge. The pyrotechnic composition of the electric match is shown in Table 4: the oxidizer was potassium chlorate and the fuel was powdered lead thiocyanate. To hold the pyrotechnic compositions together a binder (dextrin) was again utilized.

Test charge fabrication

Once the main charge comprising the barium nitrate, aluminum and its binder was thoroughly mixed, it was pressed into a small cylindrical mould that had an internal diameter of 4 mm diameter, and was 15 mm long, for a length of 12 mm, with the remaining 3 mm allocated to the material for the 'electric match'. A steel support bar, 60 mm in length and 2 mm in diameter was then pushed through the mixture along the axis of the mold. An electric heating element consisting of a 50.8 mm long, 0.16 mm diameter (34-gauge)

Table 3 *Chemical formulation of commercial pyrotechnic material.*

Charge	Chemical	Formula	Quantity (by wt)	Mesh size
Main charge (CPM)	Barium nitrate	$Ba(NO_3)_2$	74%	<200
	Aluminum	Al	24%	<200
	Binder (dextrin)	$(C_6H_{10}O_5)_n$	2%	<200

Table 4 *Chemical composition of electric match.*

Charge	Chemical	Formula	Quantity (by wt)	Mesh size
Electric match	Potassium chlorate	$KClO_3$	55%	<200
	Lead thiocyanate	$Pb(SCN)_2$	44%	<200
	Binder (dextrin)	$(C_6H_{10}O_5)_n$	1%	<200

nichrome wire with a resistance of 2.73 ohm was wrapped around the support bar but isolated from it by a small piece of electrical insulating tape. The electric match mixture was then pushed into the remaining 3 mm part of the mold encompassing the electrical element such that the flat surface of the match composition is in contact with the composition of the main charge, around which the temperature distribution was to be measured. The complete test charge was then allowed to dry for 24 h and then removed from the mold. Ignition of the test charge was accomplished by igniting the electric match using the heating element connected to a 5 V DC power supply. Figure 9 is an image of the complete test charge showing the main charge, electric match, support bar and the electrical leads of the heating element.

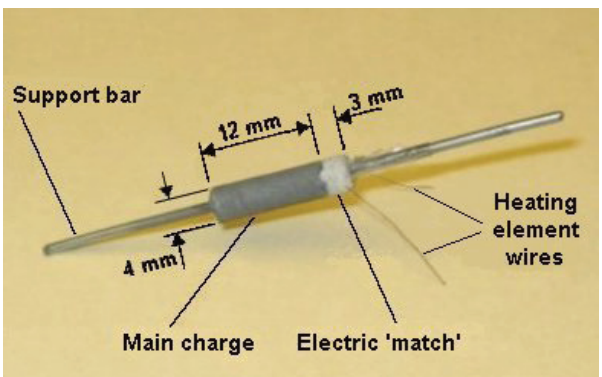

Figure 9 *Image of fabricated CPM charge from sparkler material.*

Testing facility

In order to improve the ability to locate a thermocouple bead away from the surface of the test charge with more accuracy a 3-dimensional traversing mechanism was constructed, Figure 10.

The base of the main traverse section supported the test charge holder, test charge, and three micrometer controlled slides to which three separate thermocouples could be mounted. The slides were configured to provide accurate independent

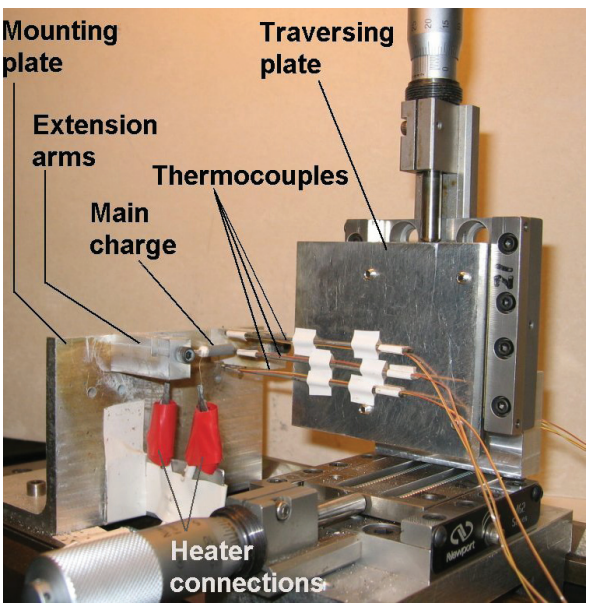

Figure 10 *Facility for accurately positioning thermocouples close to the main charge.*

movement in three orthogonal directions (x, y, z), with a spatial resolution in each direction of 1 micron. To allow the test charge to be rigidly fixed in space a separate aluminum mounting plate was utilized, and two extension arms added ensuring that the test charge was mounted off the plate by approximately 40 mm, Figure 10. In addition, a second flat rectangular traversing block was attached to the vertical segment of the traverse and acted as the base for multiple thermocouple attachment, as shown in Figure 10, thereby allowing multiple measurements to be made for any one test.

CPM temperature profile measurements

With a test charge mounted in the extension arms of the mounting plate an electrical connection to a 5 V DC power supply can be made to initiate the ignition process. Temperature measurements were taken using three K-type thermocouples arranged so that measurements could be obtained in the x-direction, and the $\pm z$ directions simultaneously at precise horizontal and vertical locations, Figure 6.

In this phase of the study the flame of the pyrotechnic was larger than the 2.8 mm diameter sparkler, which resulted in the burnout of the K-type thermocouples at approximately 2 mm from the surface of the test piece. Therefore in order to prevent continual thermocouple failure a larger standoff distance was utilized when compared to the 2.8 mm diameter test charge. Figure 11 shows three temperature profiles around a 4 mm diameter test charge and it can again be observed that nearer the surface of the test charge, the magnitude of the temperature profile beneath the burning pyrotechnic (in the $-z$ direction) is larger than that above the charge (in the $+z$ direction), a trend similar to that found for the 2.8 mm diameter test species. However, the most striking feature of this data set is that the drop in temperature away from the burning test charge falls in a tight band with a nominal 200 ºC spread for all three directions, providing a temperature decay of approximately 240 ºC mm^{-1} over the distances measured. This is in contrast to the results found for the 2.8 mm diameter sparkler. However, there are small differences between the data sets and it may be inferred that the maximum decreases in temperature for all the three orientations occur in the x directions. The minimum drop may be observed in the $+z$ direction and the reason may be attributed to the flow of gases, due to natural convection, in this direction. The temperature drop in the $-z$ direction is between the temperature drop values in the other two directions, but below that for the $+z$ direction. The reasons for this relatively lower temperature drop in the $-z$ direction can be attributed to interference with natural convection from jet-like ejections, not related to the emission of iron particles.

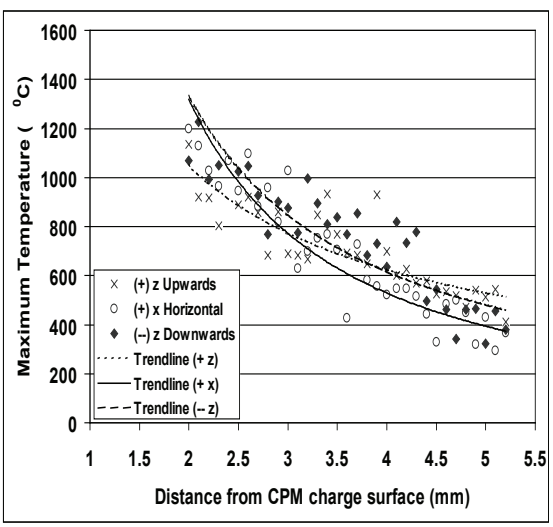

Figure 11 *Temperature distributions around a 4 mm diameter CPM charge.*

The primary reason for the scatter in the data was due to the slight uncertainty in thermocouple position and the continuous pulsations in the flame when the premixed composition burned. Other factors that influence data scatter are related to the following initial assumptions:

- Each test piece has the same density/ composition.
- Burning is uniform – following a ring-like pattern along the length of the test piece.
- Each test piece is unaffected by external conditions.

Although care was taken to maintain constant weight of each test charge, their weights varied within ±2% error. Similarly while compacting the composition into the mold shell, attempts were made to maintain the dimensions to within ±2%, thereby keeping the test charge final density to

Table 5 *Heat of formation for different chemical products.*

Chemical formula	Chemical name	Heat of formation ΔH_f /kJ mol^{-1}
$Ba(NO_3)_2$	Barium nitrate	−992
Al	Aluminum	0
BaO	Barium oxide	−548.1
Al_2O_3	Aluminum oxide	−1675.7
N_2	Nitrogen gas	0

within a couple of percent.

Furthermore, it was assumed that the ignition of the main charge occurred instantaneously from the initiator (electric match) with the resulting flame propagating uniformly through the entire cross-section of the main charge. In the absence of pulsations a ring-like burning pattern was assumed. However, if the flame does not cover the entire cross-section, an irregular burning pattern results and this can be exacerbated by the difference in the surface burning speeds. It was also assumed that changes in the ambient conditions, such as variations in temperature and forced convection, were small enough to be neglected.

It should also be noted that no temperature corrections due to conduction, convection and radiation have been applied to these measurements since it was considered that any error analysis would have been dependent on the thermal conductivity of the wires (k), the convective heat transfer coefficient (h) and the emissivity (ε) of the thermocouple sensor element. This dependence would have relied upon a steady state energy balance, a condition that was inappropriate for this dynamic situation. Furthermore, due to the gaseous nature of the pyrotechnic event, the convective heat transfer coefficient could not have been accurately determined; neither would the emissivity of the thermocouple bead be a single value due to the heating and cooling nature of the event discolouring the bead surface. However, as an approximation, a conduction error has been estimated from a simple energy balance between the net heat conducted along the wires and the heat convected to the wires. This analysis forms a simple second order differential equation that can be solved for the sensor temperature. For example, for a thermal conductivity of 24 W m^{-1} deg^{-1} for the wires, and 45.4 W m^{-1} deg^{-1} for the convective heat transfer coefficient, an error in the measurement of a bead temperature of 1200 ºC would have been approximately 130 ºC, an error of some 10.8%. Likewise, an error in the temperature of the bead due to radiation has been estimated from a simple steady state energy balance between the convection heat transfer and the radiation transfer. This was achieved by using the above value for the convection heat transfer coefficient, and an emissivity value of 0.07 for a K-type (chromel/alumel) thermocouple, where it was found that the error in the temperature was approximately 1860 C, or 15.5%.

Summary

This work has shown that the near surface temperatures of a pyrotechnic charge may be measured accurately with miniature high-speed K-type thermocouples. Temperatures approaching 1600 ºC were recorded at the surface of a 2.8 mm sparkler using an R-type thermocouple, while temperatures over 1300 ºC were being measured 1.2 mm away from the sparkler surface using K-type thermocouples.

In the case of a standard sparkler the temperature distribution may be measured as close as 1.2 mm to the surface, whereas for the 4 mm diameter charge, made from the same material, the thermocouples could not be placed within 2.0 mm of the surface without a total failure.

When comparing Figures 7 and 8 for the 2.8 mm diameter sparkler to Figure 11 for the 4 mm charge, the temperature decay for the sparkler appears to have directional dependence and falls off more slowly than that for the 4 mm charge. It was also found that for the 2.8 mm sparkler the temperature decay in the vertical direction was approximately

30% lower compared to the temperature decay in the horizontal direction. This suggests that the heat liberation rate for the 2.8 mm charge was insufficient to overcome the energy transport by natural convection and thereby resulted in lower levels of thermal energy propagated in the horizontal direction.

The temperature around a 4 mm diameter test charge fabricated from commercially available pyrotechnic material has shown that, although there is a difference in the thermal energy being released in different directions, this difference is small compared with that obtained from the 2.8 mm sparkler, and that the temperature falls off in a tight band of approximately 200 ºC.

References

1 A. A. Shidlovskiy, *Principles of pyrotechnics*, 3rd edition, 1964, English text prepared from translations by staff of *American Fireworks News*, Rex E. & S.P. Inc, 1997.

2 H. M. Strong, F. P. Bundy and D. A. Larson, "Temperature measurement on complex flames by sodium line reversal and sodium D line intensity contour studies", *3rd Symposium on Combustion and Flame and Explosion Phenomena*, 1949 , pp. 641–647.

3 M. W. Beck, "Temperature profile analysis of the Sb/$KmnO_4$ system", 14th International Pyrotechnics Seminar, Jersey, UK, 1989, pp. 433–442.

4 M. R. Birnbaum, "Determination of Pd/Al reaction propagation rates and temperatures", 6th International Pyrotechnics seminar, Colorado, USA, 1978, pp 39–61.

5 G. Pan, J. Hao, D. Jiang, and B. Su, "Measuring combustion temperature of high temperature (2000–2800 deg C) pyrotechnic compositions on W–Re thermocouple", 19th International Pyrotechnics seminar, Christchurch, NZ, 1994, pp. 52–56.

6 Y. L. Lao and P. Wang, "A study of pyrotechnic delay system and analysis of temperature profile", 13th International Pyrotechnics seminar, Colorado, USA, 1988, pp. 537–544.

7 T. J. Quinn, *Temperature*, Academic Press Inc., 1990.

8 F. W. Wasmann, "The phenomenon of pulsating burning in pyrotechnics", 5th International Pyrotechnics Seminar, Colorado, USA, 1976.

9 A. I. Gol'binder and V. V. Goryachev, "Pulsatory combustion of liquid explosives thickened with dissolved polymers", *Russian Journal of Physical Chemistry*, vol. 35, no. 8, 1961, pp. 889–891.

Ballistics of an Iron Bar Shot from a Mortar

Morimasa Higaki, Dayu Ding, Yuuzo Ooki and Tadao Yoshida*
Ashikaga Institute of Technology
268-1 Omae-cho, Ashikaga-shi, Tochigi-ken 326-8558, Japan
Phone: +81-284-62-0605
Fax: +81-284-62-0976
E-mail: yoshida@ashitech.ac.jp
*To whom all correspondence should be addressed.

Abstract*: An accidental explosion in 1848 in the USA became a trigger for the development of neuroscience. An accidental explosion of black powder took place in a borehole for blasting and the expelled iron bar penetrated the head of a young man. He was injured but survived for 12 years. The authors were asked to calculate the speed, impact pressure or energy of the explosion by the producer of a TV program. At the time we were carrying out similar experiments using a mortar and firework stars, and so a model experiment was performed. Here we report of the results.*

Keywords*: black powder, ballistics, iron bar, shot energy efficiency*

Introduction

An accidental explosion involving black powder became a trigger for the development of neuroscience. On September 13, 1848, at a blasting site in Vermont, USA, Phineas Gage, a young man of 25 years old, was involved in an accident.[1] He accidentally dropped an iron tamping bar 6.1 kg in mass, 3.2 cm in diameter and 110 cm in length into a borehole 3.8 cm in diameter and 91 cm deep filled with about 0.4 kg black powder. An explosion took place, and the bar was shot from the borehole and penetrated his head from his left cheek to the top of his head. Amazingly he escaped death and survived for twelve years after the accident.

Twenty years after the accident, Gage's physician, John Harlow, perceptively correlated Gage's cognitive and behavioral changes with a presumed area of focal damage in the frontal region. His observation made considerable scientific impact and gave rise to controversy. Gage's skull was recovered and is in the Warren Anatomical Medical Museum at Harvard University.[2]

We were asked by the producer of a television program to calculate the velocity of the iron bar, the pressure of the bar on his brain, and the power of the explosion. In response to his request we carried out a small scale experiment using a mortar for firework star shots and a pressure measuring apparatus[3] and the results were analyzed as before.[4]

Experimental

Materials

The grain black powder and electric match were made by Nippon Kayaku Co. Ltd. This black powder may be similar to the black powder used in blasting 160 years ago in the USA. Howard[5] shows that the black powder manufacturing process has not changed in principle from *ca.* 1780 until now. Van Gelder and Schlatter[6] wrote in 1927 that blasting powder was made in very much the same way as gunpowder.

Apparatus

The iron bar is 1.5 kg in mass, 22 mm in diameter and 506 mm long. The mortar is shown in Figure 1. The inner diameter, wall thickness and depth of the mortar were 25 mm, 2.5 mm and 460 mm, respectively. The gap ratio in this case was 29%. The gap ratio GR (%) is defined as follows:

$$GR = \frac{S - s}{S} \times 100$$

Here, S and s are the cross sectional areas of the mortar and the bar, respectively.

Two pressure sensors were fitted, to the bottom and to a position 300 mm from the bottom of the mortar. The mortar was fixed on an H-shaped steel holder as shown in Figure 2.

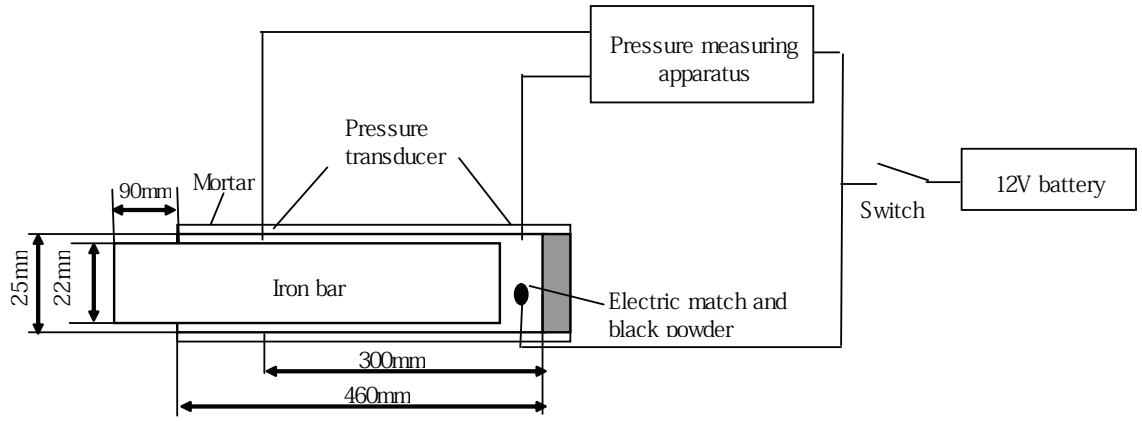

Figure 1 *Mortar and bar. The pressure in the mortar during the shot was measured and recorded using two pressure sensors (Kistler 60410A), charge amplifiers (Kistler 5011) and a digital oscilloscope (Sony Tektronix 5011).*

Procedure

The mortar was set on the ground vertically. The black powder and electric match were put in the bottom of the mortar. Then, a piece of tissue paper and the iron bar were inserted into the mortar slowly. The mortar fixed to the holder was set on the ground horizontally. The mortar was covered by U-shaped concrete blocks for safety. The space in front of the mortar was protected by sand bags and concrete blocks as shown in Figure 2.

The electric match was ignited by an electric current. The black powder burned, pressure developed and the bar moved forward. The pressure profile was recorded on an oscilloscope and the muzzle velocity of the bar was estimated from the pressure profile.

Results and Discussion

Pressure profile

An example of the observed pressure profiles in the mortar while the bar was shot is shown in Figure 3. The pressure profile shown by the fine line was recorded by the bottom sensor, and the profile shown by the thick line by the middle sensor. Both profiles in the figure were recorded simultaneously in the shot.

As indicated later, the bar stayed in the mortar while the pressure developed, that is, the combustion of the black powder had finished before the bar left the muzzle of the mortar. The pressure of the bottom sensor is higher than that of the middle sensor. The pressure of the bottom sensor is that in the space of the mortar behind the bar, and the pressure of the middle sensor is that in the gap

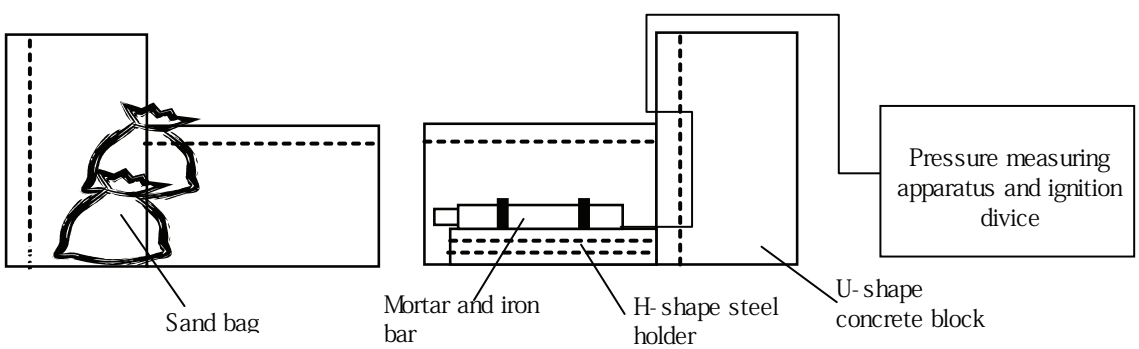

Figure 2 *Setup of the shot experiment of an iron bar.*

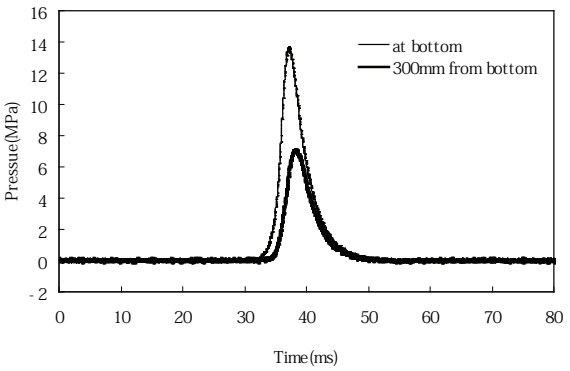

Figure 3 *Pressure profiles in the mortar with 7.5 g black powder.*

between the mortar wall and the bar.

Motion of a bar in the mortar

The motion equations of a bar in the mortar are expressed as follows:

$$m\frac{\mathrm{d}u}{\mathrm{d}t} = A \cdot p(t) \qquad (1)$$

$$\frac{\mathrm{d}z}{\mathrm{d}t} = u \qquad (2)$$

Here, m, u, A and z are the mass, velocity, cross sectional area and traveling distance of the bar, respectively.

$$A = \frac{\pi D^2}{4} \qquad (3)$$

Here, D is the diameter of the bar, and

$$\frac{\mathrm{d}u}{\mathrm{d}t} = \frac{\pi D^2}{4m} \cdot p(t) \qquad (4)$$

Here, $p(t)$ is the observed value and is substituted into equation (4)

Equations (2) and (4) are simultaneously solved by numerical calculation, and acceleration du/dt, velocity u and traveling distance z are obtained.

Equations (2) and (4) were solved by the Runge–Kutta method. The time integration process for ordinary differential equations (2) and (4) was performed using a fourth order accuracy Runge–Kutta method.

The digital pressure data were recorded on an oscilloscope and the data were reduced using Excel. These reduced data were used for calculating acceleration, velocity and the distance traveled by the bar.

The calculated profiles of the acceleration, velocity and distance of the bar are shown in Figure 4.

In all cases, the velocity of the bar increased with time at first, then became constant, suggesting that the combustion of the black powder was complete and that the overpressure in the mortar reached zero. This situation can also be seen in time–distance curves in Figure 4. The distance of the bar from the bottom of the mortar increases with time, but at a point, the rate of increase changes, and then it becomes lower and constant. The change point occurs when the inner overpressure in the mortar reaches zero. With 10 g black powder, the inner overpressure reached zero just before the bar left the muzzle.

The observed and calculated results of the bar shot experiment are listed in Table 1.

Effect of mass of black powder on peak pressure and muzzle velocity

The effect of the mass of black powder on the peak pressures in the mortar is shown in Figure 5. The peak pressures at both the bottom and the middle of the mortar increased exponentially with the mass of black powder.

Plots of the calculated muzzle velocity and kinetic energy of the bar against the mass of black powder are shown in Figure 6. The calculated muzzle velocity increased linearly with the mass of black powder (BP), but the calculated kinetic energy showed an exponential increase with the mass of BP.

Energy efficiency of the shot of the iron bar, shell and star from mortar

It is necessary to know the energy efficiency of the shot of the iron bar from the borehole in Gage's case, in order to estimate the initial velocity and kinetic energy of the bar. The shot energy efficiency of the iron bar, shell and star which were observed

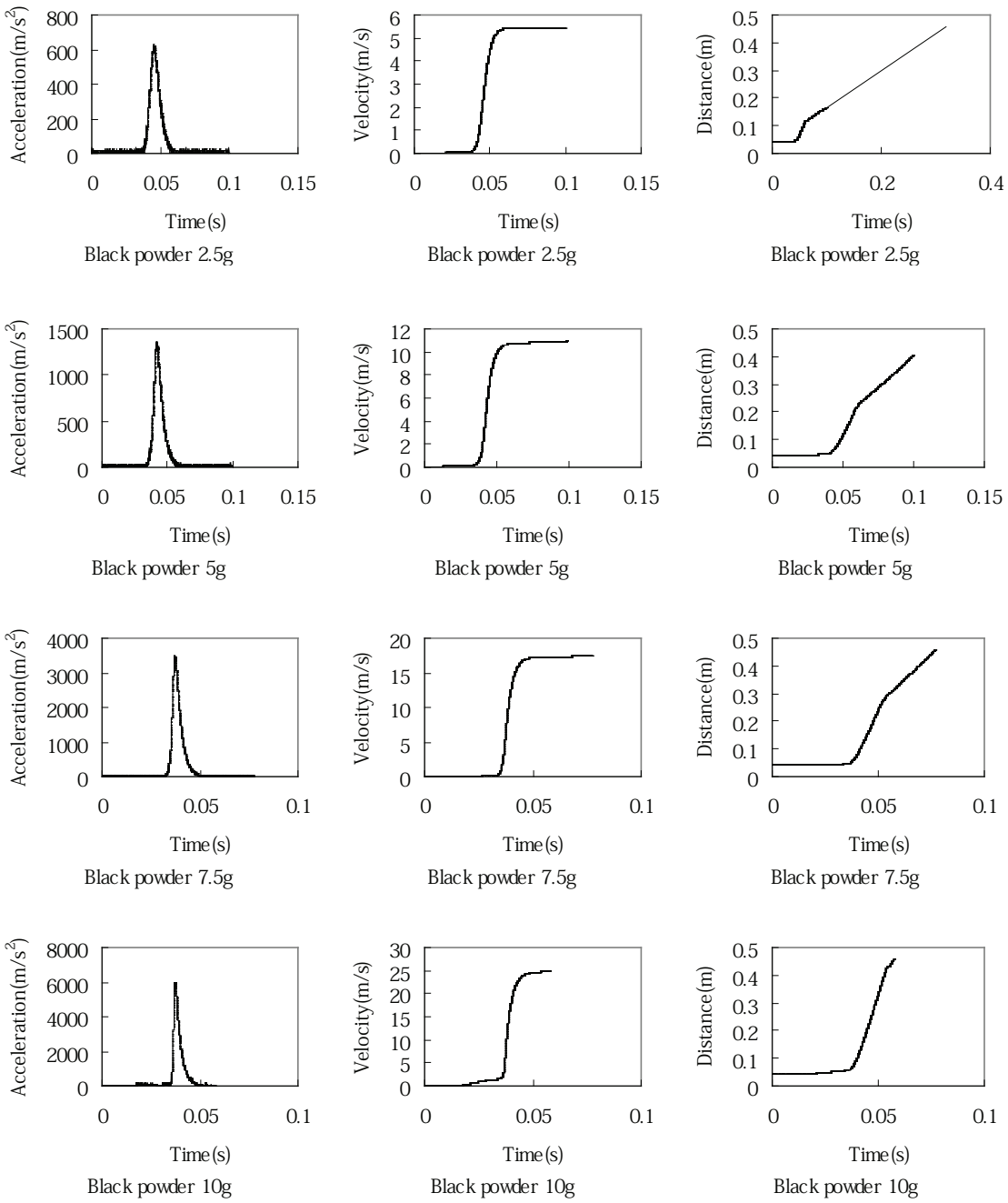

Figure 4 *Calculated profiles of the velocity and distance of the bar in the mortar.*

in experiments are listed in Tables 1 and 2. The shot energy efficiency in Tables 1 and 2 is the kinetic energy of the shot of a projectile divided by the explosion energy of black powder. The explosion energy of black powder was measured and published as 2800 J g^{-1} by Rose.[7]

We could not perform the experiment on the same scale as Gage's case, because no safe facility was available for the experiment. The information from this experiment was limited so it was necessary to estimate the data in Gage's case. So we used for a supplement the star and shell data which we had previously obtained.[4,8]

A plot of the shot energy efficiency of the iron bar against the mass of BP in this work is shown in Figure 7. In this case, with 23% GR, the shot

Table 1 *Observed and calculated results (GR = 23%).*

Run	Mass of BP (g)	P_{max1} (MPa)	T_{max1} (ms)	P_{max2} (MPa)	T_{max2} (ms)	ΔT (ms)	CMV (m s^{-1})	KE (J)	EE (%)
1	15	—	—	—	—	—	—	—	—
2	10	23.3	2.88	11.86	4.06	18.53	24.8	460	1.64
3	7.5	13.55	5.54	6.94	6.86	20.84	17.4	227	1.08
4	5	5.42	7.86	2.77	8.74	24.1	10.9	89	0.64
5	2.5	2.4	9.22	1.16	10.73	25.66	5.4	22	0.31

BP: black powder; P_{max1}: maximum pressure by the bottom pressure transducer; P_{max2}: maximum pressure by the middle pressure transducer; T_{max}: time to maximum pressure: ΔT: time during positive overpressure; CMV: calculated muzzle velocity; KE: kinetic energy of the bar; EE: energy efficiency of the shot

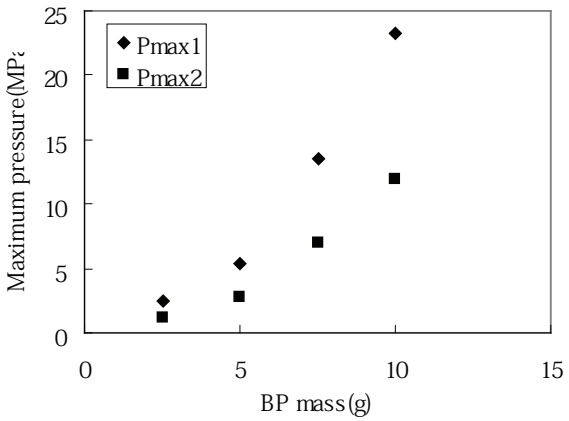

Figure 5 *Plot of peak pressures in the mortar against the mass of black powder.*

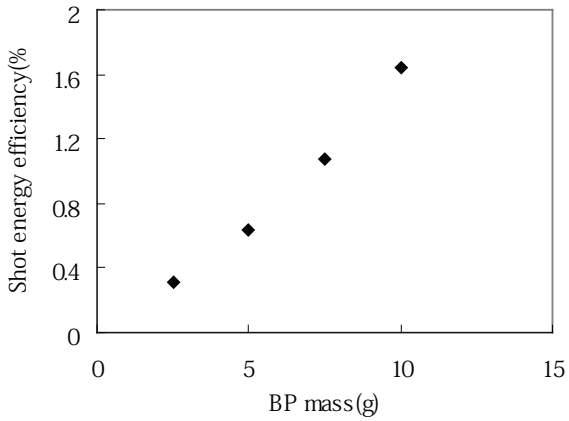

Figure 7 *Plot of the shot energy efficiency of an iron bar vs. BP mass with 23% GR.*

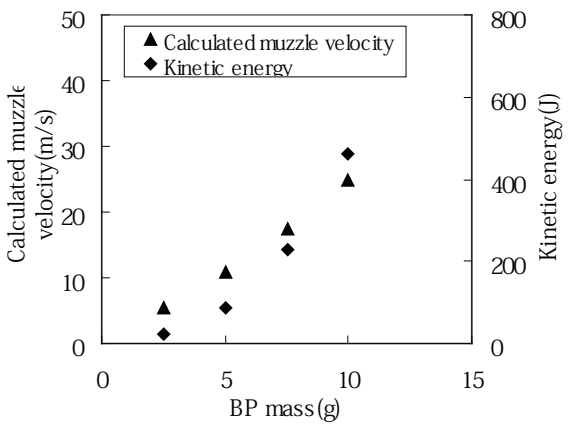

Figure 6 *Plots of the calculated muzzle velocity and kinetic energy of a bar.*

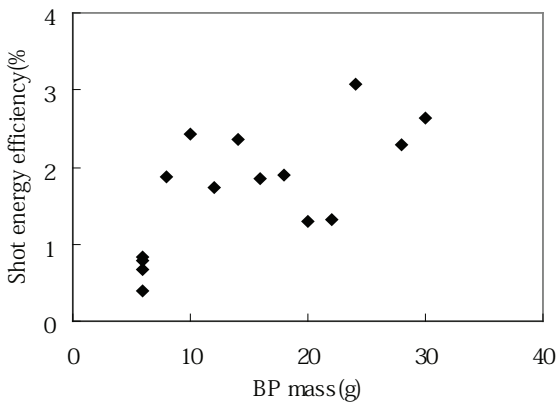

Figure 8 *Plot of the shot energy efficiency of a no. 3 firework shell vs. BP mass with about 13% GR.*

Table 2 *Shot energy efficiency of iron bar, shell and star.*

(1) No. 3 Shell. Dimensions of mortar: ∅ 90 mm × 750 mm (Ref. 4,9)

Run	BP mass (g)	Shell mass (kg)	Shell diameter (m)	GR (%)	Muzzle velocity ($m\ s^{-1}$)	KE (J)	EE (%)
1	30	0.242	0.084	13	135	2208	2.63
2	28	0.242	0.084	12	122	1797	2.29
3	24	0.237	0.084	13	132	2061	3.07
4	22	0.240	0.084	12	82	807	1.31
5	20	0.240	0.084	14	78	730	1.30
6	18	0.242	0.084	13	89	958	1.90
7	16	0.242	0.084	13	83	834	1.86
8	14	0.239	0.084	14	88	926	2.36
9	12	0.237	0.084	14	70	581	1.73
10	10	0.255	0.083	15	73	679	2.43
11	8	0.258	0.083	15	57	419	1.87
12	6	0.250	0.083	15	30	113	0.67
13	6	0.250	0.083	15	23	66	0.39
14	6	0.241	0.084	13	33	131	0.78
15	6	0.241	0.083	15	34	139	0.83

(2) Star. Dimensions of mortar: ∅ 25 mm × 460 mm (Ref. 8)

Run	BP mass (g)	Star mass (kg)	Star diameter (m)	GR (%)	Muzzle velocity (m/s)	KE (J)	EE (%)
1	1	0.0095	0.0224	20	87	36	1.29
2	0.4	0.0095	0.0227	18	27	3	0.31
3	0.7	0.0091	0.0223	20	57	15	0.75
4	2	0.0092	0.0222	21	117	63	1.13
5	1.5	0.0083	0.0218	24	103	44	1.05
6	1.5	0.0089	0.0224	20	106	50	1.19
7	2	0.0086	0.0225	19	117	59	1.05
8	1.5	0.0088	0.0226	18	86	33	0.78
9	1.25	0.0083	0.0224	20	77	25	0.70
10	1.75	0.0085	0.0220	22	91	35	0.72

energy efficiency increased linearly with mass of BP.

A plot of the shot energy efficiency of a no. 3 firework shell against BP mass is shown in Figure 8. The shot efficiency increased with BP mass, though the observed data are very scattered.

Figure 9 shows a plot of the shot energy efficiency of firework stars. With about 20% GR, the shot energy efficiency increased with BP mass in the range of 0–2 g BP. But with about 30% GR, the efficiency decreased somewhat with increasing BP mass when the BP mass exceeded 2 g.

Figure 10 shows a plot of the shot energy efficiency of stars *vs*. GR with 2 g BP mass. The efficiency

Table 2 continued *Shot energy efficiency of iron bar, shell and star.*

(3) Star. Dimensions of mortar: ∅ 20 mm × 360 mm (Ref. 8)

Run	BP mass (g)	Star mass (kg)	Star diameter (m)	GR (%)	Muzzle velocity (m s^{-1})	KE (J)	EE (%)
1	1	0.0038	0.0167	30	79	12	0.42
2	2	0.0038	0.0172	26	116	25	0.45
3	3	0.0037	0.0169	28	131	32	0.38
4	4	0.0041	0.0174	24	167	57	0.51
5	5	0.0033	0.0166	31	145	35	0.25
6	6	0.0038	0.0167	31	190	69	0.41
7	7	0.0037	0.0171	27	195	70	0.36
8	2	0.0039	0.0171	27	119	28	0.49
9	2	0.0040	0.0175	23	138	38	0.68
10	2	0.0035	0.0162	35	134	32	0.57
11	2	0.0041	0.0175	24	121	30	0.53
12	2	0.0038	0.0167	30	126	30	0.54
13	2	0.0019	0.0134	55	93	8	0.15
14	2	0.0018	0.0133	56	83	6	0.11
15	2	0.0018	0.0132	57	104	10	0.18
16	2	0.0020	0.0138	52	104	11	0.19
17	2	0.0018	0.0132	57	90	7	0.13
18	2	0.0009	0.0103	73	65	2	0.03
19	2	0.0008	0.0105	72	40	1	0.01
20	2	0.0009	0.0104	73	39	1	0.01
21	2	0.0011	0.0111	69	90	4	0.08
22	2	0.0010	0.0110	70	79	3	0.06

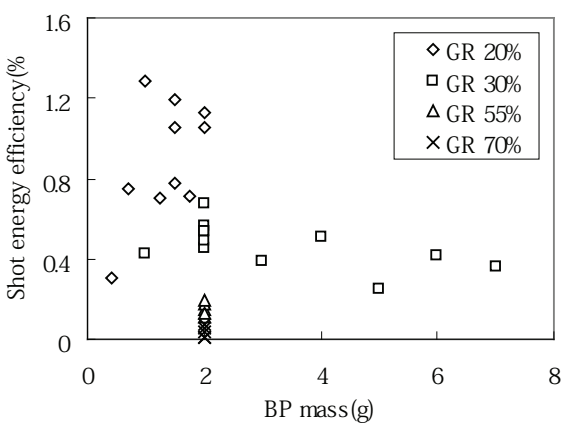

Figure 9 *Plot of the shot energy efficiency of firework stars vs. BP mass with various GR.*

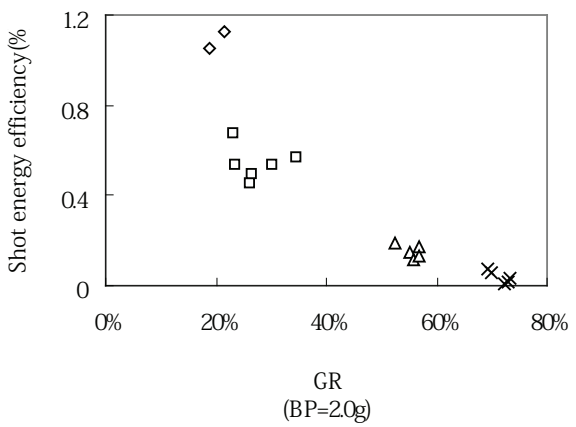

Figure 10 *Plot of the shot energy efficiency of firework stars vs. GR with 2 g BP mass.*

Table 3 *The maximum shot energy efficiency of iron bars, no. 3 firework shell and stars.*

	Shell	Star	Star	Bar (this work)	Bar (Gage's case)
Projectile mass (kg)	0.24	0.0038	0.0038	1.5	6.1
BP mass (kg)	0.024	0.0020	0.0060	0.010	0.40
Projectile/BP	10	1.9	0.63	150	15
GR (%)	13	30	31	23	29
Shot energy efficiency (%)	3.1	0.54*	0.41**	1.6	?

*Maximum shot energy efficiency with 2.0 g BP mass. **Not maximum shot energy efficiency with 6.0 g BP mass.

decreases with increasing gap ratio.

The information about the maximum shot energy efficiencies of iron bars, no. 3 shells and various stars are listed in Table 3. In this Table, the maximum shot energy efficiency was obtained with a small gap ratio (13–20%) and the largest BP mass in the experimental range. However, with a larger gap ratio (about 30%), the efficiency decreased with increasing BP mass (< 2 g).

Estimation of the velocity and kinetic energy of the iron bar in Gage's case

At the moment it is difficult to estimate the shot energy efficiency in Gage's case accurately. Most of data showed that the efficiency increased with BP mass in the experimental range. But with about 30% gap ratio the efficiency decreased with BP mass when the mass exceeded a critical value. From above considerations, the shot energy efficiency of the iron bar in Gage's case may be roughly estimated at about 1%.

The kinetic energy and muzzle velocity of the iron bar in Gage's case are estimated to have been about 11 kJ and 60 m s^{-1}, respectively. A more reliable estimation may be obtained by conducting a similar experiment using the same experimental conditions as in Gage's case.

In our experiment with 15 g black powder, the expelled iron bar penetrated a 20 cm long sand bag and then made a hole in a concrete board about 5 cm thick.

According to the Department of Defense, USA,[10] a hazardous fragment is one having an impact energy of 79 J or greater. The energy of the expelled bar in Gage's case was much greater than the energy of a hazardous fragment.

Acknowledgement

The authors wish to gratefully acknowledge the experimental assistance of the undergraduate students of Higaki Laboratory: Kasiwa, Arima, Ariga, Hukazawa and Morooka. We also thank Mr Takumi Hisaizumi of Kokoro Co. Ltd, for his valuable information.

References

1 J. Martin and J. M. Harlow, *The Boston Medical and Surgical Journal*, vol. 39, no. 20, Wednesday, December 13, 1848, pp. 389–393; J. M. Harlow, *Publications of the Massachusetts Medical Society*, vol. 2, 1868, p. 327.

2 H. Damasio, T. Grabowski, R. Frank, A. M. Galaburda and R. Damasio, "The Return of Phineas Gage: Clues About the Brain from the Skull of a Famous Patient", *Science*, vol. 264, 1994, p. 1102.

3 Y. Ooki, D. Ding, M. Higaki and T. Yoshida, "Burning and Air Resistance of Firework Stars", *Science and Technology of Energetic Materials*, vol. 67, 2006, p. 43.

4 Y. Ooki, D. Ding, M. Higaki and T. Yoshida, "Interior Pressure in the Mortar of a No. 3 Shell in a Firework shot", *Journal of Pyrotechnics*, Issue 22, Winter 2005, pp. 3–8.

5 R. A. Howard, in *Gunpowder: The History of an International Technology*, ed. B. J. Buchanan, Bath University Press, 1996, ch. 1, p. 4.

6 A. P. Van Gelder and H. Schlatter, *History of the Explosives Industry in America*, Columbia University Press, 1927, p. 18.

7 J. E. Rose, IHTR433, "Properties of Black Powder and Charcoal", US Naval Ordnance Station, Indian Head, MD, 1979.

8 D. Ding, M. Higaki, Y. Ooki and T. Yoshida, "Pressure in a Mortar and Estimation of Muzzle Velocity of Expelled Stars", *Journal of Pyrotechnics*, Issue 22, Winter 2005, pp. 50–60

9 D. Ding, M. Higaki, Y. Ooki and T. Yoshida, "Exterior Ballistics of a No. 3 Shell with an Illuminant", *J. Pyrotechnics*, in press.

10 Department of Defense, "DoD Ammunition and Explosives Safety Standards", DoD 6055.9-STD, October 5, 2004, p. 27.

Ballistics of a No. 3 Spherical Shell with Illuminant

Dayu Ding, Y. Ooki, M. Higaki and T. Yoshida*
Ashikaga Institute of Technology
268-1 Omae-cho, Ashikaga-shi, Tochigi 326-8558, Japan
Phone: +81-284-62-0605
Fax: +81-284-62-0976
E-mail: yoshida@ashitech.ac.jp
*To whom all correspondence should be addressed.

Abstract*: Shot experiments were carried out using a No. 3 spherical shell with an illuminant. The three dimensional trajectory of the flying shell was obtained by tracing the shell with two high-speed video cameras in different orientations and by analyzing the recorded video picture. The 3DSTAR1 computer code was developed for calculating the three dimensional trajectory of a flying shell with high accuracy. The optimal drag coefficient, wind speed and wind direction were estimated using the 3DSTAR1 code by fitting the calculated trajectory to the experimental one for a No. 3 shell.*

Keywords: *ballistics, no. 3 shell, trajectory*

Introduction

A firework shell is shot from a mortar, rises into the air, bursts in the sky and releases burning stars. The stars fly into the sky and form a composition like a blooming flower or bunch of flowers. The shell is set in the mortar on top of a lifting charge. The lifting charge is ignited and the shell is shot into the air by the pressure developed by the combustion gas of the lifting charge.

The ballistics of the shell expelled from the muzzle of the mortar are affected by various factors such as muzzle velocity, air drag, shot angle, mass of lifting charge, wind direction and speed, and so on. In terms of the design and safety of the shell shot, it is important to know the basic ballistics of the shell.

Shimizu[1,2] has carried out shot experiments using spherical shells and analyzed the results. Kosanke and Kosanke[3] have performed theoretical modeling of the ballistics of shells using Shimizu's experimental data. Recently, Iida *et al*.[4] have carried out a shot experiment using several sizes of spherical shells. Eckhardt and Andre,[5] and Speer[6] have calculated the trajectories of spherical firework shells in order to investigate an accident at a public fireworks display in 1997. Mercer[7] has modeled the aerodynamics of propelled aerial shells. Schneider and Schneider[8] performed ballistic trajectory calculations to investigate the relationship between the launch elevation of dud aerial firework devices and ground impact distances.

The objectives of this paper are as follows:

(1) A No. 3 spherical shell is shot from a mortar and the trajectory of the shells is observed from different directions by two high-speed video cameras, and the results are three-dimensionally analyzed.

(2) A three-dimensional theoretical model of the ballistics of the shell is developed, a theoretical calculation is carried out, and the effect of wind direction and speed, air drag, shot angle and so on are examined.

Experimental

Materials

No. 3 spherical shells with an illuminant for tracing the trajectory were made by the Sunaga Fireworks Company. The lifting charge and electric match were made by the Nippon Kayaku Company. The mass and diameter of the shells and the mass of lifting charges in this experiment are listed in Table 1 along with the observed muzzle velocity.

Apparatus

The mortar for the No. 3 shells was made of steel and the dimensions of the mortar are shown in Figure 1.

The trajectory of an expelled shell was traced

Table 1 *Mass and diameter of the shell, mass of lifting charge, and muzzle velocity.*

Run	Mass (kg)	Diameter (m)	Lifting charge (g)	Muzzle velocity ($m\ s^{-1}$)
1	0.255	0.083	10	73
2	0.258	0.083	8	57
3	0.250	0.083	6	30
4	0.250	0.083	6	23
5	0.241	0.084	6	33
6	0.241	0.083	6	34

by two high-speed video cameras (Phantom VR-V4.2) with a frame rate of 150 frames per second. The locations of the two cameras are shown in Figure 2.

Procedure

The mortar was set on the ground vertically. The lifting charge and electric match wrapped in thin paper were put in the bottom of the mortar. Then a No. 3 shell was placed on the lifting charge. The electric match was ignited by turning on an electric current. The lifting charge burned, pressure developed, the shell moved upwards and was expelled into the air. The trajectory of the shell in the air was recorded by the high-speed cameras.

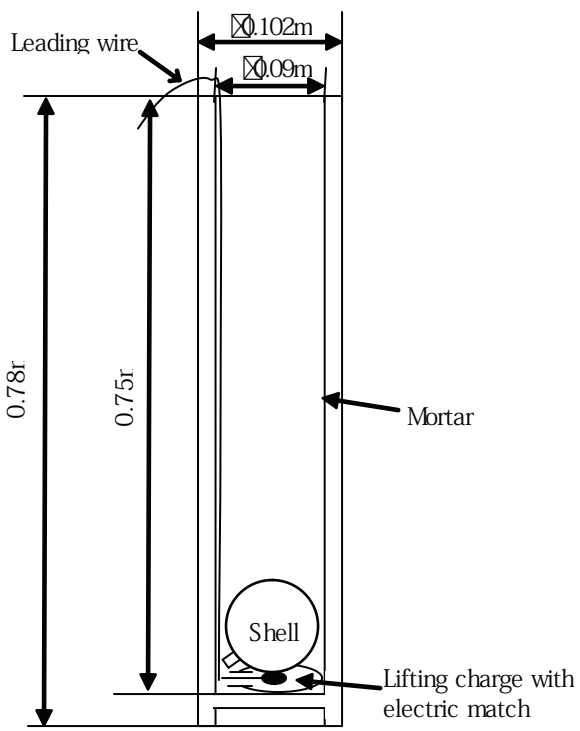

Figure 1 *Dimensions of the mortar for No. 3 shells.*

Three dimensional analysis of experimental data

The position of the shell flying in the air is analyzed using two cameras located as in Figure 2. Two three-dimensional rectangular coordinates are provided for the locations of the cameras. The muzzle of the mortar is the origin of the coordinates. The perpendicular direction is the *z* axis of the coordinates. The two horizontal coordinates are *X*–*Y* and *x*–*y*, and camera 1 is on the *X* axis of the *X*–*Y* coordinates and camera 2 is on the *y* axis of the *x*–*y* coordinates as shown in Figure 2. The *Y* coordinate of the shell in the *X*–*Y* coordinates is recorded by camera 1 and the *x* coordinate in the *x*–*y* coordinates is recorded by camera 2. The relationships of the two coordinates

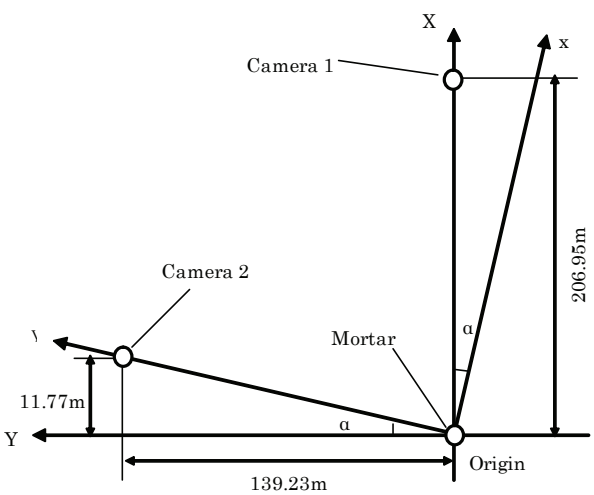

Figure 2 *Location of high-speed cameras.*

are as follows.

$$x = X\cos\alpha - Y\sin\alpha \qquad (1)$$

$$y = X\sin\alpha + Y\cos\alpha \qquad (2)$$

The coordinate y is calculated from the angle α, and the recorded x and Y values, using equations (1) and (2).

Finally, the spatial position (x, y, z) of the firework shell in one set of three-dimensional rectangular coordinates is obtained. These coordinates were converted to the real distances, and the real spatial position of the shell at a given time is calculated.

Three-dimensional model for ballistics of a shell

Equations of motion

As a shell flies into the air, a complex aerodynamic drag force acts on it. The force will depend on the density of the air, the viscosity of the air, the shape and surface roughness of the shell, etc. To simplify the problem, the following assumptions are made.

(1) The shell does not spin in flight.

(2) The shell is spherical.

(3) The air density and air viscosity are constant.

(4) The speed and the direction of the wind are constant.

The vectors of position, velocity and acceleration of the shell, and the force acting on the shell, are expressed by rectangular coordinates. For example, the vector of the position of a shell is expressed by rectangular coordinates as shown in Figure 3.

$$\vec{r} = x\vec{i} + y\vec{j} + z\vec{k}$$

$$x = r\sin\beta_1\cos\alpha_1 \qquad y = r\sin\beta_1\sin\alpha_1$$

$$z = r\cos\beta_1$$

$$r^2 = x^2 + y^2 + z^2 \qquad (3)$$

The motion equation of a spherical shell is

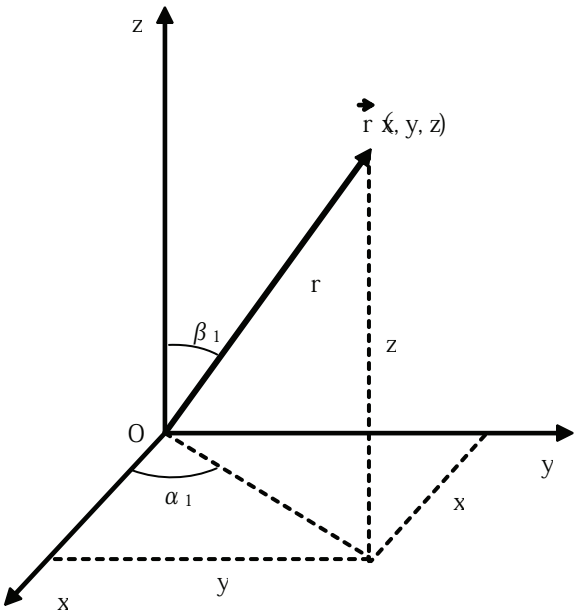

Figure 3 *Three dimensional coordinates of positional vector* $\vec{r}$.

$$\tan\alpha_1 = \frac{y}{x}$$

$$\tan\beta_1 = \frac{\sqrt{x^2 + y^2}}{z}$$

Here, $\vec{i}$, $\vec{j}$ and $\vec{k}$ are the unit vectors of the coordinates x, y and z, respectively.

α_1 is the angle between the shadow of the vector $\vec{r}$ in the x–y plane and the coordinate x, and β1 is the angle between the vector $\vec{r}$ and the coordinate z expressed as follows:

$$m\frac{\mathrm{d}\vec{v}}{\mathrm{d}t} = m\vec{g} + \vec{F}_D + \vec{F}_B \qquad (4)$$

Here, $\vec{g}$, $\vec{v}$, $\vec{F}_D$ and $\vec{F}_B$ are the vectors of acceleration under gravity, velocity of the shell, air drag and buoyancy, respectively. m is the mass of the shell.

Furthermore,

$$\vec{v} = \frac{\mathrm{d}\vec{r}}{\mathrm{d}t} \qquad (5)$$

$$\vec{F}_D = -\frac{\rho A C_D}{2} \cdot |\vec{u}| \cdot \vec{u} = -k|\vec{u}| \cdot \vec{u} \quad (6)$$

$$\vec{F}_B = -\frac{\rho}{\rho_p} m\vec{g} \quad (7)$$

Here, ρ, ρ_p, A and C_D are air density, density of the shell, cross-sectional area of the shell and drag coefficient of air, respectively. $\vec{r}$ and $\vec{u}$ are positional vector of the shell and relative velocity vector between air and the shell.

The motion velocity of a shell:

$$\vec{v} = v_x\vec{i} + v_y\vec{j} + v_z\vec{k} \quad (8)$$

Here,

$$v_x = |v| \sin\beta_2 \cos\alpha_2$$
$$v_y = |v| \sin\beta_2 \sin\alpha_2$$
$$v_z = |v| \cos\beta_2$$
$$v^2 = {v_x}^2 + {v_y}^2 + {v_z}^2$$
$$\tan\alpha_2 = \frac{v_y}{v_x}$$
$$\tan\beta_2 = \frac{\sqrt{{v_x}^2 + {v_y}^2}}{v_z}$$

The wind velocity vector $\vec{w}$ is constant,

$$\vec{w} = w_x\vec{i} + w_y\vec{j} + w_z\vec{k} \quad (9)$$

Here,

$$w_x = |w| \sin\beta_3 \cos\alpha_3$$
$$w_y = |w| \sin\beta_3 \cos\alpha_3$$
$$w_z = |w| \sin\beta_3 \cos\alpha_3$$

Relative velocity between the shell and air is:

$$\vec{u} = \vec{v} - \vec{w} = (v_x - w_x)\vec{i} + (v_y - w_y)\vec{j} + (v_z - w_z)\vec{k} \quad (10)$$

$$|\vec{u}| = |\vec{v} - \vec{w}| = \sqrt{(v_x - w_x)^2 + (v_y - w_y)^2 + (v_z - w_z)^2} \quad (11)$$

Therefore, the motion equations of a flying shell in the air are:

$$\frac{\mathrm{d}\vec{v}}{\mathrm{d}t} = (1 - \frac{\rho}{\rho_p})\vec{g} - k|\vec{v} - \vec{w}|(\vec{v} - \vec{w}) \quad (12)$$

In the three dimensional rectangular coordinate shown in Figure 3, the gravity acceleration can be expressed as follows:

$$\vec{g} = -g\vec{k}$$

And the equations of motion are:

$$\frac{\mathrm{d}v_x}{\mathrm{d}t} = -k|\vec{v} - \vec{w}| \cdot (v_x - w_x) \quad (13)$$

$$\frac{\mathrm{d}x}{\mathrm{d}t} = v_x \quad (14)$$

$$\frac{\mathrm{d}v_y}{\mathrm{d}t} = -k|\vec{v} - \vec{w}| \cdot (v_y - w_y) \quad (15)$$

$$\frac{\mathrm{d}y}{\mathrm{d}t} = v_y \quad (16)$$

$$\frac{\mathrm{d}v_z}{\mathrm{d}t} = -(1 - \frac{\rho}{\rho_p})g - k|\vec{v} - \vec{w}| \cdot (v_z - w_z) \quad (17)$$

$$\frac{\mathrm{d}z}{\mathrm{d}t} = v_z \quad (18)$$

Here, $k = \frac{\rho A C_D}{2m}$; when the shell is a sphere, $k = \frac{3\rho C_D}{4\rho_p D_p}$, where D_p is the diameter of the sphere.

Numerical calculation of motion equations

It is difficult to integrate equations (13)–(18) directly. Therefore, numerical calculation of equations (13)–(18) was carried out using the fourth-order Runge–Kutta method in this work.

Results and Discussion

Calculation accuracy of the 3DSTAR1 code

The numerical calculation results by 3DSTAR1 were compared with the analytical solutions, and the accuracy of the former was validated.

At first, considering the motion of the shell expelled perpendicularly into the sky without air drag, the perpendicular velocity V_z and position z were calculated using 3DSTAR1. The muzzle velocity of the expelled shell was assumed to be 119 m s^{-1} and the calculated results are shown in Figure 10.

On the other hand, V_z and z can be obtained analytically as follows:

$$V_z = V_0 - g \cdot t \qquad (19)$$

$$z = z_0 + V_0 \cdot t - \frac{1}{2} g \cdot t^2 \qquad (20)$$

As shown in Figure 4, the results from the 3DSTAR1 numerical calculation agreed completely with the analytical solution of equations (19) and (20).

Effect of time interval on calculation accuracy of 3DSTAR1 code

Kosanke and Kosanke[3] published "Computer Modeling of Aerial Shell Ballistics", and validated the results using Shimizu's experimental data. The effect of the time interval on the accuracy of the 3DSTAR1 code was examined using the same data:

Muzzle velocity of the shell: 118.95 m s^{-1}

Diameter of the shell: 0.17125 m

Mass of the shell: 2.1111 kg

Angle of the mortar: 0°

Wind speed: 0 m s^{-1}

Drag coefficient: 0.36

When the drag coefficient is constant, the analytical solutions of the equations of motion of the shell expelled perpendicularly are as follows

Time to apogee $$t_1 = \frac{1}{\sqrt{gk}} \cdot \tan^{-1}\left(\sqrt{\frac{k}{g}} \cdot V_0\right) \qquad (21)$$

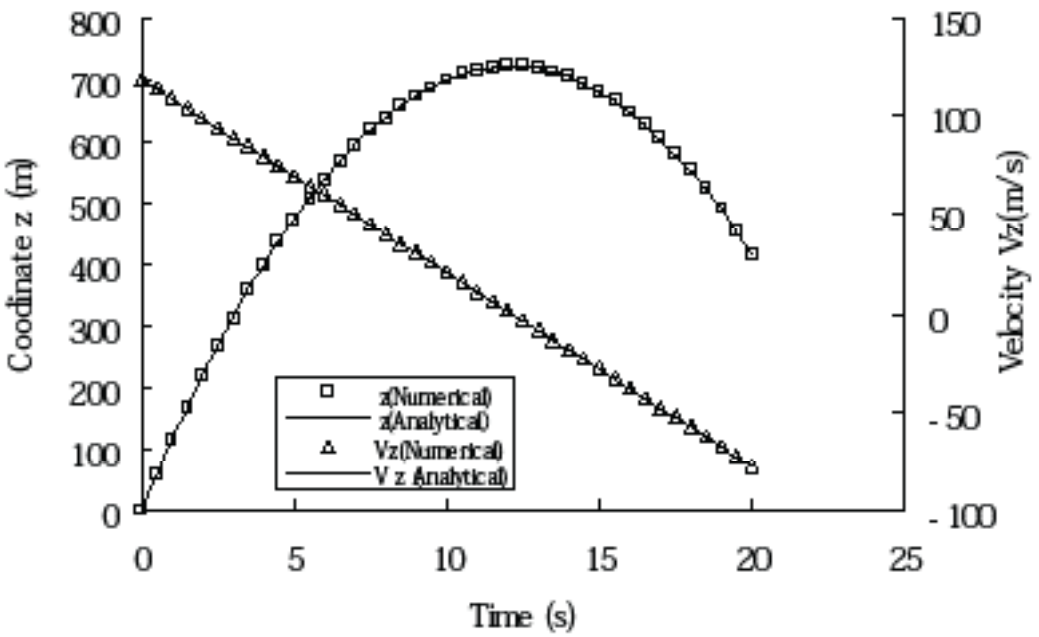

Figure 4 *Comparison of 3DSTAR1 calculation and analytical solution. Without air drag and with 119 m s^{-1} muzzle velocity.*

Apogee height $$Z_1 = \frac{1}{2k} \cdot \ln\left(1 + \frac{k}{g} V_0^2\right) \quad (22)$$

Velocity to impact $$V_2 = -\sqrt{\frac{g}{k}} \cdot \left(1 - e^{-2kZ_1}\right) \quad (23)$$

Time to impact $$t_2 = t_1 - \frac{1}{\sqrt{gk}} \cdot \tanh^{-1}\left(\sqrt{\frac{k}{g}} \cdot V_2\right) \quad (24)$$

Here, $k = \frac{3\rho C_D}{4\rho_p D_p}$ and g, ρ, C_D, ρ, D_p and V_0 are acceleration under gravity, air density, air drag coefficient, and density, diameter and muzzle velocity of the shell, respectively. The velocity of the shell is positive when the shell moves upward, and negative when it moves downward.

The results are shown in Table 2 and Figure 5.

It can be seen from Figure 5 that even if the time interval is 1 s, the computer code can give high enough calculation accuracy.

Results of observed and calculated three dimensional trajectory

The video pictures of the motion of the shell in the air were recorded by two cameras facing in

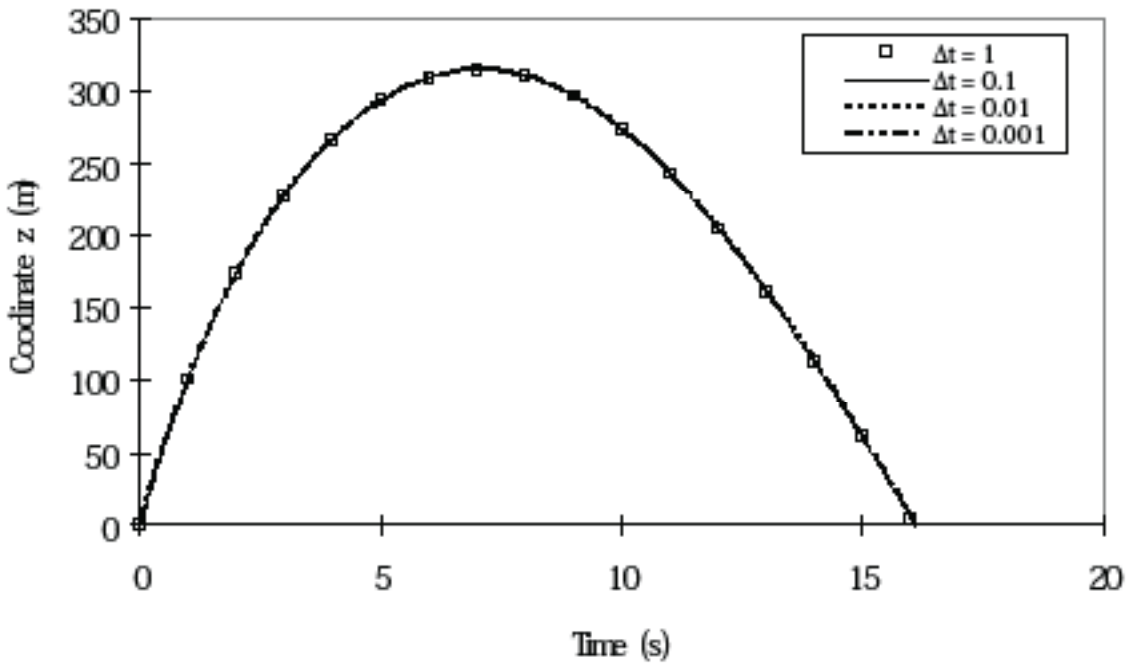

Figure 5 *Calculated results by 3DSTAR1.*

Table 2 *Calculated results by 3DSTAR1 along with analytical solution.*

Time interval (s)	Time to apogee (s)	Apogee height (m)	Time to impact (s)
1.0	7	314.246	16
0.1	7.0	314.3288	16.0
0.01	7.06	314.3479	16.08
0.001	7.063	314.3479	16.087
Analytical solution by equations (30)–(33)	7.0637	314.3485	16.0857

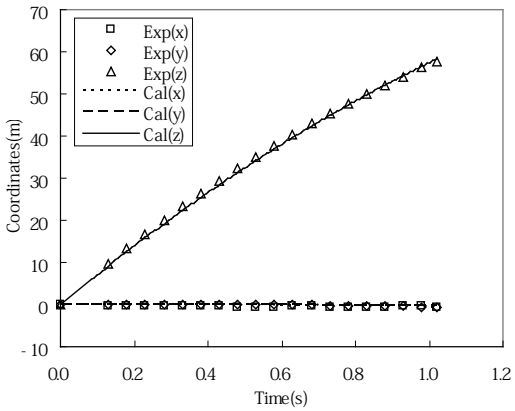

Figure 6 *Observed and calculated trajectories of an airborne No. 3 shell (run 1).*

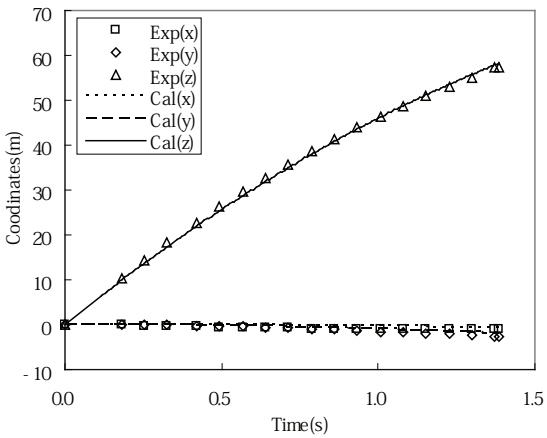

Figure 7 *Observed and calculated trajectories of an airborne No. 3 shell (run 2).*

different directions. These pictures were analyzed and the trajectory of the shell was expressed using three dimensional rectangular coordinates. The results are shown in Figures 6–11.

It is seen from Figures 6–11 that the shells were expelled nearly perpendicularly but moved with a tilt angle at high altitude. This may be the effect of the wind.

The muzzle velocity of the shell was determined from the trajectory of the shell in the air. The results are listed in Table 1. The muzzle velocity tends to increase with increasing mass of lifting charge, but the scatter is large.

Trial and error calculations were carried out using

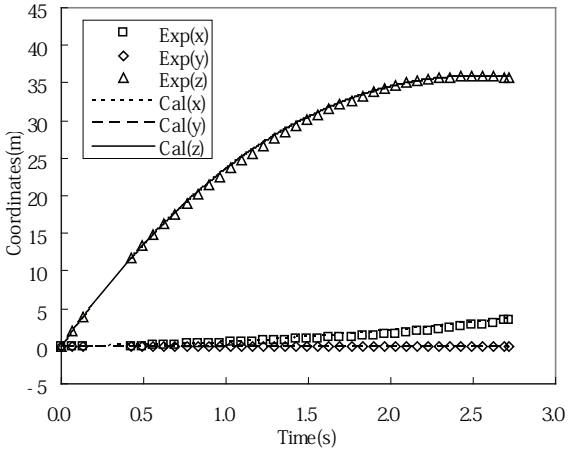

Figure 8 *Observed and calculated trajectories of an airborne No. 3 shell (run 3).*

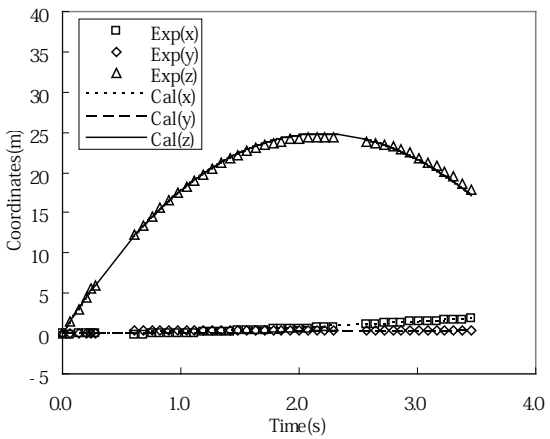

Figure 9 *Observed and calculated trajectories of an airborne No. 3 shell (run 4).*

the 3DSTAR1 code for fitting the drag coefficient, wind speed and wind direction to the observed trajectory of the shell, and the optimal values were obtained. These values are listed in Table 3. The calculated trajectories with these values are also shown in Figures 6–11.

Conclusions

A shot experiment using a No. 3 spherical shell with an illuminant was carried out and three dimensional calculations were performed. The following conclusions were derived:

(1) The three dimensional trajectory of the flying

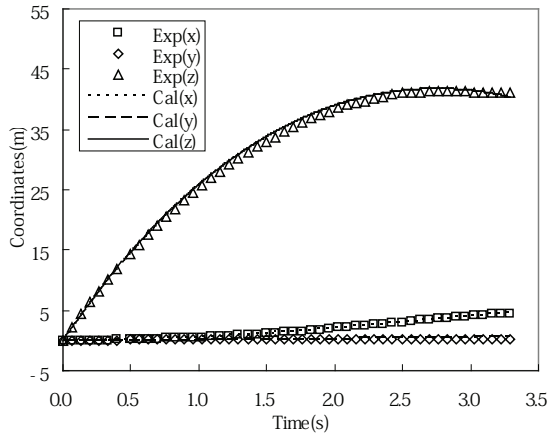

Figure 10 *Observed and calculated trajectories of an airborne No. 3 shell (run 5).*

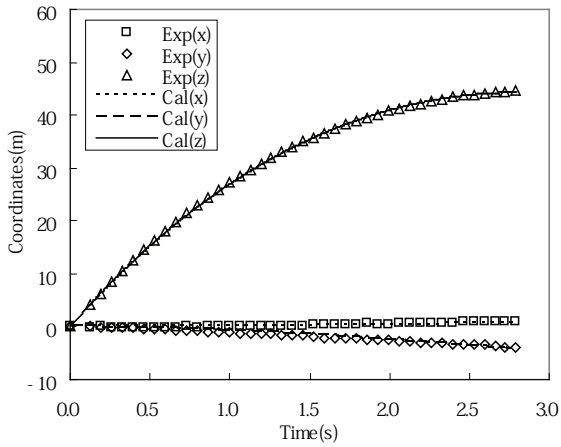

Figure 11 *Observed and calculated trajectories of an airborne No. 3 shell (run 6).*

shell was obtained by tracing the shell with two high-speed video cameras aimed in different directions, and by analyzing the recorded video picture three dimensionally.

(2) The 3DSTAR1 code was developed for calculating the three dimensional trajectory of a flying shell with a high calculation accuracy.

(3) The optimal drag coefficient, wind speed and wind direction were estimated using 3DSTAR1 code by fitting the calculated trajectory to the experimental one for a No. 3 shell.

Acknowledgement

The authors wish to gratefully acknowledge the experimental assistance of the Showarika Company, and to M. Aoyagi, an undergraduate student in the Higaki Laboratory.

Table 3 *Muzzle velocity and drag coefficient of the shell, wind speed and wind direction.*

Run	Muzzle velocity ($m\ s^{-1}$)	Drag coefficient	Wind speed ($m\ s^{-1}$)	Angle between directions of wind and coordinate x (°)
1	73	0.53	5	225
2	57	0.53	10	−110
3	30	0.99	7	0
4	23	0.71	4	10
5	33	0.67	7	8
6	34	0.63	8	−80

References

1 T. Shimizu, "On Ballistics of Fireworks Shells", *Journal of the Industrial Explosives Society, Japan*, vol. 18, no. 3, 1957, pp. 212–225.

2 T. Shimizu, "On Ballistics of Fireworks Shells (2) Character of the Air Resistance and Effect of Grain Size of the Lifting Charge", *Journal of the Industrial Explosives Society, Japan*, vol. 20, no. 5, 1959, pp. 336–349.

3 K. L. Kosanke and B. J. Kosanke, "Computer Modeling of Aerial Shell Ballistics", *Pyrotechnica*, XIV, 1992, pp. 46–57.

4 M. Iida, S. Hatanaka and N. Suruga, "Shot Experiment of Firework Shell (1)", *Abstracts of Spring Meeting of Japan Explosives Society*, May 26–27, 2005, Otsu, pp. 65–67.

5 D. Eckhardt and H. Andre, "Results and Conclusions from the Investigation of an Accident with a Display Shell", Proceedings of the 5th International Symposium on Fireworks, Naples, Italy, 2000, pp. 85–103.

6 M. Speer, "Reasons for Fuse Failure and Drift Distance of Spherical Fireworks Shells", *Journal of Pyrotechnics*, Issue 17, Summer 2003, pp. 35–52.

7 J. E. Mercer, "Thermodynamics of Black Powder and Aerodynamics of Propelled Aerial Shells", *Journal of Pyrotechnics*, Issue 16, Winter 2002, pp. 37–52.

8 R. L. Schneider and S. C. Schneider, "External Ballistic Calculations for Display Fireworks Launched from Elevated Locations", *Proceedings of the 8th International Symposium on Fireworks*, Shiga, Japan, 2005, pp. 408–415.

Effect Of Particle Size On The Mechanical Sensitivity And Thermal Stability Aspects Of Pyrotechnic Flash Compositions

S. P. Sivapirakasam,[a] M. Surianarayanan,[b]* F. Chandrasekaran[b] and G. Swaminathan[b]

[a]TIFAC-CORE in Industrial Safety, Department of Mechanical Engineering,
Mepco Schlenk Engineering College, Sivakasi - 626 005, India
[b]Cell for Industrial Safety & Risk Analysis, Chemical Engineering Department,
Central Leather Research Institute,
(Council of Scientific & Industrial Research), Adyar, Chennai - 600 020, India
*Corresponding author: e-mail: msuri1@vsnl.com

Abstract: *The mechanical and thermal sensitivity of pyrotechnic flash compositions consisting of mixtures of potassium nitrate (KNO_3), sulphur (S) and aluminum (Al) with varying particle sizes of KNO_3 and Al indicated that, irrespective of the composition of the cracker mixture, all the compositions were found to be thermally and mechanically sensitive. Although the impact sensitivity results reflected the change in the surface area of the particle sizes, the changes were within a narrow range of limiting impact energy (LIE) (7.5–9.1 J). Further it was difficult to pinpoint a particular sieve fraction as sensitive since the response to explosion depended normally on the flash composition and the particle size but also on the density and the compactness of the chemicals*

DSC studies on the effect of the Al particle size showed that a decrease in the Al particle size led to a second exothermic activity. This behavior should be viewed with caution when considering safety aspects.

Keywords: *pyrotechnics, flash composition, fireworks, impact sensitiveness, friction sensitiveness, differential scanning calorimeter, potassium nitrate, sulphur, aluminum*

Introduction

In recent years frequent incidents have been reported involving fireworks during their processing, storage and transportation.[1] Large quantities of different categories or types of fireworks are manufactured and demand for them is rising continuously. In general, the composition of fireworks is basically a mixture of sulphur, phosphorus, chlorates, nitrates and pure aluminum metal powder. These mixtures are highly sensitive to temperature, mechanical impact, pressure and friction. Knowledge of the thermal stability, auto-ignition temperature, impact sensitivity, frictional sensitivity and electrostatic sensitivity of these mixtures is required to assess their hazard potential as well as to make suitable plans for safety during processing, storage, and transportation.[2,3]

Reported information on the sensitivity to thermal, mechanical and electrostatic hazards is scarce. Recently efforts have been made by Sivapirakasam *et al*. to study the thermal hazards and the impact sensitivity of various compositions of cracker mixtures.[4,5] The parameters that influence the mechanical and thermal sensitivity are particle size, purity, and moisture content of the chemicals and ambient conditions. Though there are a few reported studies on the effect of particle size on the mechanical sensitivity and thermal stability of some pyrotechnic mixtures,[6,7] pyrotechnic flash composition mixture consisting of KNO_3, S and Al has not yet been studied. This work attempts to report the effects of the particle sizes of KNO_3 (oxidizer) and Al (fuel) in pyrotechnic flash compositions on the mechanical sensitivity and thermal stability.

Particle sizes of the ingredients and their effects in pyrotechnics

Pyrotechnic compositions are sensitive to thermal and mechanical stimuli. The degree of the hazard depends upon the rate of availability of these energies in addition to the particle size of the components of the mixture, confinement and momentum (the force during impact). Each one of the factors has a significant role in enhancing the overall hazard potential of the mixture.

It has been reported[8] that the ease of ignition is greatly dependent on the particle size and surface area of the ingredients. Smaller particle sizes create large interfacial areas, and increased numbers of atoms at the particle interface which on ignition lead to a higher heat of reaction. These effects however are not actually consistent due to the results of various physical and chemical processes occurring concomitantly and in many instances competitively. This is particularly true where an endothermic phase change absorbs some of the heat of combustion.[9]

When the particles in a pyrotechnic mixture are small and jagged, less energy input (*via* impact, friction and thermal stimuli) is needed to produce hot spots. This is because energy is localized at the stress points. Also, dislocations, cracks and other discontinuities in the crystal structure are conducive to the formation of hot spots.[10] Ignition is achieved when the energy released from the initiating hot spots is sufficient in quantity and is efficiently captured by the adjacent layers or grains of blended chemical compositions.[11]

Experimental

Materials

The flash compositions were prepared from materials purchased from SD's fine chemicals, Mumbai. KNO_3 and S were of high purity (AnalaR) grade and Al was of LR grade.

Preparation of sieve fractions of KNO_3 and Al

The sieve fractions of KNO_3 and Al were prepared using the standard sieves obtained from Jayant Scientific Industries, Mumbai, India. Particles of KNO_3 passed through a 63 μm sieve mesh and collected in a 53 μm sieve mesh were termed as +53 μm sieved fractions. Similarly, five other sieve fractions of +63 μm, +75 μm, +90 μm, +105 μm, and +150 μm were prepared. The details of the sieved fractions separated for the study are summarized in Table 1. Similarly Al was separated into 5 sieved fractions and the details are given in Table 2.

In order to examine the effect of varying the particle size of KNO_3 on the sensitiveness of a flash composition, the sieved fraction of KNO_3 was mixed with the other two components *i.e.*, S, Al. The particles of S and Al were passed through a 100 mesh brass sieve. Similarly, in order to examine the effect of varying particle sizes of Al on the sensitiveness of a flash composition, the sieved fraction of Al was mixed with the other two components *i.e.* KNO_3 and S. The particles of KNO_3 and S were passed through a 100 mesh brass sieve. Tables 3, 4, 5 and 6 show the various flash compositions and the corresponding mixture fractions taken for studies.

Table 1 *Particle sizes of KNO_3.*

Sample No.	Particle Size of KNO_3
1	+ 53 μm (53 to 63 μm)
2	+63 μm (63 to 75 μm)
3	+75 μm (75 to 90 μm)
4	+90 μm (90 to 105 μm)
5	+105 μm (105 to 150 μm)
6	+150 μm (150 to 200 μm)

Table 2 *Particle sizes of Al.*

Sample No.	Particle Size of Al
1	+37 μm (37 to 45 μm)
2	+45 μm (45 to 53 μm)
3	+53 μm (53 to 63 μm)
4	+63 μm (63 to 90 μm)
5	+90 μm (90 to 105 μm)

Measurement of impact sensitivity

Impact sensitivity measurements on flash compositions with varying KNO_3 and Al particle sizes were carried out according to the procedure outlined in the United Nations (UN) Recommendations on the transport of dangerous goods.[12] The design and principle of the equipment were similar to those of a drop fall hammer of BAM standards. The details of the equipment employed in this study are presented elsewhere.[4]

Measurement of friction sensitivity

Friction sensitivity measurements on flash compositions with varying KNO_3 and Al particle sizes were carried out by BAM (friction tester) according to the procedure outlined in the United Nations (UN) Recommendations on the transport of dangerous goods.[13]

Thermal studies

A Differential Scanning Calorimetry (DSC) module 2910 model from TA Instruments was used for thermal stability measurements for the flash compositions with different KNO_3 and Al particle sizes. The studies were conducted with a sample size of 2 mg under pure nitrogen gas at a flow rate of 100 µl min^{-1}. The equipment and the experimental conditions employed have been reported in detail elsewhere.[5]

Results and Discussion

Effect of KNO_3 particle size on impact sensitivity

Impact sensitivity testing results for 3 different flash composition mixture ratios consisting of KNO_3, S and Al with varying KNO_3 particle sizes in the range of 53–150 µm are shown in Figure 1. The plot shows that all the mixture compositions studied were impact sensitive and Limiting Impact Energy (LIE) was in the range of 7.5 to 9.1 J. Hence, these mixtures could be grouped as category III explosives according to the classification of Andreiev-Beliave.[14,15] From Figure 1 it can be seen that an increase in the particle size of KNO_3 decreased the sensitivity to impact initially up to 63 µm and then increased it. This trend was due to the fact that impact sensitivity depends not only on the flash composition and the particle size but also on the particle shape, density and compactness of the chemicals.

Effect of Al particle size on impact sensitivity

Figure 2 shows the impact on the flash composition mixtures with varying Al particle sizes. The flash composition mixtures with the lowest particle sizes showed high sensitivity compared with those with higher particle sizes. This trend could be attributed to the increase in surface area as the Al particle size decreased. All the mixtures studied were impact sensitive and varied within a narrow range of LIE (8.5–11.5 J) and hence the flash composition mixtures could be grouped as category III explosives as per the classification of Andreiev-Beliave.[14,15]

Effect of KNO_3 particle size on friction sensitivity

Figure 3 shows the effect of KNO_3 particle size on the friction sensitivity of various flash composition mixtures consisting of KNO_3, S and Al. The friction sensitivity decreased with increasing KNO_3 particle sizes. The varying particle size of KNO_3 set the lowest friction load of 144 N for the flash composition studied. KNO_3 being an oxidizer, the effect of particle size was appreciable.

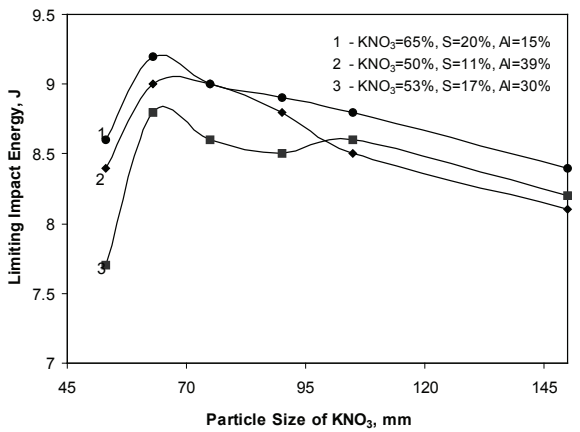

Figure 1 *Effect of KNO_3 particle size of flash compositions on the impact sensitivity.*

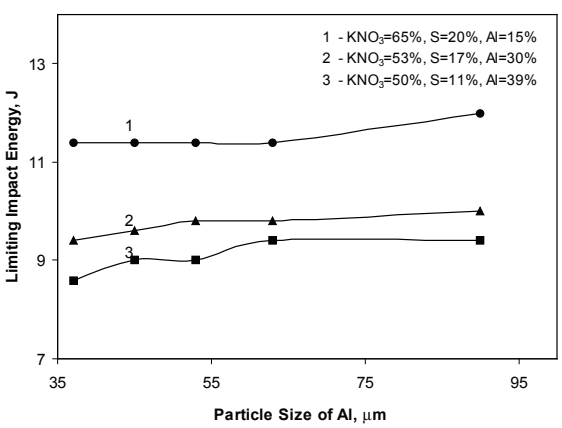

Figure 2 *Effect of Al particle size of flash compositions on the impact sensitivity.*

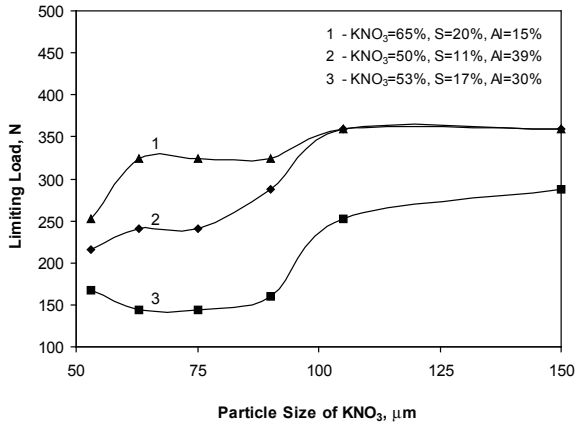

Figure 3 *Effect of KNO_3 particle size of flash compositions on the friction sensitivity.*

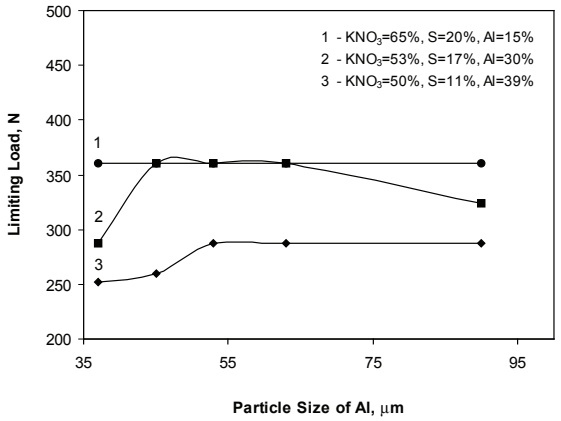

Figure 4 *Effect of Al particle size of flash compositions on the friction sensitivity.*

Effect of particle size of Al on friction sensitivity

The effect of Al particle size on the friction sensitivity of flash composition is presented in Figure 4. Although these mixtures were shown to be sensitive to friction there was no appreciable change with the change in Al particle size.

Effect of KNO_3 particle size on thermal stability

Table 5 shows the influence of KNO_3 particle size on the thermal decomposition of a pyrotechnic mixture. This is followed using DSC plots stacked according to the varying particle sizes (Figures 5, 6 and 7). In general, for all the flash compositions, the exothermic peak recorded between 299 °C

Table 3 *Effect of KNO_3 particle size for the various flash composition mixtures on mechanical sensitivity.*

Composition (wt%)	Particle Size (μm)	Limiting Impact Energy (J)	Frictional Limiting Load (N)
KNO_3 = 50% S = 11% Al = 39%	53	8.4	216
	63	9.0	240
	75	9.0	240
	90	8.8	288
	105	8.4	360
	150	8.0	360
KNO_3 = 53% S = 17% Al = 30%	53	7.7	168
	63	8.8	144
	75	8.6	144
	90	8.5	160
	105	8.6	252
	150	8.2	288
KNO_3 = 65% S = 20% Al = 15%	53	8.6	252
	63	9.3	324
	75	9.0	324
	90	8.9	324
	105	8.8	360
	150	8.6	360

Table 4 *Effect of Al particle size for the various flash composition mixtures on mechanical sensitivity.*

Composition (wt%)	Particle Size (μm)	Limiting Impact Energy (J)	Frictional Limiting Load (N)
	37	8.6	252
KNO_3 = 50%	45	9.0	260
S = 11%	53	9.0	288
Al = 39%	63	9.4	288
	90	9.4	288
	37	9.4	288
KNO_3 = 53%	45	9.6	360
S = 17%	53	9.8	360
Al = 30%	63	9.8	360
	90	10	324
	37	11.3	360
KNO_3 = 65%	45	11.3	360
S = 20%	53	11.3	360
Al = 15%	63	11.3	360
	90	11.9	360

Table 5 *Effect of KNO_3 particle size for the various flash composition mixtures on thermal sensitivity.*

Composition (wt%)	Particle Size of KNO_3 (μm)	Onset Temperature (ºC)	Peak Maximum Temperature (ºC)	Heat of Reaction (J g^{-1})	End Temperature (ºC)
	53	300.16	316.57	30.25	320.21
	63	319.66	316.57	48.93	329.90
KNO_3 = 50%	75	306.78	320.84	85.39	324.06
S = 11%	90	227.67	299.03.	697.8	314.31
Al = 39%	105	312.88	324.15	73.51	327.07
	150	310.47	320.36	41.44	324.28
	53	224.08	315.56	778.9	318.56
	63	312.2	326.12	290.6	330.52
KNO_3 = 53%	75	310.38	324.74	116.2	327.06
S =17%	90	313.79	328.80	232.6	331.13
Al = 30%		*331.84	*333.04	*28.16	*338.31
	105	315.53	326.22	78.03	329.57
	150	314.63	325.59	71.02	328.48
	53	314.38	327.20	336.7	330.64
	63	314.98	323.78	101.2	326.48
KNO_3 = 65%	75	313.03	326.82	223.2	329.8
S = 20%	90	314.3	326.63	146.2	329.65
Al = 15%	105	315.42	322.27	56.65	330.42
	150	314.27	328.63	195.3	330.92

* represents the DSC data for the second exothermic activity

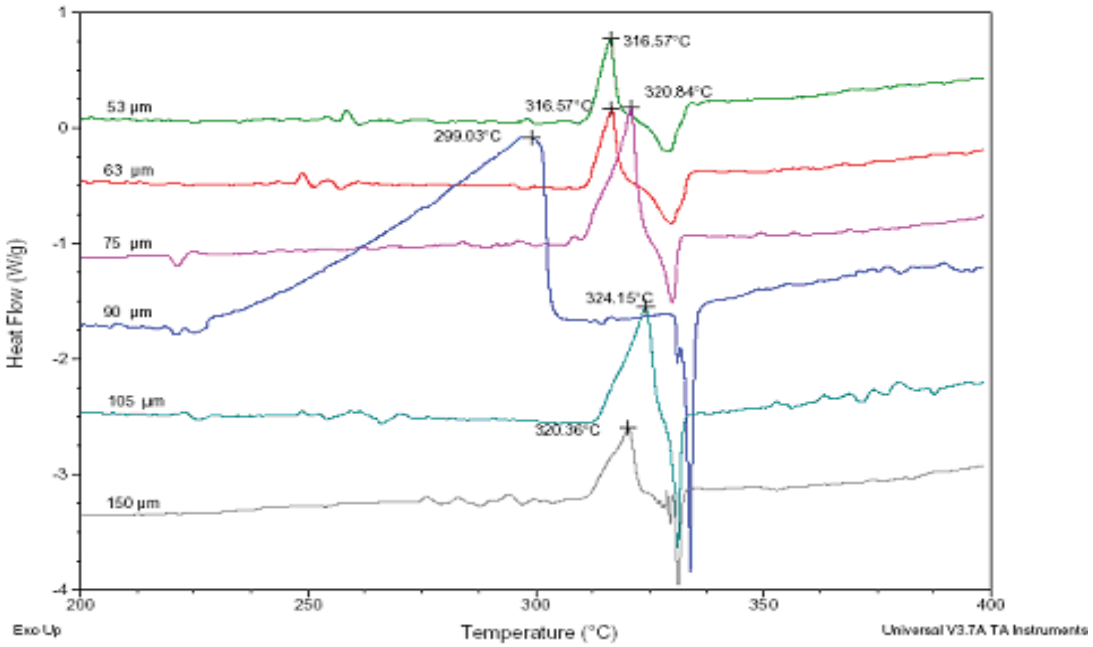

Figure 5 *DSC Plots showing the influence of KNO_3 particle size on thermal decomposition of a flash composition (KNO_3 = 50%, S = 11%, Al = 39%).*

and 333 °C was due to the prominent exothermic decomposition process. The concomitant endothermic peak with a peak maximum of 331 °C was due to melting (phase change) of unreacted KNO_3. Though the degree of exothermic activity was different with varying particle size, there was no specific trend or influence of particle size on the thermal decomposition.

A close examination of the DSC plot revealed that the decomposition process was a result of the physical and chemical processes occurring concomitantly. It appeared that the initial reaction process occurred in the solid phase (220 °C to 330 °C), until the endothermic melting of KNO_3, and hence the decomposition reaction could not proceed further at this temperature. The possibility of the existence of sulphur was remote and hence the decomposition process ended at this point.

The DSC plots (Figure 5) for the flash compositions consisting of 50% KNO_3, 11% S and 39% Al with varying particle sizes show a number of features in common, except for the one carried out with KNO_3 of 90 µm particle size. The 90 µm particle size mixture showed an early onset of thermal decomposition (227 °C) and the heat released was quite high as compared to the DSC plots of the remaining mixtures of varying particle sizes. Perhaps this oddity is because the flash compositions depend also on the particle shape and compactness of the chemical components. Though the changes in particle size in the mixture composition had a definite influence on the thermal decomposition, it was difficult to conclude which particle size and composition was the most ideal for flash composition manufacturing.

The influence of KNO_3 particle size on the thermal decomposition of a pyrotechnic mixture consisting of 53% KNO_3, 17% S and 30% Al was studied using DSC and the resulting plots were stacked according to the varying particle sizes (Figure 6). In case of the 53–63 µm sieve fraction, there was an earlier onset temperature for decomposition with the release of a high heat of reaction.

The influence of KNO_3 particle size on the thermal decomposition of a pyrotechnic mixture consisting of 65% KNO_3, 20% S and 15% Al was also studied using DSC and the resulting plots were stacked according to increasing particle size (Figure 7). This showed similar features to what was seen in the earlier compositions. Though a change was observed on increased KNO_3 particle sizes, the effect was not very significant.

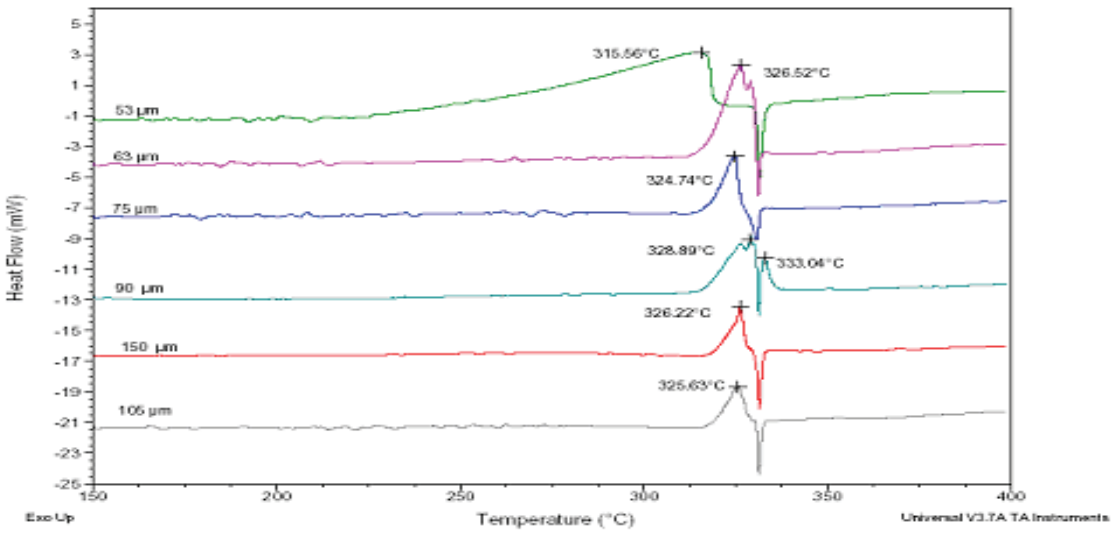

Figure 6 *DSC plots showing the influence of KNO_3 particle size on thermal decomposition of a flash composition (KNO_3 = 53%, S = 17%, Al = 30%).*

Effect of Al particle size on the thermal stability

Table 6 shows the influence of Al particle size on the thermal decomposition of the pyrotechnic mixture. The resulting plots were stacked according to the varying particle sizes (Figures 8, 9, 10). The onset of decomposition was generally found to be around 320 ºC for all particle sizes and the first process ended around 330 ºC. Here, in most cases, a second exotherm was observed immediately next to the endotherm at 331 ºC. The endothermic process recorded at the peak maximum temperature of 331 ºC was the melting of KNO_3 [reference Merck index]. DSC plots

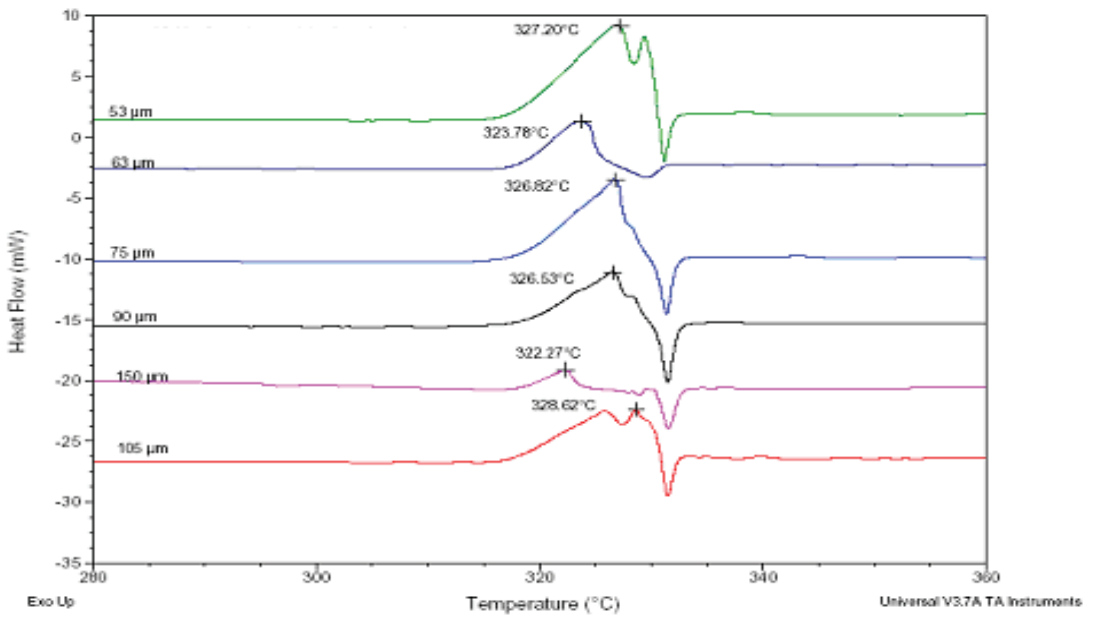

Figure 7 *DSC plots showing the influence of KNO_3 particle size on thermal decomposition of a flash composition (KNO_3 = 65%, S = 20%, Al = 15%).*

Table 6 *Effect of particle size of Al for the various mixtures of flash compositions on thermal sensitivity.*

Composition (wt%)	Particle Size of Al (μm)	Onset Temperature (ºC)	Peak Maximum Temperature (ºC)	Heat of Reaction (J g^{-1})	End Temperature (ºC)
KNO_3 = 50% S = 11% Al = 39%	37	220.03	332.75	263.2	331.8
	45	319.26	325.68	42.24	329.93
	53	319.82	326.65	27.84	330.77
		*331.54	*332.28	*11.03	*338.74
	63	320.62	325.84	47.65	329.91
	90	315.9	322.95	34.15	329.65
KNO_3 =53% S =17% Al =30%	37	318.71	326.82	76.7	330.95
		*332.25	*333.45	*12.5	*337.49
	45	312.10	329.77	105.5	330.87
		*332.15	*333.04	*81.43	*345.84
	53	316.78	328.84	101.5	330.82
		*317.28	*333.73	*23.43	*338.64
	63	319.91	326.24	66.5	330.9
	90	321.54	326.07	37.46	330.81
		*331.67	*332.68	*17.75	*339.99
KNO_3 =65% S =20% Al = 15%	37	317.69	326.35	79.87	329.91
	45	311.23	332.75	1007	353.77
	53	315.68	325.76	88.6	330.91
		*332.21	*334.29	*103.9	*353.54
	63	324.6	330.41	44.88	331.71
		*332.66	*338.45	*240.6	*363.17
	90	325	331.48	4.84	332.25
		*334.95	*343.07	*81.81	*353.72

* represents the DSC data for the second exothermic activity

also revealed that the decomposition process was the result of physical and chemical processes occurring concomitantly. The effect of particle size seemed to be inconsistent. It appeared that the initial reaction was taking place in the solid phase (220–330 ºC), until the endothermic melting of KNO_3. The concomitant reaction after KNO_3 melting appears to proceed in the liquid phase.

Figure 8 shows the DSC plot for flash compositions consisting of 50% KNO_3, 11% S and 39% Al with varying Al particle sizes. The second concomitant reaction could not be observed, because the first reaction could not provide enough enthalpy for the second reaction to proceed due to absorbance of the heat by the endothermic phase change. However, in some cases the second exothermic reaction could proceed. From Table 6, it was observed that the onset temperature increased with increase in particle size and remained constant. The decrease in the Al particle size increased the heat of reaction.

The influence of Al particle size on the thermal decomposition of pyrotechnic mixture consisting of 53% KNO_3, 17% S and 30% Al was studied using DSC and the resulting plots were stacked according to increasing particle size (Figure 9). In all the DSC runs with different particle sizes, the endothermic melting of potassium nitrate with concomitant second exothermic activity followed the first prominent exothermic peak.

The influence of Al particle size on the thermal decomposition of pyrotechnic mixture consisting

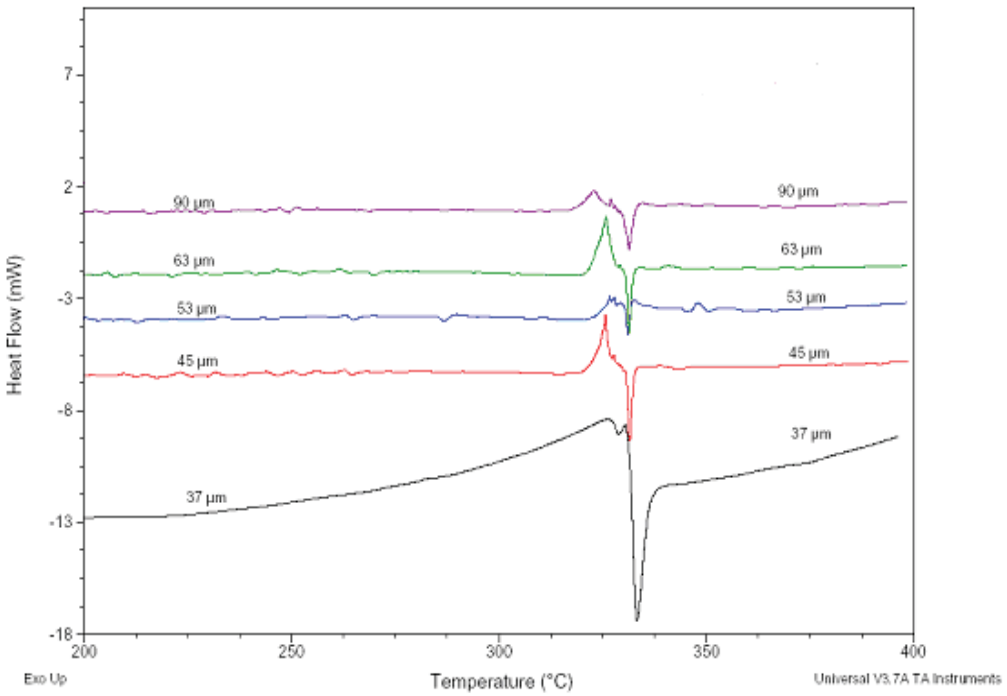

Figure 8 *DSC plots showing the influence of Al particle size on thermal decomposition of a flash composition (KNO_3 = 50%, S = 11%, Al = 39%).*

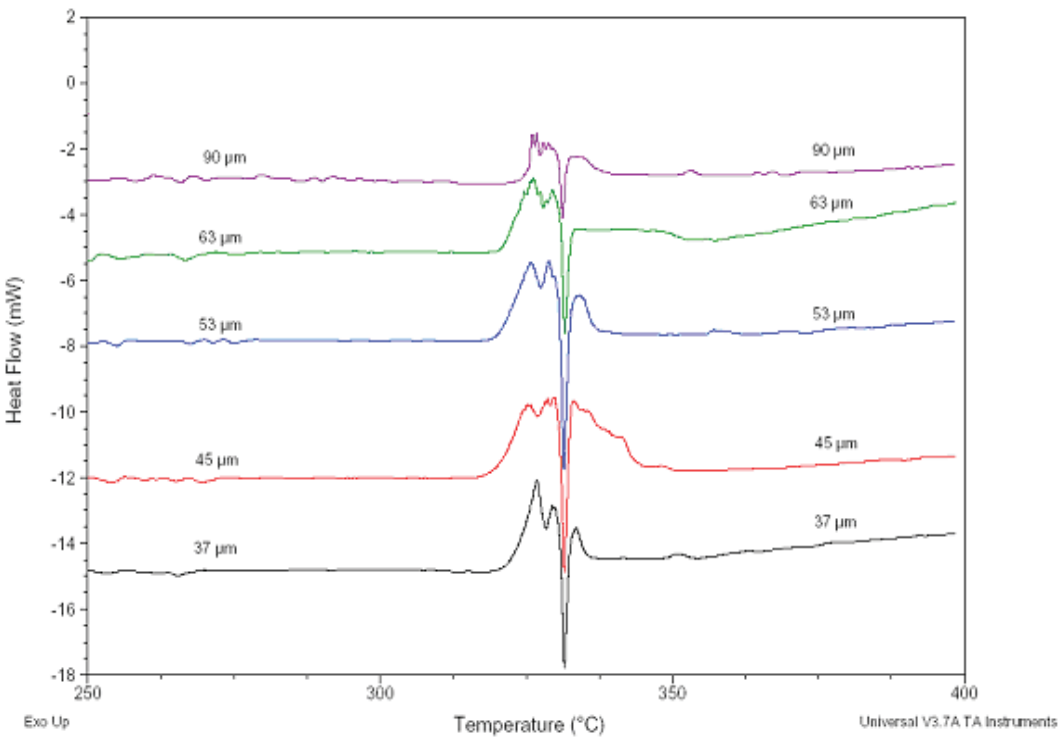

Figure 9 *DSC plots showing the influence of Al particle size on thermal decomposition of a flash composition (KNO_3 = 53%, S = 17%, Al = 30%).*

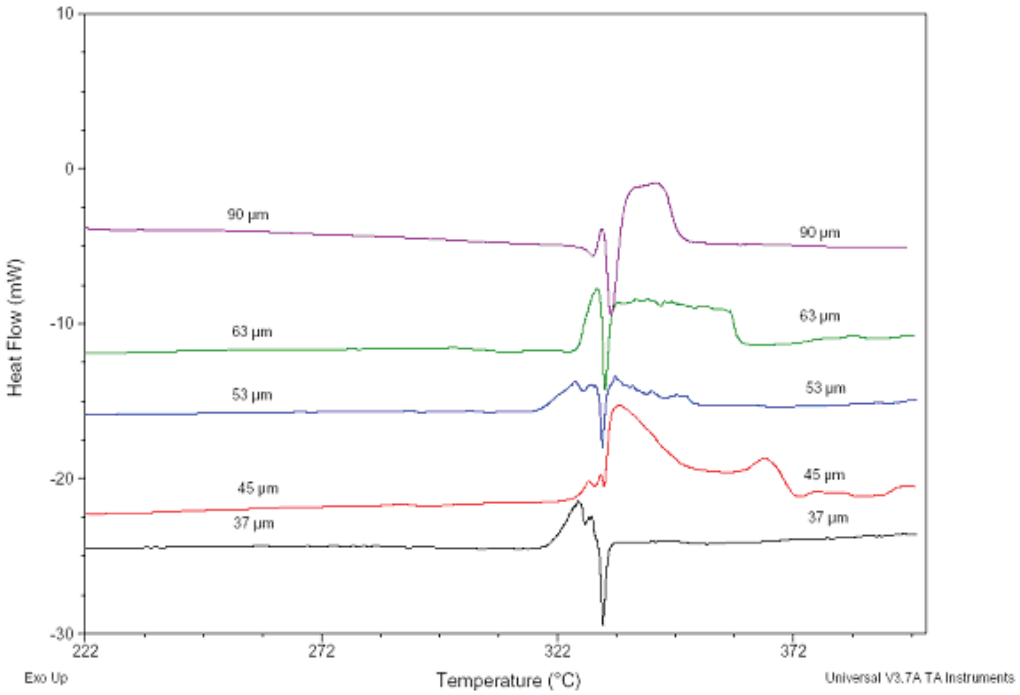

Figure 10 *DSC plots showing the influence of Al particle size on thermal decomposition of a flash composition (KNO_3 = 65%, S = 20%, Al = 15%).*

of 65% KNO_3, 20% S and 15% Al was studied using DSC and the resulting plots were stacked according to increasing particle size (Figure 10). The trend of the curve was similar to the two previous compositions except for the one with particle size of 45 µm. It was very interesting to note that the concentration of KNO_3 was the highest in the mixture and that all of them were involved in the thermal decomposition processes. As KNO_3 was the oxidizer in the flash composition a maximum amount of heat release was expected. The results are complex and it is difficult to interpret the role of each component in promoting the decomposition reaction.

Effect of Particle Size of KNO_3 (oxidizer) and Al (fuel) on Process Safety of Flash Composition

The mechanical sensitivity analysis showed that the decrease in particle size of KNO_3 had an adverse effect on sensitivity (both impact and friction) to a greater extent than the Al particle size had. However, the flash compositions studied could be categorized as class III explosives sensitive to impact.

The DSC studies showed that the decrease in particle size of KNO_3 and Al set the lowest onsets at around 220 ºC for the first exothermic activity. The chance of thermal hazard during the processing of flash compositions below the onset temperature of DSC, though remote, had to be so confirmed through the adiabatic calorimetric test. Given a margin of 100 ºC, it would be stated that below 120 ºC, the flash composition mixture would be stable provided there was no source of ignition or mechanical (impact/friction) effects of the flash composition.

The DSC studies on the effect of Al particle size showed that the decrease in Al particle size leads to a second exothermic activity. This behavior needs to be viewed with caution from the point of view of safety. The heat content from the first exothermic activity itself is enough to undergo good flash reaction by the mixture,[5] whereas the heat release due to the second exothermic activity is undesirable for the flash composition as this may lead to several cascading explosions. However, in order to improve the quality of cracking of flash composition, firework manufacturers generally tend to use finely divided Al powder in greater

quantities than necessary. DSC studies revealed that the use of finer Al powders in a flash composition would only lead to secondary exothermic activity culminating in accident situations of higher magnitude. This secondary exothermic activity can lead to secondary explosions in any hazardous situation during processing and storage of flash compositions as the quantities are going to be high.

Conclusions

Mechanical and thermal studies on the sensitivity of pyrotechnic flash compositions with varying KNO_3 and Al particle sizes indicated that all the flash compositions studied were found to be sensitive. As the KNO_3 particle size increased, the sensitiveness to impact initially decreased up to 63 µm and then increased. This was due to the fact that impact sensitivity depended not only on the flash composition and particle size but also on the particle shape, density and compactness of the chemicals. The friction sensitivity decreased with the increase in KNO_3 particle size. The lowest Al particle size exhibited high impact sensitivity compared with the higher particle sizes. But there was no appreciable effect on friction sensitivity with change in Al particle size.

The DSC studies on the effect of Al particle size showed that the decrease in Al particle size led to a second exothermic activity. Hence, the use of finer Al powders in a flash composition would only lead to secondary exothermic activity. This secondary exothermic activity can lead to secondary explosions in any hazardous situation during processing and storage of flash compositions.

Acknowledgements

S. P. Sivapirakasam is grateful to the management and Principal, Mepco Schlenk Engineering College, Sivakasi, for their constant encouragement. The author is also grateful to TIFAC, Department of Science and Technology, Government of India, New Delhi, for offering facilities to carry out this research. The authors are thankful to the Director, CLRI for their kind permission to carry out this study in CLRI.

References

1 M. Veeramani and S. P. Sivaprakasam, "Safe Storage and Handling of Pyrotechnic Chemicals", Indian Chemical Engineering Congress, Chennai, December 2002, p. 126.

2 S. P. Sivaprakasam, M. Surianarayanan, G. S. Venkataratnam and P. Nagaraj, "Hazard Evaluation Techniques for Fireworks Compositions", Indian Chemical Engineering Congress, Hyderabad, 19–22 December 2003, p. 126.

3 D. Chapman, R. K. Wharton and G. E. Williamson, "Studies of the Thermal Stability and Sensitiveness of Sulphur/ Chlorate mixtures part 1 – introductions", *Journal of Pyrotechnics*, No. 6, 1997, p. 30.

4 S. P. Sivaprakasam, M. Surianarayanan, G. S. Venkataratnam and P. Nagaraj, "Impact sensitiveness analysis of pyrotechnic flash compositions", *Journal of Pyrotechnics*, No. 21, 2005, p. 52.

5 S. P. Sivaprakasam, M. Surianarayanan, F. Chandrasekran and G. Swaminathan, "Thermal Hazards of Cracker Mixture using DSC", *Journal of Thermal Analysis and Calorimetry*, No. 78, 2004, p. 799.

6 D. Chapman, R. K. Wharton and J. E. Fletcher, "Studies of the thermal stability and sensitiveness of sulphur/chlorate mixtures part 3. The effect of stoichiometry, particle size and added materials", *Journal of Pyrotechnics*, No. 11, 2000, p. 16.

7 R. K. Wharton, R. P. Rapley and J. A. Harding, "The mechanical sensitiveness of Titanium/Black Powder Pyrotechnic Compositions", *Propellants, Explosives, Pyrotechnics*, No. 18, 1993, p. 25.

8 J. A. Conkling, *Chemistry of Pyrotechnics, Basic principles and theory*, Marcel Dekker, Inc., New York, 1985, p. 101.

9 L. V. de Yong and G. Wilson, "Comparison of several techniques for measuring the particle size of powder used in pyrotechnics", RAAF general ammunition department, Report NSW 2750, Australia, 1986.

10 J. H. McLain, *Pyrotechnics from the viewpoint of solid state chemistry*, Francklin Institute press, 1980, pp. 26–37.

11 John A. Conkling, “Ignition Sensitivity of Fireworks Composition”, Proceedings of the International Symposium on Fireworks, Montreal, Canada, 1992.

12 United Nations: Recommendations on the Transport of Dangerous Goods, Test and Criteria, section 21 (BAM Fall Hammer) ST/SG/AC.10/11/Rev.1. Second Edition New York (1990).

13 United Nations: Recommendations on the Transport of Dangerous Goods, Test and Criteria, Test 3(b) (i): BAM friction apparatus, ST/SG/AC.10/11/Rev.3, 3rd ed., New York, (1999)

14 Gyorgy Negyesi. “Sensitivity of Non-Explosive Compounds to Friction Testing”, Process Safety Progress, Vol.15, No.1, 1996, p. 42.

15 Andreiev-Beliave, ‘Theory of Explosives’, Banyagyutacsgyar, Budapest (in Hungarian) 1965

Interrelation Between Impact, Friction And Thermal Energy In A Pyrotechnic Flash Reaction

S. P. Sivapirakasam[a] and M. Surianarayanan[b]*

[a] TIFAC-CORE in Industrial Safety, Department of Mechanical Engineering,
Mepco Schlenk Engineering College, Sivakasi - 626 005, India.

[b] Cell for Industrial Safety & Risk Analysis, Chemical Engineering Department, Central Leather Research Institute,
(Council of Scientific & Industrial Research), Adyar, Chennai - 600 020, India.

* Corresponding author: email: msuri1@vsnl.com

Abstract: *Firework chemical mixtures are sensitive to thermal and mechanical stimuli and lead to many explosive incidents. Experimentally determined thermal and mechanical (impact and friction) sensitivity data of a flash composition mixture are subjected to statistical and graphical analysis in order to understand the mechanism of triggering accidents. The interrelationship study reveals that irrespective of the nature of stimuli, explosion is the final event and occurs due to a thermal mechanism. This study shows that under severe impact thermal stimuli can occur. If the thermal stimuli are equal to or greater than the activation energy of the composition then ignition of the flash composition will occur.*

Keywords: *flash composition, fireworks, mechanical and thermal sensitiveness, correlation analysis*

Introduction

During the firework manufacturing process, chemicals are initially mixed to produce a reasonably homogeneous blend of oxidizer, fuel, colour enhancing chemicals and binders. During these operations impact, friction, spark and heat stimuli may occur, and under certain conditions one or more of these stimuli may be enough to cause ignition of the composition. The sensitivity of the flash composition to these stimuli depends upon the chemical components, purity, particle size, moisture content and packing density. It is therefore extremely important to understand the sensitivity of the chemical mixture to external stimuli.

Studies on thermal stability,[1] impact sensitivity and friction sensitivity[2] of firework compositions have been reported. The reported information cannot be used directly for determining the safety limits for storage, processing, and transportation of firework compositions because no attempts have been made to study the thermal, mechanical and electrostatic hazards together to pinpoint the reasons for accidents to occur. However, in a few reported studies,[3–6] attempts to correlate the mechanical initiation of organic high explosives to kinetics of thermal decompositions are evident.

Ho and Fong[3] compared the impact sensitivity of the various propellants with the thermal decomposition data at 20 ºC min^{-1} and showed that the impact energy had a good correlation with thermal decomposition for the composite propellants with the same binder : oxidizer weight ratio. The results at 20 ºC min^{-1} were used for comparison so as to emphasize the thermal effect most pronounced under rapid heating conditions.

Wenograd[4] suggested that impact sensitivities of organic high explosives were governed by the thermal decomposition processes which took place at the widely varying temperature generated under the impact mass. He found that the temperature at which an explosion would occur within 250 microseconds (a time comparable to the interval under the impact mass) varied greatly among explosives.

Bowden[5] made efforts to study the mechanism of impact initiation. The authors suggested that initiations stemmed from hot spots in the explosive mass generated by a number of possible routes including viscous heating, frictional heating and adiabatic compression of entrapped gases. They concluded that to cause fires in PETN and NG, these hot spots must reach temperatures of at least 430–500 ºC.

Field *et al*.[6] suggested shear banding as a possible source of hot spot formation on impact. In this mechanism, localized plastic flow of material

following its structural collapse under compressive stress was related to hot spot formation.

Of all the firework compositions, flash compositions are real explosives that detonate, if a sufficient quantity of powder is present in bulk form, even if unconfined.[2] It is necessary to study the thermal, impact and friction sensitivity of these compositions so that the interrelation and the functioning of mechanical initiation to thermal decomposition can be understood. The work reported here is focused on this objective. Further in this paper, for the first time, Pearson's correlation analysis[7] has been employed to interrelate the mechanical and thermal decomposition parameters and the resulting data have been analyzed using graphical methods.

Experimental

Materials

The chemicals used for the preparation of the flash composition were of commercial grade and obtained from a firework manufacturing company situated in the southern part of Tamilnadu, India. The purity and assay of the chemicals were: KNO_3: 91.6%, S: 99.84% and Al: 99.71%. The chemicals were passed through a 100 mesh brass sieve. The samples were stored in an airtight container and kept away from light and moisture.

The mixture compositions varied in the range of 50–65% potassium nitrate, 5–20% sulphur, and 45–15% aluminum. The range was kept wide so as to cover the range of compositions employed in different fireworks industries in and around Tamilnadu, India.

Thermal studies under isothermal conditions

Intensive studies with the pyrotechnic flash compositions consisting of KNO_3, S and Al were carried out using Differential Scanning Calorimetry (DSC) to analyze their thermal stability and understand the importance of the role of varying proportions and particle size of pyrotechnic flash compositions in inducing cracking characteristics.

DSC module 2910 model (TA Instruments) was used for measurement of thermal stability for the different flash compositions. The studies were conducted with a sample size of 2 mg under pure nitrogen gas at a flow rate of 100 l min^{-1}. The equipment and the experimental conditions employed have been reported elsewhere.[1]

Thermal studies under adiabatic conditions

Thermal study of the flash compositions under adiabatic conditions was carried out using an Accelerated Rate Calorimeter (ARC). An ARC 1000 supplied by CSI of Austin, TX was used.[8] About 1 g of sample was loaded into a titanium bomb calorimeter and its temperature raised incrementally by 5 ºC min^{-1} under heat–wait–search mode, until a measurable rate of exothermic activity was detected (0.02 ºC min^{-1}) or the final temperature was attained without any positive thermal input.

Measurement of impact sensitivity

The impact sensitivity measurements of the flash compositions were carried out according to the procedure outlined in the United Nations (UN) Recommendations on the transport of dangerous goods.[9] The design and principle of the equipment were similar to those of a drop fall hammer of BAM standards. The details of the equipment employed have been presented elsewhere.[2]

Measurement of friction sensitivity

The friction sensitivity measurements of the flash compositions were carried out by BAM (friction tester) according to the procedure outlined in the United Nations (UN) Recommendations on the transport of dangerous goods.[10]

Correlation analysis[7]

If two variables vary such that change in one variable affects the change in the other variable, the variables are correlated. The degree of relationship between the variables under consideration is measured through correlation analysis. The measure of correlation is called the correlation coefficient or correlation index. Thus, correlation analysis refers to the techniques used in measuring the closeness of the relationship between the variables. Although there are several methods[11] of analyzing the correlations of physical and chemical sensitiveness, Pearson's coefficient of correlation is simple and highly reliable for measuring the degree of relationship between two variables. The correlation coefficient ρ between two random variables X and Y is given as follows (equation 1):

$$\rho = \frac{n\Sigma XY - \Sigma X \Sigma Y}{(n\Sigma X^2 - (\Sigma X)^2)(n\Sigma Y^2 - (\Sigma Y)^2)^{1/2}} \quad (1)$$

The value of the correlation coefficient ρ always lies between +1 and −1. A value of $\rho = 0$ indicates no correlation. If the value of ρ is near +1 then the variables X and Y are said to be positively correlated and if the value of ρ is near to −1 then the variables X and Y are said to be negatively correlated.

Results

Flash compositions under isothermal conditions

The results of the experiments conducted using DSC for the different flash compositions are presented in Table 1. The DSC plots of the flash compositions for varying sulphur concentration are shown in Figure 1. It can be seen that with increasing sulphur content, the onset temperature

Table 1 *Explosive parameters for the various flash compositions.*

Sample No.	Mixture Components (wt%)			Onset Temperature (ºC)	Peak Temperature (ºC)	ΔH (J g^{-1})	LIE (J)	Friction sensitivity (N)
	KNO_3	S	Al					
1	65	20	15	310.37	319.69	246.2	6.5	360
2	65	17	18	310.68	314.79	253.2	7.9	240
3	65	14	21	313.98	321.79	466.7	7	240
4	65	5	30	305.85	309.37	53.83	7.9	360
5	62	20	18	312.76	321.09	332.1	6	216
6	62	17	21	311.83	320.92	252.5	7.8	216
7	62	14	24	309.85	314.13	56.27	7.2	240
8	62	11	27	308.14	314.02	79.78	8.8	192
9	60	7.5	32.5	304.06	308.14	33.94	6.5	216
10	59	20	21	310.22	314.49	36.24	7.6	216
11	59	17	24	310.5	319.5	358.8	7.6	180
12	59	14	27	303.58	321	966.2	6.1	192
13	56	20	24	312.91	320.5	525.8	6	216
14	56	14	30	306.35	320.3	397.2	6.2	192
15	53	20	27	312.11	313.56	372.3	7.0	216
16	53	17	30	310.37	318.24	409.9	6.3	216
17	53	14	33	311.84	313.88	346	6.4	240
18	53	11	36	310.59	312.87	227.6	6.6	240
19	52.5	7.5	40	307.5	311.2	53.64	7.2	240
20	50	20	30	308.61	319.81	335.6	6.7	216
21	50	17	33	310.97	321.31	534.1	5.9	288
22	50	12.5	37.5	306.75	318.82	367.9	6.0	288
23	50	11	39	311.61	315.3	326.3	6.1	360

Table 2 *Summary of ARC data of flash composition.*

Thermal Inertia (Φ)	Onset Temperature T_o (ºC)	Final Temperature T_f (ºC)	Adiabatic temperature rise ΔT (ºC)	Absolute temperature rise ΔT_{ab} (ºC)	Heat of reaction ΔH_r (J g^{-1})
4.84	191	450	259	1253.6	1311.25

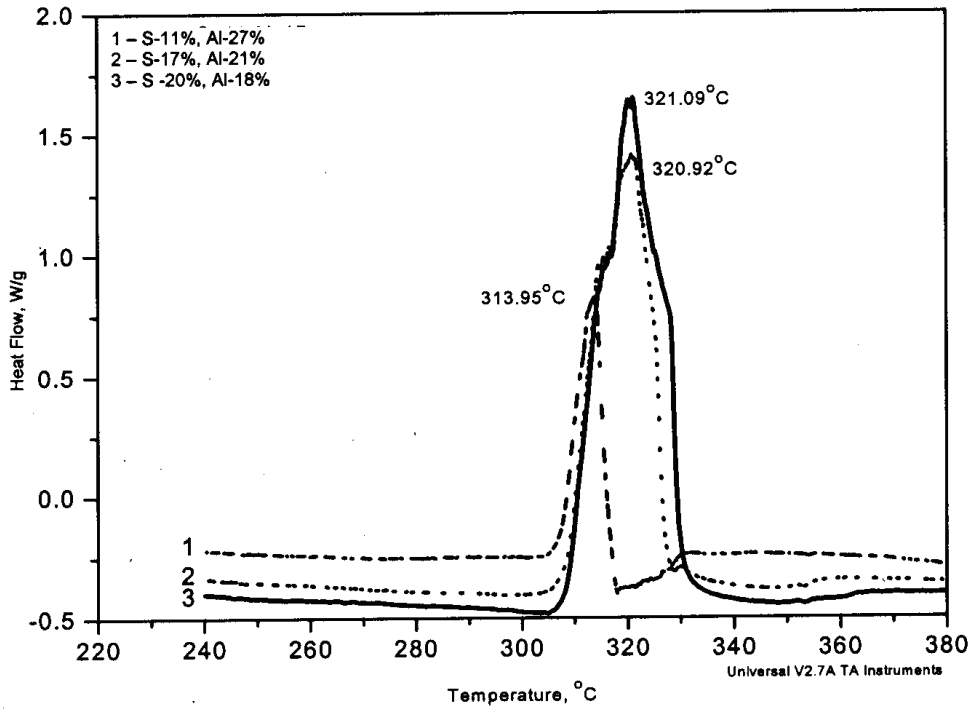

Figure 1 *DSC plots of pyrotechnic flash composition of varying sulphur content (KNO_3: 62% fixed).*

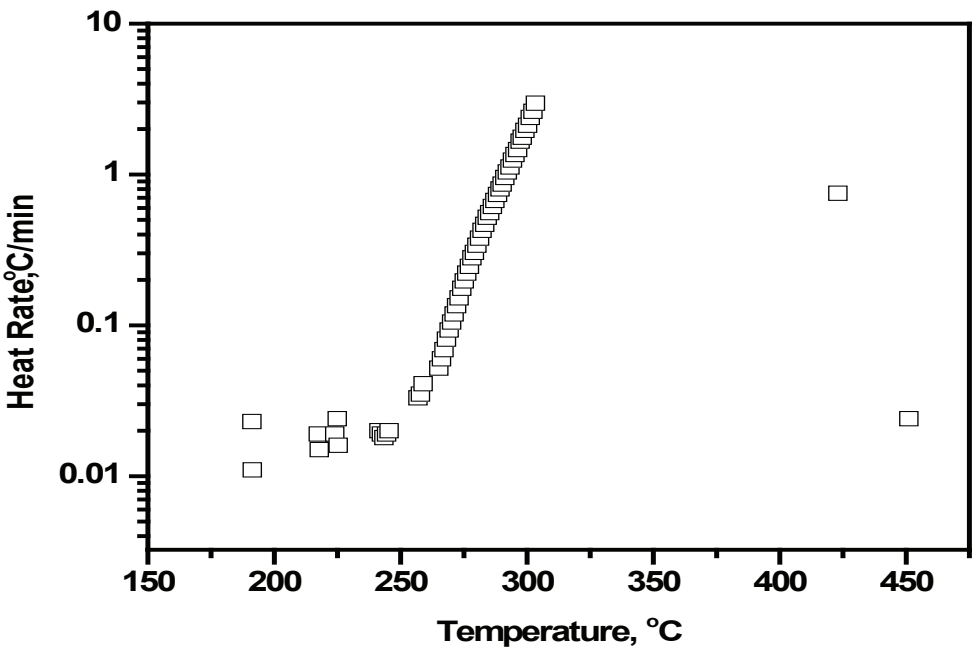

Figure 2 *Self-heat rate vs. temperature plot for thermal decomposition of flash composition (KNO_3 : S : Al 53 : 17 : 30).*

for exothermic decomposition advances to a higher value to increase the heat of decomposition.

Flash compositions under adiabatic conditions

The self-heat rate plot for thermal decomposition of flash composition consisting of potassium nitrate, sulfur, aluminum in the ratio of 53 : 17 : 30 is shown in Figure 2. ARC data are summarized in Table 2.

Mechanical sensitiveness of flash compositions

The results of mechanical sensitiveness (impact and friction) are shown in Table 1. The limiting Impact Energy (LIE) falls in the range of 5–8 J for the compositions studied, which may be categorized as class III explosives according to the 1965 classification by Andreieve-Beliaev.[2] The friction-limiting load falls in the range of 192–240 N for the compositions studied. The impact energy and friction-limiting load vary when the concentration of any one of the components of the mixture is changed. This behavior is due to the sensitivity and reactivity of each component.

Correlation analysis on mechanical sensitiveness and thermal decomposition

The results of thermal, impact and friction sensitivity data (Table 1) were subjected to Karl Pearson's correlation analysis to understand the

Table 3 *Correlation of mechanical sensitiveness and thermal decomposition parameters.*

Variables	Correlation coefficient	Significance
Limiting impact energy *vs.* onset temperature	+0.26	A weak positive correlation
Limiting impact energy *vs.* peak temperature	−0.6	A strong negative correlation
Limiting impact energy *vs.* heat of reaction	−0.6	A strong negative correlation
Friction sensitivity *vs.* onset temperature	+0.23	A weak positive correlation
Friction sensitivity *vs.* peak temperature	−0.13	A weak negative correlation
Friction sensitivity *vs.* heat of reaction	+0.17	A weak positive correlation

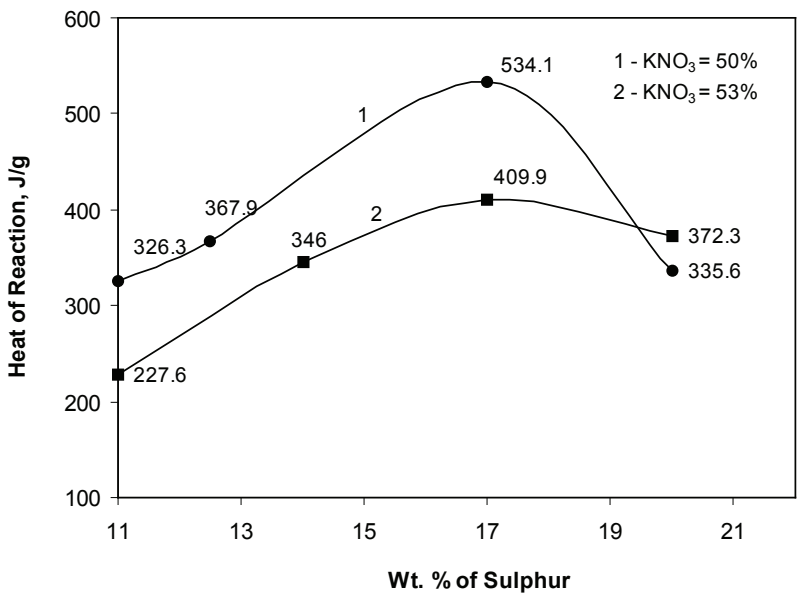

Figure 3 *Effect of sulphur concentration on the heat of decomposition of flash compositions.*

interrelation between the mechanical and thermal explosive sensitiveness.

Equation (1) was employed to determine the correlation coefficient ρ between impact friction and thermal sensitivity. The results are summarized in Table 3.

Discussion

The plot between the decomposition energy and sulphur concentration (Figure 3) showed that with increasing sulphur concentration, the decomposition energy (H decomposition) release increased and reached a maximum value at 17% concentration. Above this, the H decomposition decreased, perhaps due to an increase in concentration of other two components. Table 1 show that the flash composition was found to have explosive characteristics between 11 and 20% of sulphur concentration. Thus, sulphur concentration in the flash composition appeared not only critical, but should also be around the optimum level to exhibit good flash properties. The onset temperature in DSC was above 303 ºC (Table 1). However, the reactive potential of flash composition under adiabatic conditions was severe, and a lower onset for decomposition was recorded as 191 ºC (Table 2). A peak self-heating rate of 2.625 ºC min^{-1} was registered at 302 ºC. The adiabatic temperature rise for the process was 260 ºC. Under adiabatic conditions flash compositions decomposed slowly until 250 ºC (1700 min) (Figure 2), and beyond this the rise in temperature was sudden and sharp. This showed that, under adiabatic conditions, flash composition underwent vigorous decomposition.

Interrelation between limiting impact energy and thermal decomposition

The results of correlation analysis are summarized in Table 3. The strong negative correlation between LIE and ΔH and peak temperature is an indication of the fact that a pyrotechnic mixture, when subjected to an impact force, is triggered to an energetic response *i.e*. it explodes. In Figure 4 the interrelation between LIE and ΔH is graphically shown. It can be seen from the graph that, within the experiments conducted, ΔH increases with the concentration of KNO_3 to a maximum of 59%; between 59 and 62% ΔH drops to its minimum; beyond 62% KNO_3 ΔH increases again. Moreover, with increase in concentration of KNO_3, the impact energy initially decreases and later there is a rapid increase in impact energy before it decreases again. A close examination of the graph reveals that there is an inverse relationship between LIE and ΔH. That is, at lower impact energy (higher sensitivity), ΔH released is higher. This shows that the degree of energetic response is dependent on

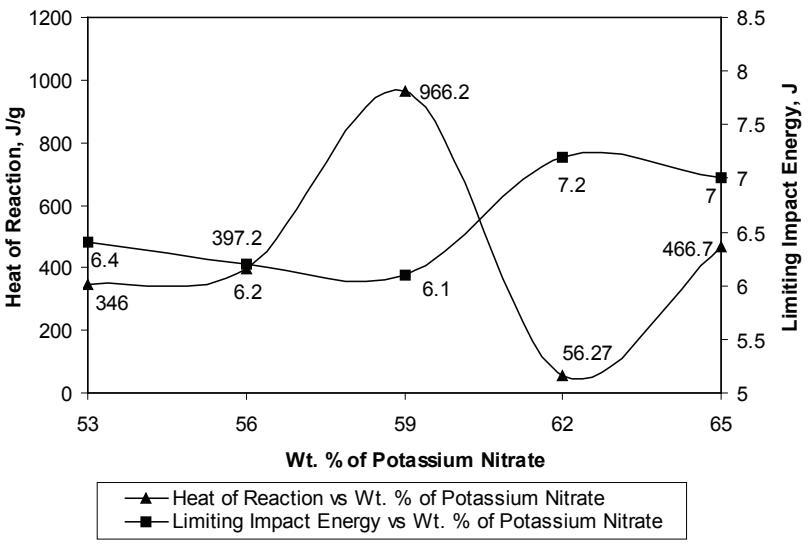

Figure 4 *Interrelation between heat of reaction and impact energy of flash composition at fixed S = 14 wt%.*

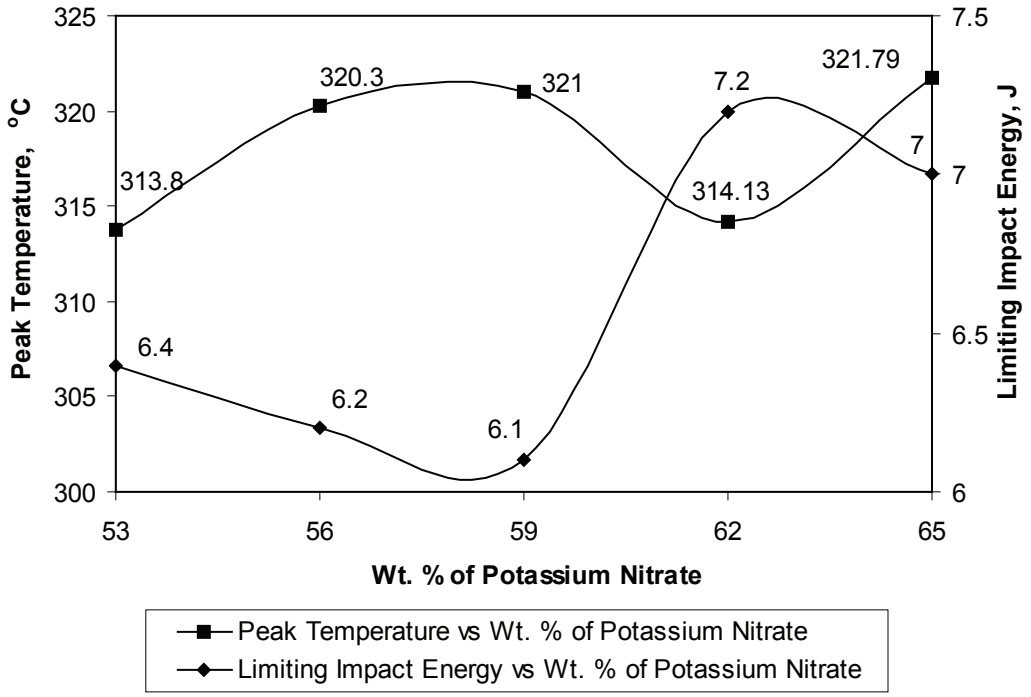

Figure 5 *Interrelation between peak temperature and limiting impact energy of flash composition at fixed S = 14%.*

the concentration of mixture constituents and not the impact force.

In Figure 5, the interrelation between LIE and peak temperature of flash compositions at a fixed sulphur concentration (14 wt%) is graphically shown. It can be seen that higher impact sensitivity leads to higher peak temperature.

From Table 3, the weak positive correlation of the impact energy to onset temperature can be attributed to the fact that the temperature generated through impact energy should be more than that of the onset temperature for the ignition to occur. In the impact sensitivity experimental measurement, the impact energy is measured when the explosion occurs. It is noted that the time factor between the applied impact force and explosion occurring is sudden and almost instantaneous, and may be of the order of microseconds (up to 250 microseconds for most high explosives[4]). In the thermal treatment of the composition under adiabatic conditions, it is seen that sudden and instantaneous explosion is achievable only when the temperature on the mixture is raised to a temperature beyond 302 ºC for the flash compositions (self-heat rate plot Figure 2).

Therefore, it is hypothesized that in impact sensitivity measurement, the temperature generated under impact mass should be more than the temperature of 302 ºC for the sudden and instantaneous explosion to occur. However, this does not mean that explosion will not occur when the impact force produces a temperature lower than 302 ºC (under conditions of less impact). Flash composition is known to undergo a sort of self-heating type of explosive decomposition as observed in the ARC studies. In a practical situation, where the impact force can produce an initial temperature of 191 ºC (development of hot spots) the onset of explosion may occur, however there is some induction time before it reaches the critical temperature of 302 ºC. Therefore, any impact force that contributes to rise in temperature of flash composition around 191 ºC or more is certainly dangerous. Further, the vigor and induction time of the explosion primarily depend on the compactness, density and particle size of the mixture.

There is no direct correlation between thermal and

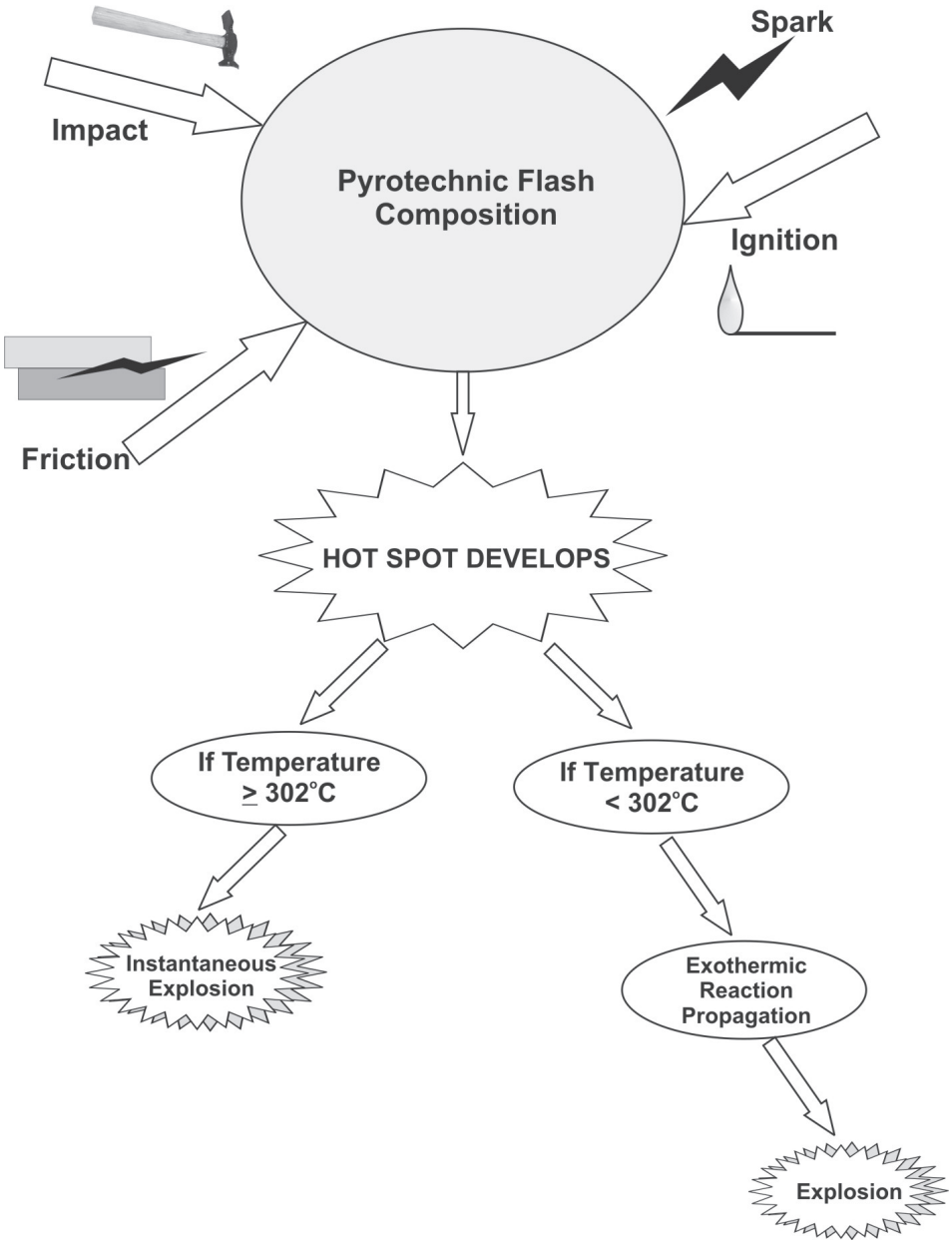

Figure 6 *Flow chart showing the initiation mechanism for explosive decomposition of pyrotechnic flash composition.*

impact sensitiveness, to either predict one from the other or to predict which of these forces can come together to trigger a thermal explosion. It is hypothesized that impact stimuli cause thermal stimuli for the flash composition to undergo thermal explosion. Under severe impact, thermal stimuli can occur immediately and lead to a catastrophic thermal explosion. Irrespective of the nature of the stimulus, explosion occurs through thermal mechanism only. This means that the impact or other kind of stimulus can only initiate the thermal mechanism by providing the minimum threshold energy needed/necessary to a reaction temperature of 191 ºC observed experimentally as the onset point for thermal explosion in ARC. Figure 6 shows the initiation mechanism for explosive decomposition of a pyrotechnic flash composition arising from various stimuli. It is thus possible to interrelate the mechanical form of energy leading to the threshold energy (ΔE) observed in the ARC. This provides a means of suggesting a predictive correlation in such explosive systems. The degree

of explosivity also depends on other factors such as compactness, particle size and shape and other environmental conditions.

The impact energy has generally been considered to be insufficient to heat the whole pyrotechnic charge to adiabatic temperature. This may mean that the initiating mechanism is most likely to be manifested under impact pressure due to the following factors:

1. Adiabatic compression of trapped gas.
2. Viscous heating of material rapidly extruded between impacting surfaces or grains.
3. Friction between impacting surfaces, the explosive materials and/or grit particles in the explosive layer.
4. Localized adiabatic shear of the materials during mechanical fail.

Correlation for the flash composition shows that there exists a relation between LIE, ΔH and peak temperature. It can be concluded that flash composition mixtures sensitive to impact will also be thermally sensitive and the higher the impact sensitivity, the higher the heat of reaction will be. The degree of energetic response will primarily depend on the mixture compositions and not on impact pressure. A minimum of 302 ºC is required for the instantaneous thermal decomposition under impact pressure for a flash composition. However, any impact force which contributes to a rise in the temperature of flash composition around 191 ºC or more is certainly dangerous. This is because flash composition mixture is known to undergo a self-heating type of explosive decomposition as observed in ARC studies.

Interrelation between friction sensitiveness and thermal decomposition

It can be seen from Table 3 that the friction sensitivity and thermal decomposition are weakly correlated. It is difficult to offer any scientific explanation at this stage; an acceptable reason may be the lack of precision in the measurement of friction sensitiveness. In the BAM friction sensitiveness measurement apparatus (employed in this study) the pyrotechnic mixtures are subjected to a localized frictional load and do not cover the entire sample subjected to the test. Considering the physical nature of the sample and the expected chemical mechanism available for reaction, the friction sensitivity data obtained may not be a true representation of real life situations. Further work is in progress.

Conclusions

The correlation analysis has proved that there exists a relation between impact and thermal sensitiveness for a pyrotechnic flash composition. The inverse relationship between limiting impact energy and heat of reaction shows that the degree of energetic response is dependent on the concentration of mixture constituents and not the impact force. Higher impact sensitivity leads to higher peak temperature during thermal stimuli. The correlation analysis has also predicted that flash composition mixture sensitive to impact will also be thermally sensitive. Further it is hypothesized that impact stimuli cause thermal stimuli for the flash composition to undergo thermal explosion. Under severe impact, thermal stimuli can occur immediately, leading to ignition of compositions. Thus through this correlation analysis, a satisfactory explanation could be projected for an accident triggering mechanism. Further research is required to relate the numerical factors (onset temperature, heat of reaction, limiting impact energy) to gain a thorough understanding of the accident triggering mechanism.

Acknowledgements

S. P. Sivapirakasam is grateful to the management and Principal, Mepco Schlenk Engineering College, Sivakasi, Tamilnadu, India, for their constant encouragement. The author is also grateful to TIFAC, Department of Science Technology, Government of India for offering facilities to carry out this research. The authors are thankful to Mr T. Baskaran, Technician of the Institute, for his assistance while carrying out the impact sensitivity experiments. The authors are thankful to the Head, Chemical Engineering Department and Director, CLRI Chennai, 600020, India, for their kind permission to carry out this study at CLRI.

References

1 S. P. Sivaprakasam, M. Surianarayanan, F. Chandrasekran and G. Swaminathan, "Thermal Hazards of Cracker Mixture using DSC", *Journal of Thermal Analysis and*

Calorimetry, No. 78, 2004, p. 799.

2 S. P. Sivaprakasam, M. Surianarayanan, G. S. Venkataratnam and P. Nagaraj, "Impact sensitiveness analysis of pyrotechnic flash compositions ", *Journal of Pyrotechnics*, No. 21, 2005, p. 52.

3 S. Y. Ho and C. W. Fong, "Relationship between impact ignition sensitivity and kinetics of the thermal decomposition of solid propellants".

4 J.Wenograd, *Transactions of the Faraday Society*, vol. 57, 1961, p. 1612.

5 F. P. Bowden and A. D. Yoffee, *Initiation and growth of explosion in liquid and solids*, Cambridge University Press, Cambridge, 1952.

6 J. E. Field, G. M. Swallowe and S. N. Heavens, "Ignition mechanism of explosives during mechanical deformation", *Proceedings of the Royal Society of London*, vol. A382, 1982, pp. 231–244.

7 K. Murugesan, *Probability and Statistics and Random Processes*, Anuradha Agencies, p. 54.

8 Y. Iizuka and M. Surianarayanan "Comprehensive Kinetic Model for Adiabatic Decomposition of Di-tert-butyl Peroxide Using BatchCAD", *Industrial & Engineering Chemistry Research*, vol. 42, No. 13, 2003, pp. 2987–2995.

9 United Nations: Recommendations on the Transport of Dangerous Goods, Test and Criteria, section 21 (BAM Fall Hammer) ST/SG/AC.10/11/Rev. 1, 2nd edn., New York, 1990.

10 United Nations: Recommendations on the Transport of Dangerous Goods, Test and Criteria, Test 3(b) (i): BAM friction apparatus, ST/SG/AC.10/11/Rev. 3, 3rd edn., New York, 1999.

11 S. P. Gupta, *Probability and Statistics for Engineers*.

Thermal Characterization And Kinetic Modeling Of A Pyrotechnic Flash Composition Under Adiabatic Conditions

S. P. Sivapirakasam,[a] M. Surianarayanan[b]* and R. Vijayaraghavan[b]

[a] TIFAC-CORE in Industrial Safety,
Department of Mechanical Engineering,
Mepco Schlenk Engineering College, Sivakasi - 626 005, India

[b] Cell for Industrial Safety and Risk Analysis,
Central Leather Research Institute
Chennai - 600 020, India
*Corresponding author: email: msuri1@vsnl.com

Abstract: *A pyrotechnic flash composition consisting of 53% KNO_3, 30% Al and 17% S is subjected to Accelerating Rate Calorimetry (ARC) studies. The onset point for thermal explosion is 191 ºC resulting in the generation of a considerable quantity of gaseous products. The mixture is vulnerable to thermal hazards. There is good agreement between the predicted and experimental self-heat rates determined using adiabatic thermo kinetics.*

Keywords: *Flash composition, ARC, fireworks, adiabatic thermo kinetics, thermal characterization*

Introduction

In recent years, frequent accidents during processing, storage and transportation have been reported in the fireworks industry.[1] This is of great concern because large quantities of different types of fireworks are manufactured in India and demand for them is steadily increasing. Generally, the composition of fireworks is a mixture of oxidizer, fuel, igniter, binder and color enhancing chemicals. These mixtures have high sensitivity to temperature, impact, friction and electrostatic stimuli. A thorough knowledge of thermal stability, auto-ignition temperature, impact sensitivity, frictional sensitivity and electrostatic sensitivity of these mixtures is imperative to assess the hazard potential.[2] Also, it should lead to a suitable plan for safety during processing, storage and transportation.

Chemical reactions of pyrotechnics produce large amounts of heat when confined to a closed system and result in thermal explosion. Although there are numerous thermal measurement techniques available to characterize the hazardous nature of pyrotechnic mixtures, Accelerating Rate Calorimetry (ARC) is the only adiabatic and versatile calorimetry that produces reliable data. Because ARC measurements are conducted adiabatically (*i.e.* no heat losses), the result can be effectively correlated with the behavior of energetic materials in bulk. The information obtained from ARC experiments relates to the onset temperature, self-heat rates and pressure activation energy for an exothermic reaction. The ARC data can be used to set ceiling temperatures and pressures for safe operation, storage and transportation.

In the past, researchers have studied the thermal stability and kinetics of pyrotechnic mixtures using Differential Scanning Calorimetry (DSC).[3] The thermal data obtained from DSC could not be used for determining safe operating temperatures due to the uncertainties associated with the very small quantity of samples (2–5 mg) used in the experiments and poor reproducibility of results and non-adiabatic experimental conditions. Subjecting flash composition mixtures to ARC studies would throw light on the behavior of these samples under adiabatic conditions; *i.e.*, under conditions of bulk storage, handling and transportation. Such a study has not been attempted, except for a theoretical paper detailing the suitability of ARC for studying the thermal decomposition of pyrotechnic mixtures.[4] In the present study the thermal data from ARC and the thermo kinetics of a pyrotechnic flash mixture consisting of potassium nitrate (KNO_3), sulphur (S), and aluminum (Al) have been studied.

Experimental

Materials: Preparation of flash composition mixture

The chemicals used in this study were of commercial grade and obtained from a fireworks chemical manufacturing company situated in southern Tamilnadu, India. The purity and assay of the chemicals were KNO_3: 91.6%, S: 99.84% and Al: 99.1%. The flash composition consisting of potassium nitrate, sulphur and aluminum in the ratio of 53 : 17 : 30 was mixed using a wooden spatula in a non-flammable container, and each time a sample size of 1 g was prepared. The sample was then stored in an airtight container and kept away from light and moisture sources.

Method: Accelerating Rate Calorimeter (ARC) experiments

The ARC used in this study was an ARC 1000 supplied by CSI of Austin, TX. The working principle, design description, and operational details of ARC are well cited in the literature.[6] ARC measurements were made using a titanium sample vessel in heat–wait–search mode. Before loading of the sample, the bomb was flushed with inert nitrogen gas and precautions were taken not to allow air to enter during the sample loading as well as during attachment of the sample vessel to the instrument. After connection, the sample vessel was pressurized to 2500 psi nitrogen gas to ensure that there was no leak and that the air in the assembly was replaced. The instrument was switched to step mode at an initial temperature of 80 ºC, and a wait time of 15 min was set prior to entering the search mode. About 1 g of sample was loaded into the titanium bomb of the calorimeter, and its temperature was raised incrementally by 5 ºC min^{-1} in heat–wait–search mode, until a measurable rate of exothermic activity was detected (0.02 ºC min^{-1}) or the final temperature was attained without any positive thermal input. The self-heat rate, time, temperature, and pressure data were obtained as ARC output.

Overview of adiabatic thermo kinetics[6]

The first assumption in the interpretation of ARC experimental data is the representation of concentration in terms of temperature differences. The equivalence of temperature and concentration for a simple well-defined chemical reaction is established using the ratio:

$$\frac{C}{C_0} = \frac{T_F - T}{T_F - T_0} = \frac{T_F - T}{\Delta T} \qquad (1)$$

where C is the concentration of the reacting substance and T is the temperature. The subscript 0 indicates some initial condition, and F a final state in which the substance has been consumed. Then $\Delta T = T_F - T_0$ is the temperature rise for the reaction. It is also equal to the ratio of enthalpy to average specific heat. In this relation the disappearance of the reacting species produces a proportionate increase in the heat energy. The heat of reaction, ΔH can be calculated from

$$\Delta H = m\overline{C}_P \Delta T$$

where $\overline{C}_P$ is the average heat capacity, and m is the mass of the sample.

The heat generated in an exothermic reaction is used in three ways *viz*., to heat the material, the container or bomb and the surroundings. The heat being used up in heating the sample mass depends on the specific heat. The proportion of heat used in heating the container is called thermal inertia (ϕ), which is expressed as ϕ = [heat capacity of sample (S) and container or bomb (B)]/[heat capacity of sample].

$$\phi = \frac{m_s \overline{C}_{ps} + m_B \overline{C}_{pB}}{m_s \overline{C}_{ps}}$$

$$\phi = 1 + \frac{m_b \overline{C}_{pB}}{m_s \overline{C}_{ps}} \qquad (2)$$

Incorporating the effects of thermal inertia (ϕ), the corrected heat of reaction ΔH_r is calculated using equation (3):

$$\Delta H_r = \phi m \overline{C}_P \Delta T \qquad (3)$$

The question that is basic to the study of the relationship of time to explosion is the measurement and extrapolation of data. Extrapolation must involve a concept of concentration since no material can continue to self-heat forever. The time dependence of concentration for an *N*th order reaction rate is expressed as follows:

$$\frac{-dC}{dt} = kC^N \qquad (4)$$

where C is the concentration, k is the rate coefficient and t is the time. When equations (1) and (4) are used, additional temperature dependence appears.

$$\frac{\mathrm{d}C}{\mathrm{d}t} = C_0 \frac{\mathrm{d}}{\mathrm{d}t}\left(\frac{T_\mathrm{F} - T}{\Delta T}\right) = \frac{-C_0}{\Delta T} \cdot \frac{\mathrm{d}T}{\mathrm{d}t}$$

$$m_T = \frac{\mathrm{d}T}{\mathrm{d}t} = k\left(\frac{T_\mathrm{F} - T}{\Delta T}\right)^N \cdot C_0^{N-1} \cdot \Delta T \qquad (5)$$

Here m_T is defined as the rate of temperature increase (or slope of the graph of T *vs.* t), *i.e.* the self-heat rate. To remove this extra temperature dependence, a modified rate is defined as the pseudo rate constant, k^*. It is defined in such a way that its dimensions for any order reaction are reciprocal of time.

$$k^* = k.C_0^{N-1} = \frac{m_T}{\Delta T} \cdot \left(\frac{\Delta T}{T_F - T}\right)^N \qquad (6)$$

In practice, k^* is evaluated from experimental data using the right hand side of the expression. With the proper choice of N, k^* has the same temperature dependence as k and yields a straight-line graph.

The Arrhenius relationship for determining the rate coefficients is

$$k = Ae^{\left(\frac{-\Delta E}{RT}\right)} \qquad (7)$$

where T is the absolute temperature in Kelvin, E is the activation energy, R is the universal gas constant and A is the pre-exponential factor. The ln k^* *vs.* $1/T$ plot yields a straight line with the proper choice of N. The activation energy and the pre-exponential factor are calculated by the following expressions:

$$\Delta E = \frac{RT_1T_2}{T_2 - T_1} \ln \frac{k^*_2}{k^*_1} \qquad (8)$$

$$\ln A = \ln \frac{k^*_1}{60} + \frac{\Delta E}{RT} \qquad (9)$$

Results and Discussion

Flash composition under adiabatic conditions

The self-heat rate plot for thermal decomposition of flash composition consisting of potassium nitrate, sulfur, aluminum in the ratio of 53 : 17 : 30 is shown in Figure 1 and the results are summarized in Table 1. The onset for reaction occurred at 191 °C and extended until 450 °C. A maximum self-heating rate of 2.625 °C min^{-1} occurred at 302 °C. The adiabatic temperature rise for the process was 259 °C. Under adiabatic conditions flash compositions decomposed slowly until 1700 min (250 °C) (Figure 2) and beyond this the rise in temperature was sudden and sharp as indicated in Figures 1 and 2. The reaction process was also accompanied by a considerable pressure rise (Figure 3); the peak pressure observed was 34 psi (2.312 bar) at 450 °C. As per equation (3), the heat of reaction was calculated as 1.311×10^3 J g^{-1}, which is found to be more than the value of 409 J g^{-1} obtained under isothermal conditions.[3] The ARC data showed that the pyrotechnic decomposition process under adiabatic condition was vigorous and therefore dangerous.

Thermo kinetics of flash composition

First order model (*i.e.* $N = 1$) kinetics were assumed for the decomposition of pyrotechnic flash composition. For $N = 1$ equation (6) becomes

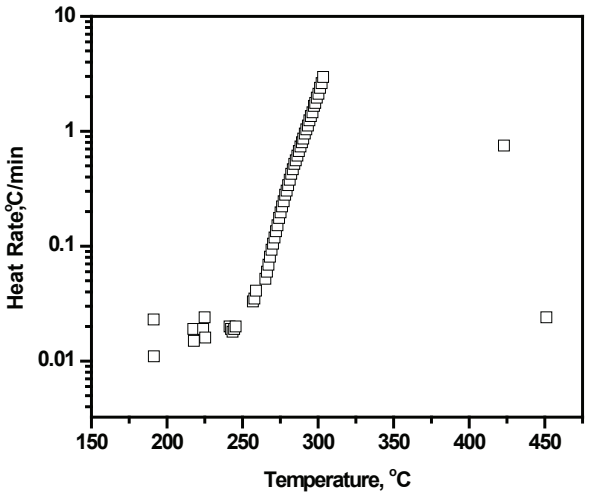

Figure 1 *Self-heat rate vs. temperature plot for thermal decomposition of flash composition (KNO_3 : S : Al; 53 : 17 : 30).*

Table 1 *Summary of ARC data of flash composition.*

Thermal inertia (Φ)	Onset Temperature T_o (°C)	Final Temperature T_f (°C)	Adiabatic temperature rise ΔT(°C)	Absolute temperature rise ΔT_{ab} (°C)	Heat of reaction ΔH_r (J g^{-1})
4.84	191	450	259	1253.6	1.311×10^3

$$k^* = k = m_t/(T_F - T) \quad (10)$$

Pseudo rate constants (k^*) were calculated using equation (10). Then ln k^* *versus* the inverse of temperature was plotted and the plot obtained is shown Figure 4. The straight line obtained confirms the assumption that the flash composition mixture follows first order kinetics.

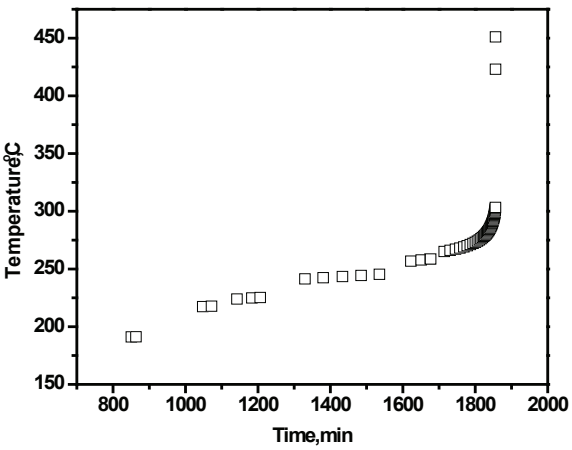

Figure 2 *Time vs. temperature plot for thermal decomposition of flash composition (KNO_3 : S : Al; 53 : 17 : 30).*

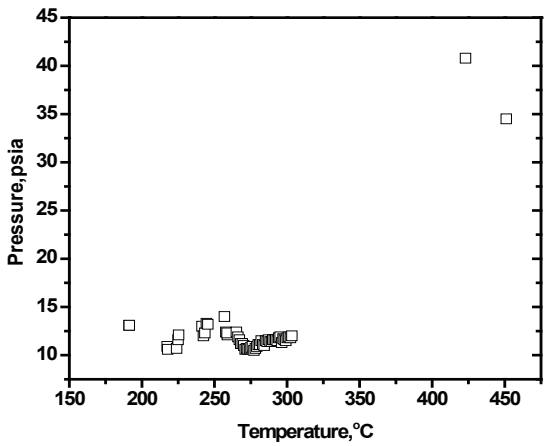

Figure 3 *Temperature vs. pressure plot for thermal decomposition of flash composition (KNO_3 : S : Al; 53 : 17 : 30).*

The slope of the plot is equal to $\Delta E/R$. As per equation (8), the activation energy was calculated as 63.99 kcal mol^{-1} (268 kJ mol^{-1}). It is seen that the activation energy obtained under adiabatic conditions is close to those found under isothermal conditions (199.7 kJ mol^{-1}) reported by us elsewhere.[3] This shows decomposition under isothermal and adiabatic condition operates on the same mechanism. Using equation (9), the pre-exponential factor was evaluated as 6.13×10^{20}. Thus the Arrhenius rate law for thermal decomposition of flash composition can be given as

$$k = 6.13 \times 10^{20} \exp\left(-\frac{268}{RT}\right) \quad (11)$$

Thermo kinetics

The heat rates determined using equation (11) have been compared with the experimentally observed heat rates and the results are shown in Figure 5. A

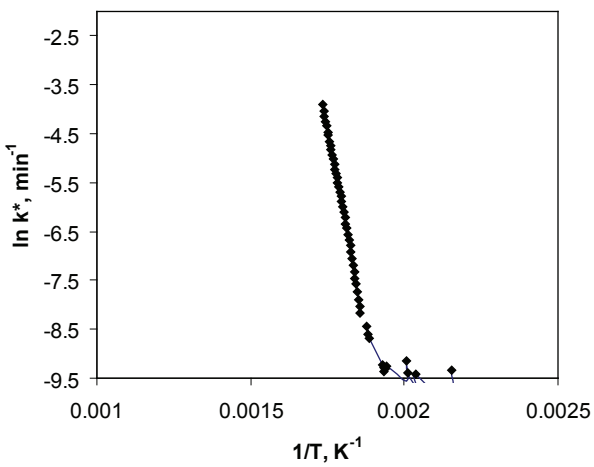

Figure 4 *Pseudo rate constant plot for the adiabatic thermal decomposition of flash composition (KNO_3 : S : Al; 53 : 17 : 30).*

close examination of Figure 5 indicates that there is good agreement between the experimental and predicted values. It can be observed now that the kinetics obtained in this study are highly reliable.

Process safety

Pyrotechnic mixtures are vulnerable to thermal hazards. ARC data are used for determining the ceiling temperature for processing, handling and transportation of hazardous materials. Accordingly the practice adopted is that the process/handling temperature should be 100 °C below the onset temperature observed in ARC.[7,8] This rule has been in practice in the process chemical industry for the safe and successful operation of process plants, storage systems and transportation. On these considerations, in the case of flash composition the ceiling temperature should never exceed 91 °C. Although there is no possibility of reaching this temperature during normal mixing[9] and packing processes of flash composition, this temperature can be achieved under situations like heat radiation from a neighboring area or ignition from unknown sources. During such abnormal situations the flash composition mixture is vulnerable to hazard.

Further, impact and friction sensitivities can also lead to triggering of explosive decompositions. There is no direct correlation available between thermal, impact and frictional sensitiveness, either to predict one from the other or to predict which of these forces can come together to trigger a thermal explosion. We hypothesize that an impact or frictional stimulus brings about a thermal stimulus for the flash composition to undergo thermal explosion. Under severe impact or friction stimuli, thermal stimuli can occur immediately, and this can lead to a catastrophic thermal explosion. Irrespective of the nature of the stimulus, explosion occurs through a thermal mechanism only. This means that, for the current flash composition, an impact or any other stimulus can only initiate the thermal mechanism by providing the minimum threshold energy needed/necessary to raise the reaction temperature of 191 ºC as this has been observed experimentally as the onset point for thermal explosion in ARC. Therefore it is possible to relate the mechanical form of energy to the threshold energy (ΔE) observed in the ARC. This provides a means of suggesting a predictive correlation in such explosive systems. The degree of explosivity also depends on the other factors such as chemical components, percentages of those components, compactness, particle size and shape and other environmental conditions.

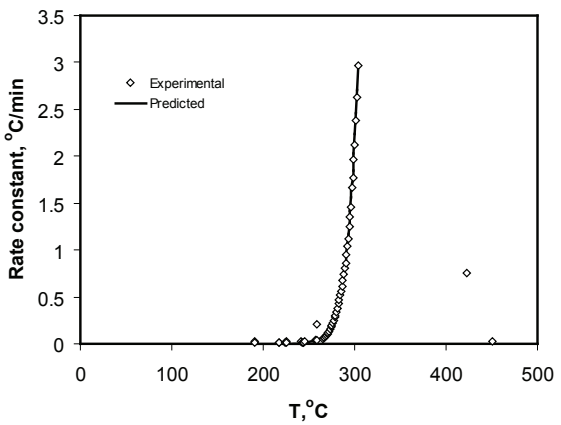

Figure 5 *Kinetic modeling for the adiabatic thermal decomposition of flash composition (KNO_3 : S : Al; 53 : 17 : 30).*

Conclusions

The ARC studies of the flash composition mixture confirm that the mixture is vulnerable to thermal hazard if exposed above 191 ºC. This temperature can be achieved under situations like direct heat radiation from neighboring areas or ignition from unknown sources or through other ignition stimuli like impact or friction. For the first time, a lower onset temperature of 191 ºC for thermal decomposition is recorded in this study. It was shown that the observed onset temperature can be achieved through ignition stimuli like friction or impact. Thus this study can offer a better explanation for the accident triggering mechanism in fireworks factory during the summer months in southern India. The kinetic study reveals that there is good agreement between the experimental and predicted heat rate values. The Arrhenius kinetic constants reported in this study are reliable.

References

1 S. P. Sivaprakasam, M. Surianarayanan, G. S. Venkataratnam and P. Nagaraj, in *Hazard evaluation technique for firework compositions*, Indian Chemical Engineering Congress, Hyderabad, 19–22 December 2003, p. 126.

2 S. P. Sivaprakasam, M. Surianarayanan, G. S. Venkataratnam and P. Nagaraj, "Impact sensitiveness analysis of pyrotechnic flash compositions", *Journal of Pyrotechnics*, No. 21, 2005, p. 52.

3 S. P. Sivaprakasam, M. Surianarayanan, F. Chandrasekran and G. Swaminathan, "Thermal Hazards of Cracker Mixture using DSC", *Journal of Thermal Analysis and Calorimetry*, No. 78, 2004, p. 799.

4 P. D. Lightfoot, R. C. Fouchard, A.-M. Turcotte, Q. S. M. Kwok and D. E. G. Jones, "Thermal Techniques used in the Hazard Evaluation of Pyrotechnics", J*ournal of Pyrotechnics*, No. 14, 2000, p. 15.

5 Y. Iizuka and M. Surianarayanan, "Comprehensive Kinetic Model for Adiabatic Decomposition of Di-tert-butyl Peroxide Using BatchCAD", *Industrial & Engineering Chemistry Research*, Vol. 42, No. 13, 2003, pp. 2987–2995.

6 D. I. Townsend and J. C. Tou, "Thermal hazard evaluation by an Accelerating Rate Calorimetry", *Thermochimica Acta*, Vol. 37, 1980, pp. 1–30.

7 T. C. Hofelich and R. C. Thomas, "The use/misuse of the 100 degree rule in the interpretation of thermal hazard tests", *Proceedings of the International Symposium on Runaway Reactions*, Cambridge, AIChe, CCPS, Ichem, 1989, pp. 74–85.T

8 M. Surianarayanan, G. Vijayaraghavan, G. Swaminathan and P. G. Rao, "Microcalorimetry and its role in thermal hazard quantification", *Current Science*, 80, 2001, No. 6, p. 25.

9 C. M. Badeen, O. S. M. Kwok, Marie C. R. Vachon, R. Turcotte and D. E. G. Jones, *Journal of Thermal Analysis and Calorimetry*, 81, 2005, p. 225.

FIREWORKS – PRINCIPLES AND PRACTICE 4th Edition

Rev R Lancaster MBE

Review by Christopher Pearce
Chairman – British Pyrotechnists Association

The name of Ronald Lancaster has been synonymous with the British Fireworks Industry for the past forty years or so and his firm, Kimbolton Fireworks, has been responsible for many of the major displays staged in the UK since 1980. The fourth edition of *Fireworks – Principles and Practice* is the current, and perhaps final, stage in the evolution of a book that was first published in 1972.

When the first edition made its appearance, there was relatively little in the way of published material in respect of fireworks manufacture (certainly in the UK). The book was therefore seen as a natural successor to classic texts such as Weingart's *Pyrotechnics* (1947). Over the past twenty years or so, there has been an explosion (sic) in the number of publications dealing with both fireworks and pyrotechnics, at both practical and theoretical levels. However, Lancaster's book still has its place and the 4th edition is a further refinement on its predecessor, which appeared in 1998.

Principles and Practice is presented in a traditional format, with twenty-three chapters covering all aspects of fireworks manufacture, technology, history, and display techniques. In common with all three previous editions, there are contributions from other well known individuals – particularly Tom Smith and Darryl Fleming – whose areas of speciality (legislation and display practices respectively) give added weight and authority to the book. Ronald Hall's name no longer appears in the list of contributors, as Ron Lancaster significantly revised the chapter on Rockets in the previous printing.

The fourth edition differs from the third in a few important respects. There has been a general revision and refinement of the text, a significant improvement in the number and quality of diagrams and illustrations, and a fascinating introductory chapter entitled Sixty Years' Love of Fireworks – Diamonds in The Sky. This is the author's personal reflection on a lifetime in fireworks; it is a delightful and evocative piece of work. To say that it is long overdue is rather crass; after all, the right time to pen a worthwhile biography is in your twilight years, with all the benefit of hindsight (although it is not uncommon for modern footballers to record their life history well before arriving at their thirtieth birthday!). Lancaster takes us back to pre-war days in Yorkshire, where his passion for fireworks was kindled, and then develops the chapter by recalling his time with Pains–Wessex before taking the huge step of developing Kimbolton Fireworks as an entity in its own right. In forty pages or so, the reader is given an insight into a little personal, social and industrial history – which is of great value. Chapter 1, The History of Fireworks, by Roy Butler has not changed significantly since the previous edition, but is still an excellent survey of the development of fireworks manufacture. It is supported by some rather nice images of display rigging and factory production relating to Brocks' activities in the 1930s.

Taking *Principles and Practice* as a whole – from the outset, the author's philosophy was to produce a textbook that adopted a 'broad-brush' approach. As a result, all of the key areas involved in general firework manufacture are covered in reasonable depth, without immersing the reader in minute detail. Take the design and construction of cylinder shells, for example. This is covered in just a few pages within chapter 16, whereas one could devote a whole chapter to do justice to this specialised area of shell manufacture. Lancaster covers the basics more than adequately, and refers the reader to more comprehensive works on the subject – a sensible approach that is adopted throughout.

Chapter 8 concerning Mixing and Charging is a nice example of how Lancaster's book has evolved since its first printing in 1972. While the basic content has remained the same, the chapter benefits from improved diagrams (some of which are now 3D), a series of new photographs (the Pains–Wessex images having been replaced by equivalent pictures from the Kimbolton factory), and the author's personal opinions on the current state of play. Lancaster does not pull any punches when it comes to his assessment of contemporary

approaches to health and safety. As an ordained Anglican minister, he is able to draw on a source of 'higher authority' and does so from time to time, with amusing results. Bemoaning the excesses and complexity of modern health and safety management, Lancaster quotes from the Bible - Luke XI verse 46 "Yes, you Lawyers and Pharisees, you load men with intolerable burdens and will not put a single finger to lift the load." Quirky inclusions such as this add a touch of mild eccentricity, at the same time enhancing its appeal as a work of unique style.

The key 'technical' chapters of the book, as with previous editions, cover all fundamental aspects of fireworks manufacture and deal with individual types; rockets, shells, roman candles, fountains and so on. Each chapter is comprehensive enough to provide a good basic grounding in the functional principles, with a strong practical emphasis throughout. The framework of the book has not changed significantly, in this respect, compared with the 3rd edition. Basic firework chemistry is also dealt with in a clear and concise fashion – providing an excellent grounding in the subject, borne out of the author's own experience.

The 4th edition of *Principles and Practice* does contain a number of errors – mainly textual and typographical, many of which appear in the glossary. These do not detract from the overall quality of the publication, but need to be addressed in any future printings. A couple of important 'chemical' errors have also been identified and the author has already produced a list of corrections.

Ron Lancaster has never needed to strive to establish his credentials as an authority in the field of fireworks. His research and development work has won him considerable respect and Kimbolton's achievements in the display forum speak for themselves. *Principles and Practice* has grown alongside Ron Lancaster's reputation; both author and publication have now reached full maturity and the 4th edition of this already 'classic' text will consolidate Lancaster's position as a key figure in the history of fireworks manufacture. This latest version should be in the library of anyone who has a serious interest in the subject – whether that be from a technical or historical perspective, or both!

2nd Workshop on Pyrotechnic Combustion Mechanisms, held July 27th 2005 in Fraunhofer ICT Pfinztal, Germany

Ernst-Christian Koch[a] and Rutger Webb[b]
[a]Diehl BGT Defence GmbH & Co. KG, Fischbachstr. 16, D-90552 Röthenbach a d Pegnitz
[b]TNO, Defence Safety & Security, Rijswijk, The Netherlands

For the second time the "Workshop on Pyrotechnic Combustion Mechanisms" was held at Fraunhofer ICT in Pfinztal, Germany, preceding the combined 32nd IPS and 36th ICT Seminar in Karlsruhe. The Workshop had 41 registered participants from Germany, Poland, UK, USA, Israel, Turkey, Austria, Sweden, Finland and the Netherlands.

This event received positive feedback from both participants and presenters.

The following presentations have already been published elsewhere.

- *M. Eremets, Polymeric Nitrogen,*
- *P. Politzer, Computional Analyses of High-Nitrogen C,H,N Compounds*
- *S. Cudzilo, Formation of Carbon Based nanostructures by Combustion of Reductant-Halocarbon Mixtures*
- *D. Ladouceur, An Overview of the Known Chemical Kinetics and Transport Effects Relevant to Mg/PTFE Combustion*

The Combustion Properties of Novel High-Nitrogen Energetic Materials

David E. Chavez, Michael A. Hiskey, My Hang Huynh, Darren L. Naud, Steven F. Son and Bryce C. Tappan

Los Alamos National Laboratory
High Explosives Science and Technology
DX-2 MS C 920
Los Alamos, NM 87545 USA
naud@lanl.gov and hiskey@lanl.gov

Abstract: *High-nitrogen energetic materials based on the tetrazine and tetrazole ring systems have shown unique and unpredictable combustion behavior. Unlike traditional energetic compounds, such as 2,4,6-trinitrotoluene (TNT) and hexahydro-1,3,5-trinitro-1,3,5-triazine (RDX), which derive their energy by the oxidation of the carbon and hydrogen skeletal atoms by the oxygen carrying nitro group, high-nitrogen materials typically have large positive heats of formation as their source of energy. This difference in the energy source may partly explain why the combustion chemistries of some high-nitrogen materials are unusual.*

Using the precursor 3,6-bis-(3,5-dimethylpyrazol-1-yl)-s-tetrazine (BDT), several useful energetic compounds based on the s-tetrazine system have been synthesized and studied. A number of these tetrazine-based materials have shown to exhibit burn rates with low sensitivity to pressure, namely 3,6-bis(1H-1,2,3,4-tetrazol-5-ylamino)-s-tetrazine (BTATz), 3,6-bis-nitroguanyl-1,2,4,5-tetrazine (NQ_2Tz), the corresponding bis-triaminoguanidinium salt (TAG_2NQ_2Tz) and the N-oxides of 3,3′-azobis(6-amino-1,2,4,5-tetrazine) (DAATO3.5). A fifth compound of high nitrogen make-up, triaminoguanidinium azotetrazolate (TAGzT), is not prepared from BDT, but it also burns at exceptional rates with low pressure sensitivity.

The tetrazole-based materials, bis-(1(2)H-tetrazol-5-yl)-amine (BTA) and 5,5′-bis-1H-tetrazole (BT), are useful high-nitrogen energetic ligands for the preparation of metal complexes. While BTA, BT and their salts have been previously shown as possible energetic fuels for low-smoke pyrotechnic applications, some recent combustion experiments with the metal complexes of BT and BTA have proved to be even more noteworthy. These metal ion complexes have sufficient internal energy that they can burn under an inert atmosphere to produce the free metal, usually in the form of high-surface area foams or nano-sized particles. This highly unusual, reductive combustion chemistry may lead to efficient and controlled production of metal nanofoams.

The heat of formation (ΔH_f) of 3,6-diazido-1,2,4,5-tetrazine (DiAT), a highly energetic and sensitive energetic material (most notably to friction, spark and impact), was calculated to be approximately +1100 kJ mol^{-1}, or +92 kJ mol-$atom^{-1}$, using an additive method. Depending on the heating rate, DiAT can undergo pyrolytic decomposition to produce either carbon nanospheres or carbon nitride nanopolygons. With slow heating, leaf-like or rope-like forms of carbon nitride were the predominant products. With faster heating, carbon spheres with diameters on the order of 10 to 100 nm were produced. Such nanomaterials are of interest to the scientific community for a wide number of industrial applications.

Keywords: *high-nitrogen, tetrazole, tetrazine, combustion, nanomaterials, propellant, foam*

Introduction

At Los Alamos National Laboratory we have developed a number of energetic high-nitrogen materials that exhibit unusual combustion properties with a variety of potential commercial and military applications. These materials have two characteristic attributes. First, they are

high in nitrogen and, consequently, have large positive heats of formation, which is attributed to the nitrogen–nitrogen bonds that are prevalent in these systems.[1] Second, because the skeletal framework contains relatively less carbon and hydrogen when compared to traditional explosives, the oxygen balance can be more easily achieved. Furthermore, these materials possess relatively high crystal densities, a critical parameter for the enhancement of explosive performance, and are often insensitive towards destructive stimuli such as impact, friction, and electrostatic discharge. Of particular interest to our group is the synthesis of high-nitrogen materials based on the tetrazine and the tetrazole systems. In this paper we describe the combustion properties of a number of these materials in three applications, specifically their potential use as high-performance propellant ingredients, precursors for high-surface area and low-density metal foams, and carbon and carbon nitride nanomaterials.

High-Performance Propellant Ingredients

Solid propellants provide a means of converting chemical potential energy into useful kinetic energy. Although the chemical ingredients of propellants are varied and complex, two basic components—fuel and oxidizer—burn to produce heat and gas, which can expand in a gun barrel to push a shell, or flow at supersonic speed in a De Laval nozzle to provide thrust. High-nitrogen compounds may be the key to meeting the advanced performance objectives of next-generation propellants. Classical solid propellants have not changed fundamentally for nearly three decades and can be separated into two general classes. **Monopropellants** contain ingredients that have fuel and oxidizer in the same molecule, such as the explosives octahydro-1,3,5,7-tetranitro-1,3,5,7-tetrazocine (HMX) or nitroglycerine (NG). **Heterogeneous** or **composite propellants** are aggregate mixtures of fuel and oxidizer bound together by polymeric binder, which is a fuel itself. The ammonium perchlorate (AP) and hydroxy-terminated polybutadiene (HTPB) matrix is a popular composite motor propellant system. Ingredients, such as HMX, aluminum or AP of different particle sizes, are often included in the composite matrix to enhance or tailor its performance. A serious drawback of AP solid propellants, however, is the copious amount of toxic hydrogen chloride that is generated as a combustion product. One solid rocket booster of the space shuttle, for example, generates 240,000 pounds (109 tonnes) of hydrogen chloride gas.

High-nitrogen energetic materials offer the possibility of significant performance improvement over current propellant systems in at least two ways. In one, inert and invisible nitrogen gas is the major combustion product of high-nitrogen materials, which is a clear improvement over toxic hydrogen chloride produced by AP composite propellants. This will also facilitate the formulation of low-smoke, "reduced-signature" propellants, a useful feature that increases the defensive posture of an attacker. In the second, high-nitrogen materials typically have large positive heats of formation and generate low molecular weight gases, attributes that are very desirable for high impulse performance. This is best exemplified by the simplified reciprocal relationship between the exit gas velocity, V, of a De Laval nozzle and the mean average of the molecular weights of the combustion gas products, M_{ave}.

$$V \propto [1/M_{ave}]^{1/2}$$

Decreasing the overall molecular weight of the exit gases by substituting hydrogen chloride, carbon monoxide and carbon dioxide, which are typical reaction products of HMX/AP composite motors, with lighter gases of high-nitrogen compounds, such as H_2 and N_2, will increase the exit gas velocity, and in turn the impulse of the motor.

In this section, we compare the burn-rate data of five high-nitrogen energetic materials as viable candidates for use in high-performance propellants. They are: (1) 3,6-bis(1*H*-1,2,3,4-tetrazol-5-ylamino)-*s*-tetrazine (BTATz), (2) the mixed *N*-oxides of 3,3′-azobis(6-amino-1,2,4,5-tetrazine) (DAATO3.5), (3) triaminoguanidinium azotetrazolate (TAGzT), (4) 3,6-bis-nitroguanyl-1,2,4,5-tetrazine (NQ_2Tz), and (5) its corresponding bis-triaminoguanidinium salt (TAG_2NQ_2Tz). The structures of these materials are given in Figure 1. Except for TAGzT, all of the above compounds are derived from the valuable precursor, 3,6-bis(3,5-dimethylpyrazol-1-yl)-1,2,4,5-tetrazine, which is prepared in two steps from commercially available triaminoguanidine hydrochloride,

2,4-pentanedione, and nitrogen dioxide.[2] The synthesis procedures of these five materials have been described elsewhere.[3]

In Figure 2, the measured burn rate *vs*. pressure profiles are graphically represented for the pressure ranges studied for each material.[4] The linear relationship between burn rate (r_b) and pressure (p) is best described by the empirical equation $r_b = cp^n$, where c is the empirical constant and n is the pressure exponent.[5] A large pressure exponent (approaching 1 or greater) is often typical with traditional high explosive materials and indicates that 2nd order gas-phase reactions dominate the combustion process. A lower pressure exponent, however, is attributed to early rate-controlling reactions in the condensed phase, and thus results in a burn rate that is insensitive to changes in pressure. Low pressure sensitivity (*i.e.*, a low pressure exponent) offers advantages in the design of gun and rocket propellants, particularly in motor stability. Conversely, energetic materials with high exponent values are typically avoided for use in propellant applications. In all five materials, the pressure exponents are reasonably, if not exceptionally low (see Table 1). For comparison, the pressure exponent for HMX is 0.75 and its burn rate at 1000 psi is 1.1 cm s^{-1}.[5]

Nanoporous metal foams

The synthesis of low-density, nanoporous materials has been an active area of study in chemistry and materials science dating back to the first synthesis of aerogels.[6] These materials, however, are mostly limited to silica, metal oxides (*e.g.*, Al_2O_3) and organic aerogels (*e.g.*, resorcinol/formaldehyde), with the only elemental material being carbon, arising from the pyrolysis of organic aerogels.

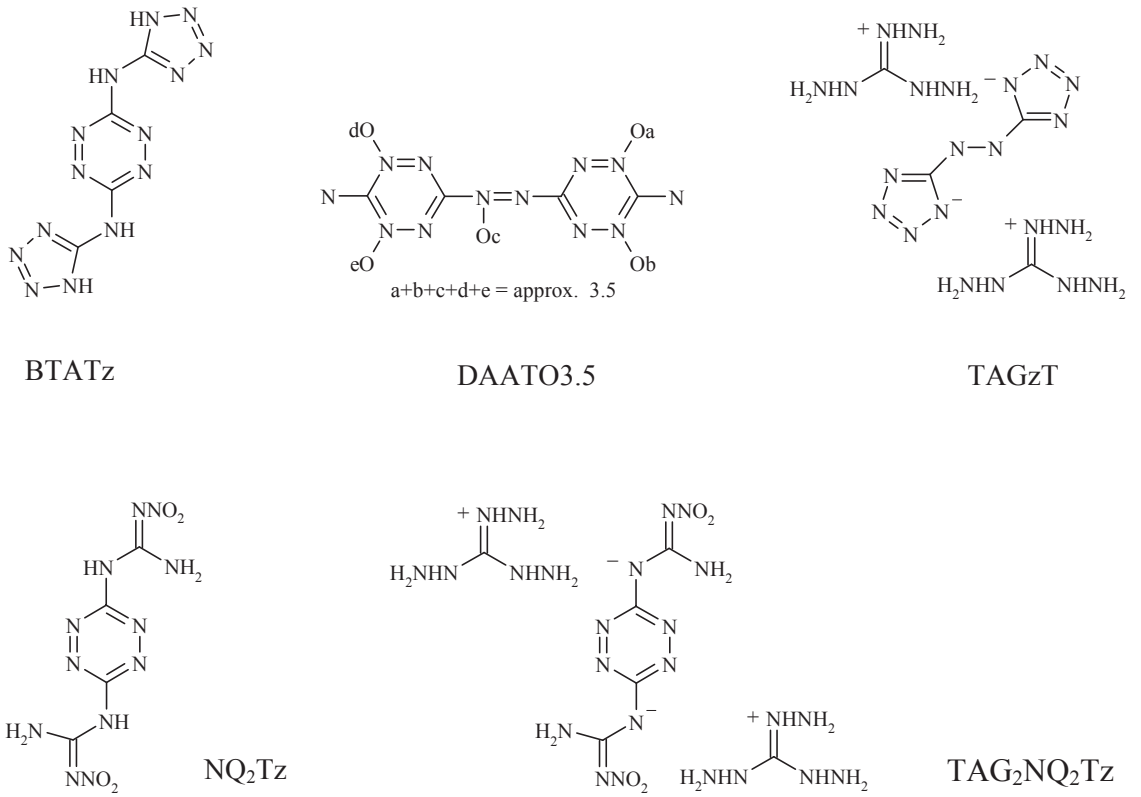

Figure 1 *Five high-nitrogen energetic materials of interest as high-performance propellant additives: (a) 3,6-bis(1H-1,2,3,4-tetrazol-5-ylamino)-s-tetrazine (BTATz); (b) the mixed N-oxides of 3,3′-azobis(6-amino-1,2,4,5-tetrazine) (DAATO3.5); (c) triaminoguanidium azotetrazolate (TAGzT); (d) 3,6-bis-nitroguanyl-1,2,4,5-tetrazine (NQ_2Tz); and (e) its corresponding bis-triaminoguanidinium salt (TAG_2NQ2Tz).*

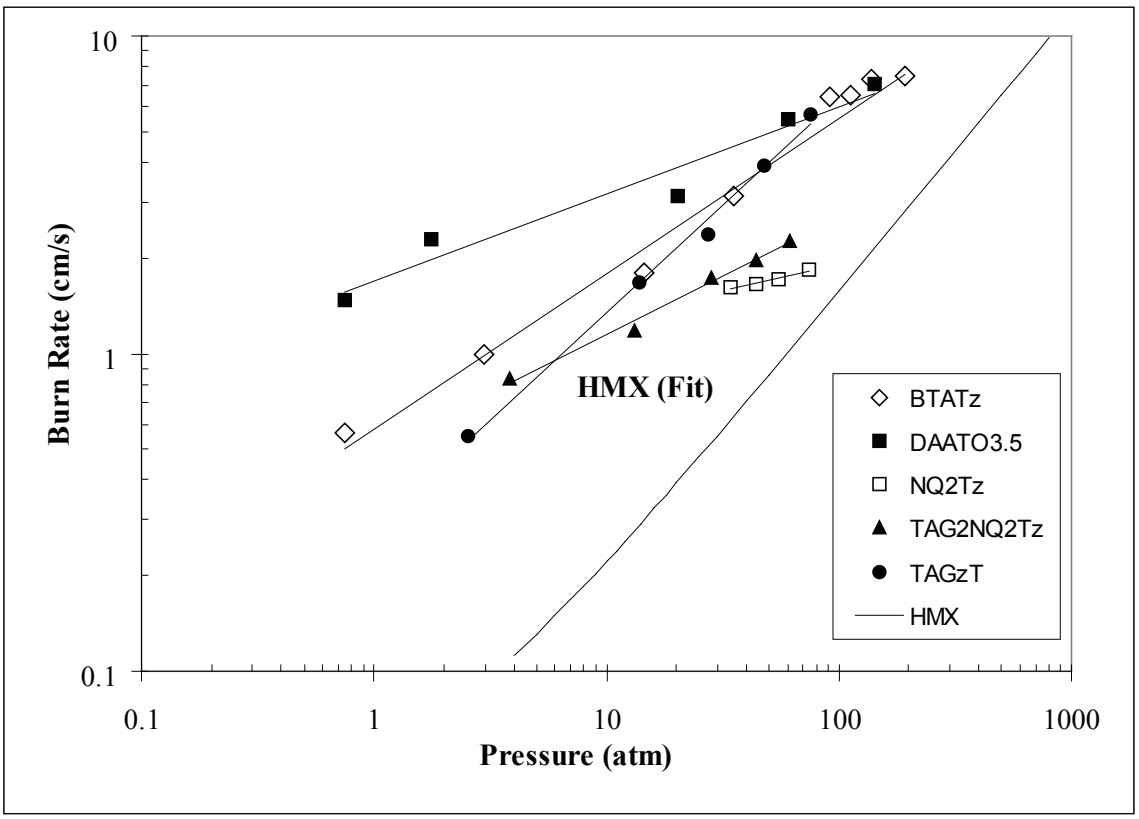

Figure 2 *Burn rate versus pressure profile for five high-nitrogen energetic materials. Some of the materials were pressed with binders (BTATz with 3% Kel-F-800, DAATO3.5 with 5% PVA and 1% TEG), while the rest were studied as neat materials.*

Table 1 *Sensitivity and burn rate data for five high nitrogen materials. All data are for pure material unless noted otherwise.*

	BTATz	DAATO3.5	TAGzT	NQ_2Tz	TAG_2NQ_2Tz
Pressure Exponent, *n*	0.49[a]	0.275[b]	0.67	0.163	0.366
Empirical Constant, *c*	0.581	1.69	0.287	0.899	0.494
Burn Rate at 1000 psi †	4.6	5.4	4.9	2.0	2.3
H_{50} (cm) Type 12	32[c]	50	25	65	114
DSC Onset (°C)	264	177	195	228	166
Friction (kg) BAM	> 36	2-14	10	> 36	> 36
Spark (J)	< 0.36[d]	< 0.36	< 0.31[e]	> 0.36	> 0.36
Density (g cm^{-1})	1.76	1.88	1.60	1.76	1.61
ΔH_f (kJ mol^{-1})	+883	+690	+1075	+389	+1255
ΔH_f (kJ mol-$atom^{-1}$)	+40.1	+29.4	+24.4	+15.0	+22.4

[a]BTATz formulated with 3% Kel-F-800 binder. [b]DAATO3.5 formulated with 5% PVA and 1% TEG. [c]Positive impact results ranged widely between 32 and 200 cm so a conservative value of 32 cm was assigned. [d]11 out of 13 samples initiated when subjected to 0.36 J of energy. [e]Threshold Initiation Limit (TIL) value, which represents a probability that an event will happen 3.4% of the time a given stimulus is applied. † 68.0 atm or 6.89 MPa.

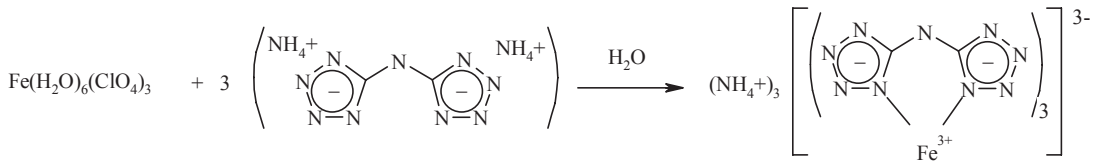

Figure 3 *Synthesis scheme of Fe-BTA, formed by the reaction of iron(III) perchlorate with 3 equivalents of diammonium salt of bis-(1(2)H-tetrazol-5-yl)-amine (BTA).*

A method to prepare ultra-low-density transition-metal foams has been developed using a novel pyrotechnic technique. The process is simple in concept; a transition-metal complex containing an energetic, high-nitrogen ligand is allowed to combust under an inert atmosphere, such as argon or nitrogen. As the complex burns, the metal cation undergoes chemical reduction to the free metal. Because the intrinsic energy of the selected complex is high, the combustion is self-sustaining. By this method, metal monolithic foams with remarkably low densities (0.011 g cm^{-3}) and high surface areas (258 m^2 g^{-1}) have been formed. The ability to form monolithic metallic nanocellular

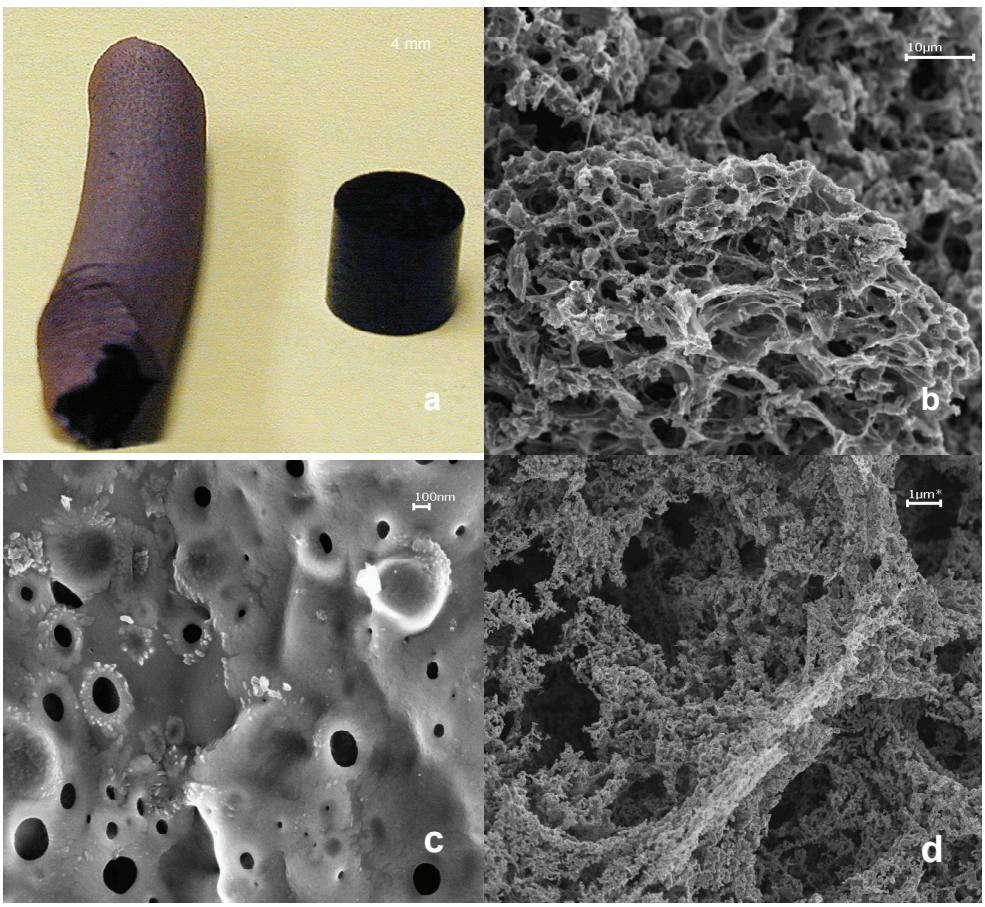

Figure 4 *(a) Photograph, 4 mm scale, of iron foam next to unburned pellet of the Fe-BTA complex. (b) Scanning electron micrograph (SEM), 10 µm scale, of low pressure iron foam showing pore structure of roughly 1 µm. (c) SEM, 100 nm scale, of high pressure iron foam showing pore sub-structure of roughly 20–100 nm. (d) SEM, 1 µm scale, of heat-treated iron foam.*

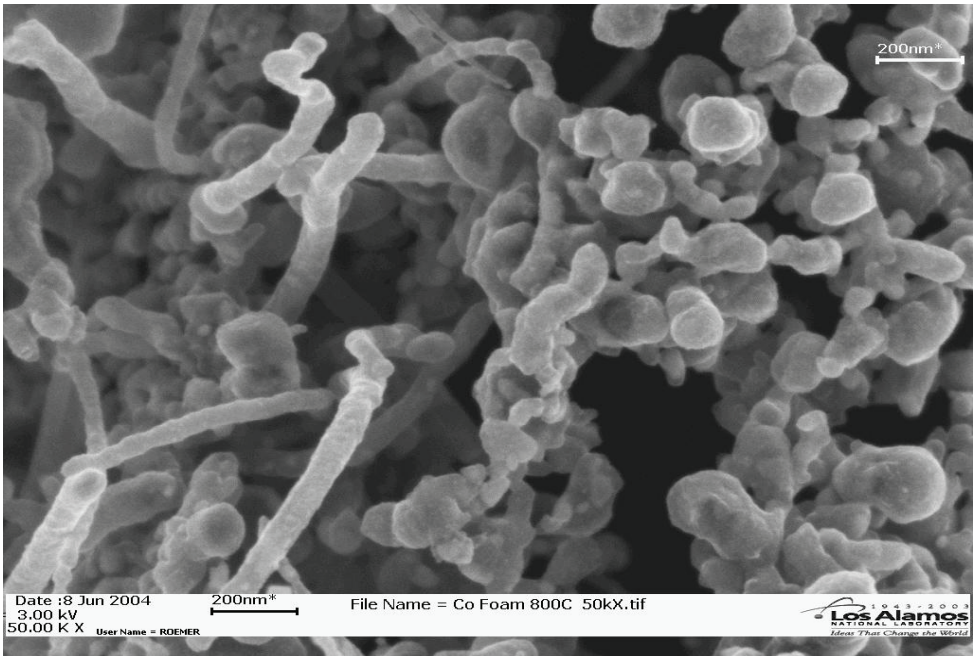

Figure 5 SEM, scale 200 nm, of Co foam after heat treatment, foam walls made up of particles and rods of cobalt metal.

porous materials is presently not possible using conventional processes, particularly at the densities we have observed or with such ease of production. To date, we have produced iron, cobalt, copper and silver foams from their corresponding high-nitrogen ligand complexes.

The lowest-density metal foams found in the literature range from 0.04-0.08 g cm^{-3} and were made from magnesium and aluminum. These foams, however, contain cells on the millimetre length-scale, and have a relatively low surface area.[7] Recently, a silver sponge was reported with pore sizes on the order of a few microns and a surface area of 0.5 m^2 g^{-1}, however, no density was given.[8] The synthesis of dendritic platinum with three-dimensional foam-like nanostructures

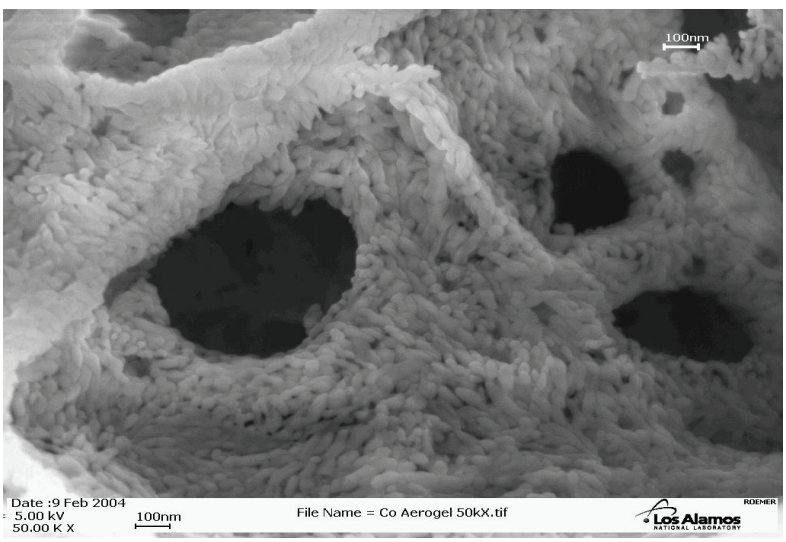

Figure 6 *SEM, scale 100 nm, of Co foam showing nanoporous substructure made up of rice-like particles that form foam walls.*

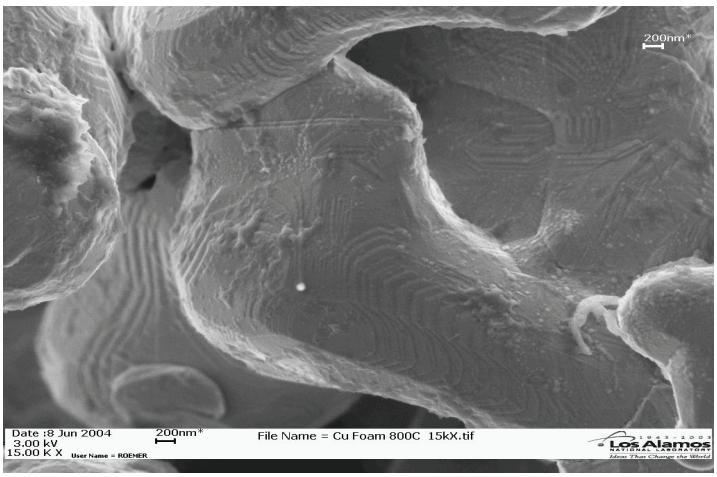

Figure 7 *SEM, 200 nm scale, of heat-treated copper foam.*

was also recently described, but the structures are limited to small clusters ranging in size from 6 to 200 nm.[9]

The first and best characterized metal foam in our initial studies was obtained from the ammonium tris(bi(tetrazolato)amine)ferrate(III) complex (Fe-BTA). This complex is easily formed by the reaction of 3 : 1 molar ratio of the diammonium salt of bis-(1(2)*H*-tetrazol-5-yl)-amine (BTA) and iron(III) perchlorate (Figure 3). BTA is a high-nitrogen material easily synthesized from inexpensive sodium dicyanamide and sodium azide under controlled addition of hydrochloric acid.[10] When ignited as a loose powder in air, Fe-BTA rapidly combusts with the production of orange sparks, which is attributed to nascent, elemental iron burning. The combustion of cylindrical pellets of Fe-BTA in a combustion chamber of inert atmosphere at varying pressures results in the formation of the metal foam monolith

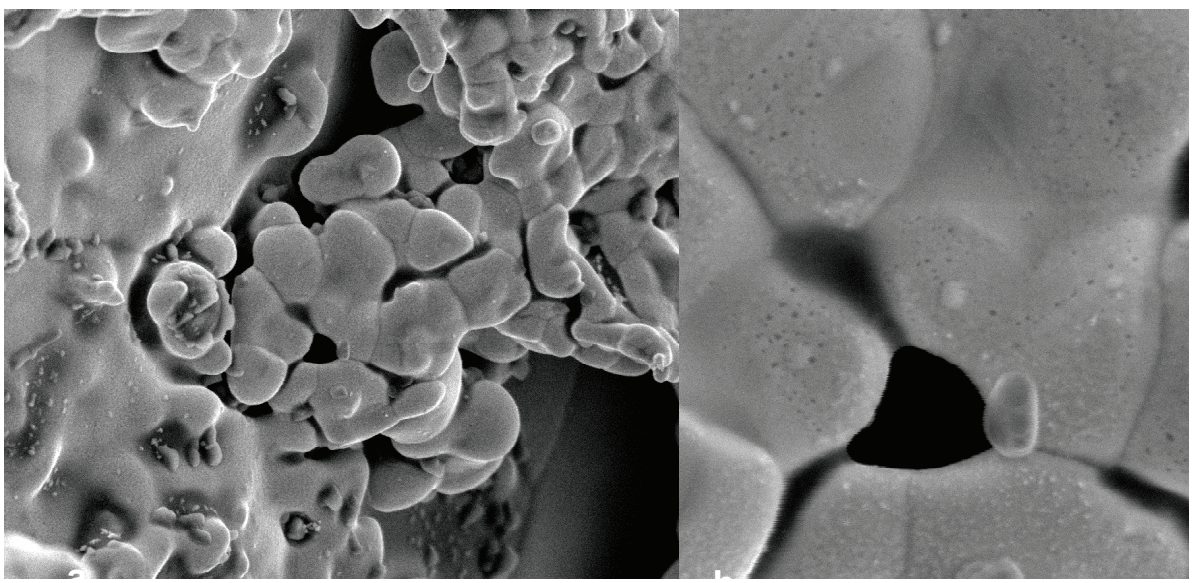

Figure 8 *(a) SEM, scale 1 μm, of Ag foam. (b) scale 100 nm, closer view of (a) showing surface nano-porosity of around 20 nm.*

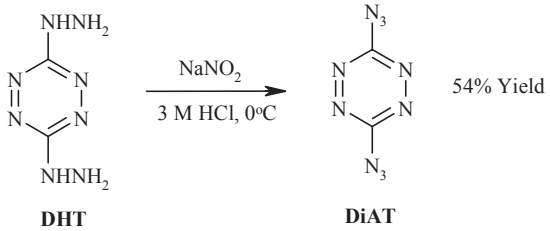

Figure 9 *Synthesis scheme for DiAT from 3,6-dihydrazino-1,2,4,5-tetrazine (DHT).*

(Figure 4a). Following combustion at 20.4 atm, a bimodal pore size distribution was observed within the micron and 20–200 nm ranges. Interestingly, combustion at higher pressure (72.3 atm) resulted in a metallic foam containing only the 20–200 nm pore size distribution (Figures 4b–c). Brunauer–Emmett–Teller (BET) surface area analysis for the metal foam produced at 20.4 atm yielded an extraordinarily high surface area of 258 $m\,g^{-1}$. For comparison, a high surface area titania aerogel has BET values that range from 100 to 200 $m\,g^{-1}$.[11] BET surface areas for foams produced at higher pressures (*ca*. 70 atm) range from 12 to 17 $m\,g^{-1}$. Evidently, the high-nitrogen ligand acted as a blowing agent on a molecular level as Fe-BTA decomposed, liberating decomposition gases. Elemental analysis (standard combustion technique) and energy dispersive spectra (EDS) demonstrated that the as-produced metal foams contain up to 50% carbon and nitrogen which are mostly removed by heating to 1073 K in an inert atmosphere (Figure 4d). While no density or surface area measurements were made on the heat-treated foam due to small sample size, it is apparent from the SEM image that no sintering took place (Figures 4d and 5). Thermogravimetric analysis (TGA) and EDS indicate that the heat-treated foams range from 10% remaining carbon (iron foam) to essentially pure (copper foam).

Metal foam production using this unique combustion method is possible with other transition metal complexes. Cobalt, silver and copper metal foams have been produced from the corresponding BTA complexes; however, the morphology of the resultant foam is strongly dependent on the metal employed. Electron micrographs of the cobalt foam showed the two basic pore morphologies observed in the iron foam. A third morphology consisting of small cobalt grains (*ca*. 100 nm) that aggregate to form the foam walls, which should dramatically increase the surface area of the metal foam (Figure 6). The copper foam was of a higher density and had much more regular, yet larger pore sizes of approximately 1 micron, and after heating to remove impurities, displayed interesting crystal lattice lines along the foam walls (Figure 7). The silver foam was the most dense, and in fact had partially fused to form shiny silver beads. Selected SEM images of the silver foam that had not fused show a foam structure, indicating that monoliths similar to those of iron foam could perhaps be achieved by optimizing the combustion method (Figures 8a–b). This pyrotechnic method shows promise as a flexible and simple approach to the formation of a wide range of new nanoporous metals that are not currently accessible by state-of-

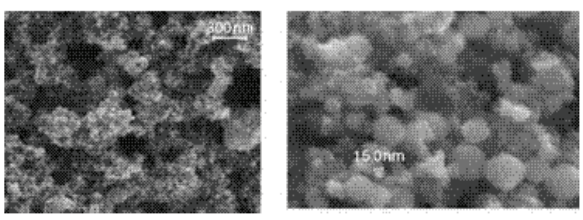

Figure 10 *SEM images of carbon nanospheres at magnifications of 25,000 × (left) and 150,000 × (right).*

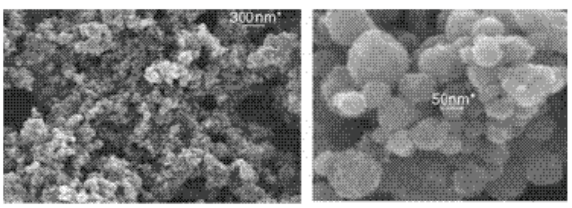

Figure 11 *SEM images of carbon nanopolygons at magnifications of 25,000 × (left) and 150,000 × (right).*

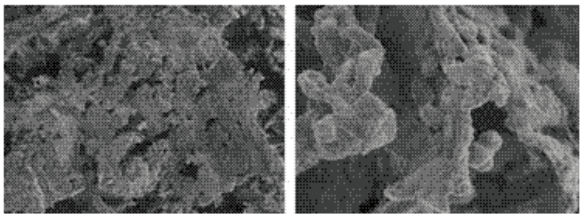

Figure 12 *SEM images of carbon nitride, C_3N_4, with leaf-like (left) and rope-like (right) morphologies.*

the-art nanoscience. Possible applications abound in the fields of catalysis, fuel cells, hydrogen storage, unique insulation, and electromagnetic absorption materials.

Pyrolysis of 3,6-diazido-*s*-tetrazine (DiAT)

The compound, 3,6-diazido-1,2,4,5-tetrazine (DiAT), is easily prepared by the diazotization of 3,6-dihydrazino-1,2,4,5-tetrazine (DHT) (Figure 9). *Typical of organic azides, DiAT is extremely sensitive to spark, friction and impact stimuli and must be handled with extreme care and in small quantities, preferably stored as a solution*.[12] Using the additive method, the heat of formation of DiAT was estimated to be relatively high, approximately +1100 kJ mol^{-1}, or +92 kJ $mol\text{-}atom^{-1}$.[13] The large positive value is attributed to its high nitrogen makeup of 85.4% by weight. Because of these attributes, DiAT was examined as a precursor for the production of carbon and carbon nitride nanomaterials by pyrolytic methods.

Elemental carbon is used in many applications, including high-density and high-strength carbon artifacts, super-active carbon beads of high surface area, lithium storage, lithium battery anodes,

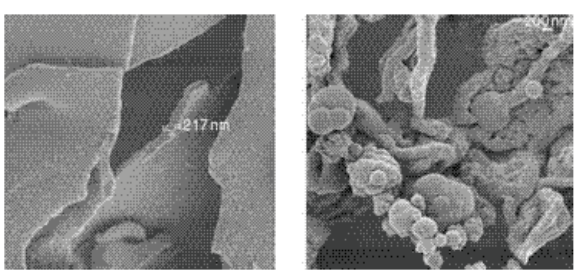

Figure 13 *SEM images of higher-nitrogen content carbon nitride, C_3N_5, with sheet-like (left) and rope and ball (right) morphologies.*

spherical packing materials for HPLC, hydrogen storage applications, and catalysis.[14] Because their applications significantly depend on the shape and size of the particles, much attention is focused on methods of preparation and characterization.

Besides carbon, carbon nitrides are also of interest to the materials community due to their novel mechanical, optical, and tribological properties, including low density, extreme hardness, surface roughness, wear resistance, chemical inertness, and biocompatibility. These mechanically hard materials promise a variety of technological and biological applications. For example, they are used as biocompatible coatings on biomedical implants, battery electrodes, catalytic supports, gas separation systems, electronic materials, and humidity and gas sensors.[15] Applications of carbon nitrides are not only governed by the texture and size of the particles but also by the relative nitrogen content. As a consequence, extensive effort is focused on the discovery of precursors along with the appropriate methods to increase the nitrogen content in carbon nitrides.

Carbon nanoparticles were prepared by the pyrolytic decomposition of DiAT under atmospheric air. The reactions were carried out in a 50 mL heavy-walled pressure bomb. For ease and safety of handling fairly large quantities of DiAT, a method of loading the pressure bomb was developed. A chloroform solution containing 0.2 g of DiAT was poured into the bottom half of the bomb and the solvent allowed to evaporate in the hood. The bomb was assembled and then ramp-heated at a constant rate for 2 hours until the temperature reached 150 ºC. The bomb was cooled and disassembled and the resulting fine product collected from the walls. Elemental and SEM analysis confirmed the production of carbon nanospheres with diameters ranging from 25 to 100 nm (Figure 10). When the reaction was repeated, but with the heating accelerated such that 150 ºC was reached within 1 hour, an audible pop within the pressure bomb was heard. Elemental analysis indicated that the resulting pyrolytic product was again mainly carbon. An SEM image revealed carbon nanospheres with larger diameters, ranging from 50 to 200 nm in diameter (Figure 11).

Nitrogen-rich carbon nitrides were produced

from DiAT when two different heating protocols were employed. Using the same pressure bomb and under ambient air pressure, DiAT (0.3 g) was heated to 100 ºC over the course of 2 h and held at this temperature for an additional 4 h. The temperature was then increased to 150 ºC over 3 h and maintained overnight to yield leaf-like carbon nitride C_3N_4 (Figure 12, left). When DiAT was heated to 150 ºC over the course of 5 h and then held at that temperature overnight, carbon nitride C_3N_4 with a rope and ball morphology was obtained (Figure 12, right). The carbon nitride products from both reactions were confirmed by IR spectroscopy and elemental analysis. Carbon nitrides with higher nitrogen content were formed when the same two heating protocols as describe above were used but conducted under a nitrogen atmosphere. As measured by elemental analysis, the nitrogen content of the reaction products increased from C_3N_4 to C_3N_5. The SEM images of these nitrides show sheet-like (Figure 13, left) and rope and ball morphologies (Figure 13, right).

These results demonstrate a novel method of producing carbon nanospheres with diameters ranging from 5 to 50 nm and nitrogen-rich carbon nitrides of varying morphologies. While DiAT may be one possible precursor, other high-nitrogen compounds with high positive heats of formation may provide additional avenues for the synthesis of exotic carbon and carbon nitride nanomaterials.

Acknowledgements

This work was supported by the Los Alamos National Laboratory Directed Research and Development (LDRD) Program Office in addition to the joint Department of Defense and Department of Energy Munitions Technology Development Program. The Los Alamos National Laboratory is operated by the University of California for the Department of Energy under Contract W-7405-ENG-36.

References

1 For an overview of heats of formation of high-nitrogen materials see: D. E. Chavez, M. A. Hiskey and D. L. Naud, High-Nitrogen Fuels for Low-Smoke Pyrotechnics, *Journal of Pyrotechnics*, no. 10, 1999, pp. 17–36.

2 M. D. Coburn, G. A. Buntain, B. W. Harris, M. A. Hiskey, K. -Y. Lee and D. G. Ott, An Improved Synthesis of 3,6-Diamino-1,2,4,5-tetrazine. II. From Triaminoguanidine and 2,4-pentanedione, *Journal of Heterocyclic Chemistry*, vol. 28, 1991, p. 2049.

3 (BTATz and DAATO3.5) D. E. Chavez, M. A. Hiskey and D. L. Naud, Tetrazine Explosives, *Propellants, Explosives, Pyrotechnics*, vol. 29, 2004, p. 209; (TAGzT) M. A. Hiskey, N. Goldman and J. R. Stine, *Journal of Energetic Materials*, vol. 16, 1998, p. 119; (NQ_2Tz and TaG_2NQ_2Tz) D. E. Chavez, M. A. Hiskey and R. D. Gilardi, Novel High-Nitrogen Materials Based On Nitroguanyl-Substituted Tetrazines, *Organic Letters*, vol. 6, 2004, p. 2899.

4 (BTATz and DAATO3.5) A. N. Ali, S. F. Son, M. A. Hiskey and D. L. Naud, Novel High Nitrogen Propellant Use in Solid Fuel Micropropulsion, *Journal of Propulsion and Power*, vol. 20, 2004, p. 120; (TAGzT) B. C. Tappan, A. N. Ali, T. B. Brill and S. F. Son, Decomposition and Ignition of the High-Nitrogen Compound Triaminoguanidinium Azotetrazolate (TAGzT), *Propellants, Explosives, Pyrotechnics*, accepted for publication; (NQ_2Tz and TaG_2NQ_2Tz) D. E. Chavez, B. C. Tappan, M. A. Hiskey, S. F. Son, H. Harry, D. Montoya and S. Hagelberg, New High-Nitrogen Materials Based on Nitroguanyl-Tetrazines: Explosive Properties and Thermal Decomposition and Combustion Studies, *Propellants, Explosives, Pyrotechnics*, vol. 30, 2005, p. 412.

5 (a) A. I. Atwood, T. L. Boggs, P. O. Curran, T.P. Parr, D. M. Hanson-Parr and J. Wiknich, Burning Rate of Solid Propellant Ingredients, Part 1: Pressure and Initial Temperature Effects, *Journal of Propulsion and Power*, vol. 15, 1999, p. 740; (b) M. J. Ward, S. F. Son and M. Q. Brewster, Steady Deflagration of HMX With Simple Kinetics: A Gas Phase Chain Reaction Model, *Combustion and Flame*, vol. 114, 1998, p. 556.

6 (a) S. S. Kistler, *Nature*, vol. 127, 1931, p. 741; (b) S. S. Kistler, *Journal of Physical Chemistry*, vol. 36, 1932, p. 52.

7 (a) L. Gibson, *Annual Review of Materials Science*, vol. 30, 2000, p. 191; (b) H. Kanahashi, T. Mukai, Y. Yamada,

K. Shimojima, M. Mabuchi, T. G. Nieh and K. Higashi, *Materials Science and Engineering: A*, vol. 280, 2000, p. 349.

8 D. Walsh, L. Arcelli, I. Toshiyuki, J. Tanaka and S. Mann, *Nature Materials*, vol. 2, 2003, p. 386.

9 Y. Song, Y. Yang, C. J. Medforth, E. Pereira, A. K. Singh, H. Xu, Y. Jiang, C. J. Brinker, F. van Swol and J. A. Shelnutt, *Journal of the American Chemical Society*, vol. 126, 2004, p. 635.

10 D. L. Naud and M. A. Hiskey, "Preparation of Bis(1(2)H-tetrazol-5-yl)-amine Monohydrate," *US Patent*, 6,570,022, May 27, 2003.

11 D. J. Suh and T. J. Park, *Chemistry of Materials*, vol. 8, 1996, p. 509.

12 M. H. V. Huynh, M. A. Hiskey, J. G. Archuleta, E. L. Roemer and R. D. Gilardi, *Angewandte Chemie, International Edition*, vol. 43, 2004, p. 5658.

13 M. H. V. Huynh, M. A. Hiskey, D. E. Chavez and R. D. Gilardi, "Synthesis, Characterization and Energetic Properties of Diazido Heteroaromatic High-Nitrogen C-N Compound," submitted for publication.

14 (a) M. Inagaki, Y. Tamai, S. Naka and K. Kamiya, *Carbon*, vol. 12, 1974, pp. 639–643; (b) Y. Yamada, T. Imamura, H. Kakiyama, H. Honda, S. Oi and K. Fukuda, *Carbon*, vol. 12, 1974, pp. 307–319; (c) T. Nitta, M. Nozawa and S. Kida, *Journal of Chemical Engineering of Japan*, vol. 25, 1992, pp. 176–182; (d) J. Economy, L. Dominguez and C. L. Mangun, *Industrial and Engineering Chemistry Research*, vol. 41, 2002, pp. 6436–6442; (e) X. Huang, H. Li, Q. Wang, W. Liu, L. Shi, L. Chen, *Wuli*, vol. 31, 2002, pp. 444–449; (f) A. Mabuchi, K. Tokumitsu, H. Fujimoto and T. Kasuh, *Journal of the Electrochemical Society*, vol. 142, 1995, pp. 1041–1046; (g) H.-Y. Lee and S.-M. Lee, *Electrochemistry Communications*, vol. 6, 2004, pp. 465–469; (h) S. Dasgupta, R. Bhola, R. Jacobs and K. James, *US Patent*, 6261722, 2001; (i) H. Honda, *Molecular Crystals and Liquid Crystals*, vol. 94, 1983, pp. 97–108; (j) T. Yokono, M. Nakahara, K. Makino and Y. Sanada, *Journal of Materials Science Letters*, vol. 7, 1988, pp. 864–866; (k) S. Isobe, T. Ichikawa, J. I. Gottwald, E. Gomibuchi and H. Fujii, *Journal of Physics and Chemistry of Solids*, vol. 65, 2004, pp. 535–539; (l) Z. C. Kang and Z. L. Wang, *Journal of Physical Chemistry,* vol. 100, 1996, pp. 5163–5165; (m) H. Shioyama, *Carbon*, vol. 41, 2003, pp. 2882–2884.

15 a) E. K. Wilson, *Chemical & Engineering News*, vol. 82, 2004, pp. 34–35, and references therein; (b) F. Z. Cui, D. J. Li, *Surface and Coatings Technology*, vol. 131, 2000, pp. 481–487, and references therein; (c) D. J. Li and L. F. Niu, *Bulletin of Materials Science*, vol. 26, 2003, pp. 371–375; (d) D. J. Li, S. J. Zhang and L. F. Niu, *Applied Surface Science*, vol. 180, 2001, pp. 270–279; (e) D. Y. Zhong, G. Y. Zhang, S. Liu, E. G. Wang, Q. Wang, H. Li and X. J. Huang, *Applied Physics Letters*, vol. 79, 2001, pp. 3500–3502; (f) M. Kawaguchi, *Advanced Materials*, vol. 9, 1997, pp. 615–625; (g) H. L. Chang, C. M. Hsu and C. T. Kuo, *Applied Physics Letters*, vol. 80, 2002, pp. 4638–4640; (h) J. N. Armor in *Materials Chemistry, An Emerging Discipline*, Eds. L. V. Interrante, L. A. Caspar and A. B. Ellis, *Advances in Chemistry* Series, American Chemical Society, Washington, DC, 1995, Ch. 13, p. 245; (i) I. Widlow and Y. W. Chung, *Brazilian Journal of Physics*, vol. 30, 2000, pp. 490–498; (j) W. Kulisch, C. Popov and L. Zambov, *New Diamond and Frontier Carbon Technology*, vol. 11, 2001, pp. 53–76.

Laser-initiated Reactions Of Energetic/Thermitic Composites

Jared C. Gump and Suhithi M. Peiris

Indian Head Division, Naval Surface Warfare Center
101 Strauss Avenue
Indian Head, MD 20640 USA

Abstract: *Researchers are attempting to prepare smaller (nano-scale) metal particles, and nano-scale thermitic (metal–metal-oxide) composites. When added to energetic compositions, these nano-materials could burn during or close behind the shock front produced by an explosive material. Therefore, investigation of their combustion kinetics is important, especially when the investigation technique requires only very small quantities of material that is initially prepared. This study uses time-resolved emission spectroscopy to measure reaction kinetics and mechanisms of micrograms of material initiated by a laser pulse. Results from nano-scale aluminum and the thermite-type compositions of Al+Fe_2O_3, Al+MoO_3, and Al+B_2O_3 are presented here.*

Keywords: *laser, nano-scale, composite, kinetics, time-resolved spectroscopy*

Introduction

Metals such as aluminum have been added to energetic material compositions for a long time. Traditionally the Al particles have been in the 20–100 micrometre range, resulting in Al burning after (or behind) the shock front produced by the energetic material. More recently, researchers have been attempting to prepare smaller (nano-scale) metal particles, and nano-scale thermitic (metal–metal-oxide) composites. These nano-materials could burn during or close behind the shock front produced by an explosive material.[1–4] It is important to develop a simple method to measure reaction kinetics using the initially prepared small quantities of these new materials. We use time-resolved emission spectroscopy to measure reaction kinetics of microgram quantities of sample. In this paper we present time-resolved reaction data from nano-scale aluminum and the nano-aluminum containing thermite-type compositions of Al+Fe_2O_3, Al+MoO_3, and Al+B_2O_3, and discuss the kinetic rates of these reactive materials.

Experimental Method

Sample holders were prepared by exposing 5 μm gold foil to focused 532 nm laser light from a 5 ns pulsed ND:YAG laser. The resulting holes were on the order of 80–120 μm in diameter. Powdered samples were pressed onto the gold foil hole using a pestle. Average sample thickness was estimated at 15 μm.

Mounted samples were returned to the focus position of the 532 nm laser and exposed to a single 5 ns pulse. Emitted light was collected and sent by a fiber optic cable first into a spectrometer to disperse the light spatially, then into a streak camera to temporally separate the spectra, and finally into a CCD to measure the intensity of the light at each time and wavelength. The spectrometer was centered at 490 nm and has a spatial range of ~100 nm. The streak camera was set for a 47 μs window. The zero for the time axis was determined by the image of the laser pulse on the streak camera output. Laser pulse energy was estimated from a portion of the beam that was diverted into an energy meter using a single glass slide. For these experiments the average energy per pulse was ~220 mJ.

Experimental results

Nano Al

The energetic/thermitic composites in this study all use nanometre size Al as their fuel. Therefore, it is important to understand what response should be expected from the laser initiation of nano Al by itself. 120.5 nm Al was obtained from Technanogy. This Al had a 4.9 nm thick oxide coating (74.3% active Al content).

During all the laser initiation experiments we performed, an intense, broad background appears in the first couple of microseconds due to the laser interaction with surrounding air. This background reduces after the first couple of microseconds. In the case of nano Al initiation, evidence for AlO emission can be seen above the background noise as early as the first microsecond. By the third microsecond the background has reduced and the dominant features in the spectrum are due to AlO emission. These results are illustrated in Figure 1. Note that due to edge effects on the detector, peaks below about 465 nm in this wavelength window are significantly less intense relative to the rest of the spectrum. The AlO signal that appears by 3 μs persists until 37 μs. Beyond that time, any peak intensity has reduced to the level of the background noise. In Figure 1 each line plot was obtained by averaging over spectra within the time range shown in the legend. The stick plot refers to emission lines obtained from spectrographic references.[5,6] The region from approximately 520–540 nm is reduced in intensity due to a 532 notch filter placed in the beam path to reduce the intensity of the exciting laser, which defines time $t = 0$.

Al + Fe_2O_3

A representative set of spectra for an Al + Fe_2O_3 sample prepared by Professor Edward Dreizin (New Jersey Institute of Technology) is shown in Figure 2.[7] The first peaks attributed to the Al + Fe_2O_3 sample appear above the background even during the first or second microsecond. A full set of peaks is clearly visible beginning from 4 μs, and the average of the spectra from 4 to 8 μs is shown. The majority of peaks appearing in this spectrum can be attributed to elemental iron. These results illustrate that the iron oxide is breaking apart very early in the reaction. Some iron lines persist through 30 μs, but any evidence of them beyond 38 μs is lost in the background noise.

By 30 μs there is some evidence for the appearance of AlO peaks. The maximum intensity for these peaks occurs during 30 to 34 μs. A time average over this interval is shown in Figure 2. As can be seen, the AlO peaks are not well-formed. This may be due in part to overlap with the iron lines that are still in the spectrum.

An Al + Fe_2O_3 sample was also obtained from Professor Michael Zachariah's group (University of Maryland).[8] This sample also exhibited Fe peaks within the first couple of microseconds after exposure. However, by the 9 μs peaks from AlO emissions become visible and are more intense than the Fe peaks. The strongest Fe peaks persist

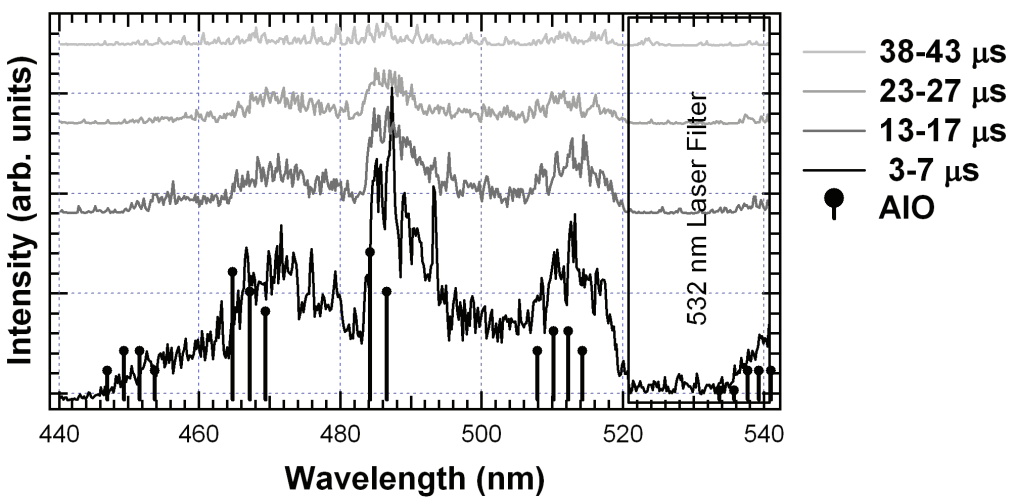

Figure 1 *Time resolved emission spectra from the laser initiation of 120.5 nm Al. The line plots were obtained by averaging the spectra within the time ranges shown in the legend. The stick plot was generated from emission lines for AlO obtained from a spectrographic reference.*

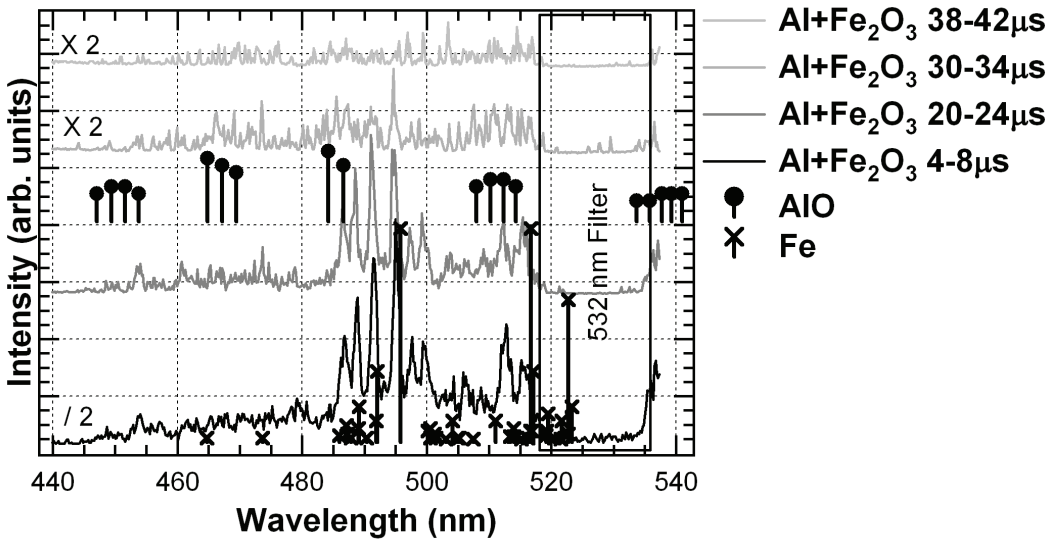

Figure 2 *Representative spectra for reaction of Dreizin's Al + Fe_2O_3. Each Al + Fe_2O_3 line spectrum is an average over the time range shown.*

for at least 20 μs. The AlO peaks are visible until 35 μs. Beyond 35 μs there are no spectral features distinguishable above the background noise. Time-averaged spectra from the reaction of Zachariah's Al + Fe_2O_3 sample can be seen in Figure 3.

Al + MoO_3

Figure 4 displays a representative set of spectra for the reaction of Al + MoO_3 (also prepared by Dreizin's group). During the first 8 μs of the reaction there is evidence of elemental Mo above the background. This is illustrated by the average of the spectra from 2 to 7 μs shown in Figure 4.

By 9 μs, weak AlO peaks begin to emerge. These peaks gain in intensity, reaching a maximum around 22 μs. The time average of the spectra from 20 to 24 μs is shown in Figure 4. By 40 μs there is still some evidence for AlO peaks, but their intensities are barely above the background noise.

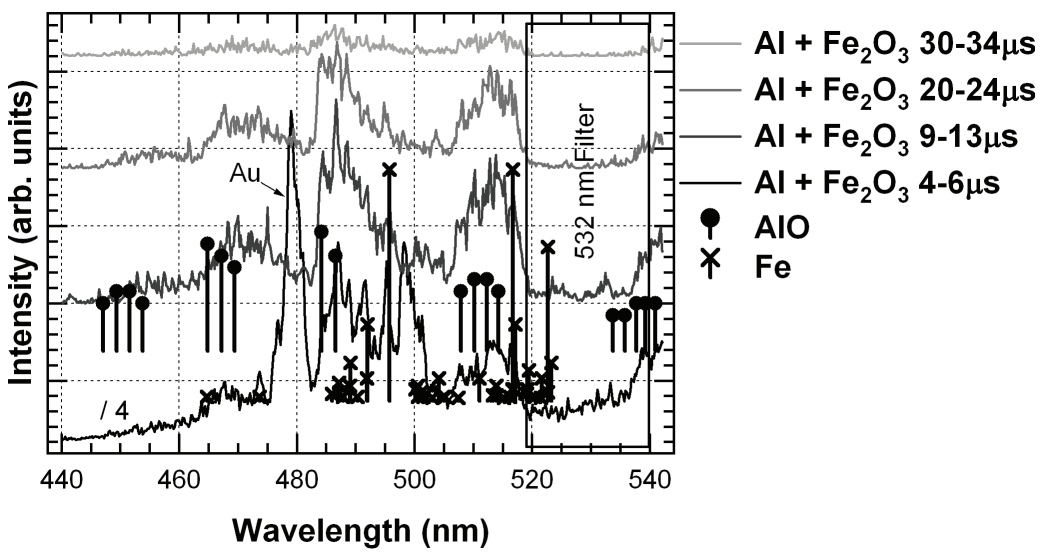

Figure 3 *Representative spectra for reaction of Zachariah's Al + Fe_2O_3. Each Al + Fe_2O_3 line spectrum is an average over the time range shown.*

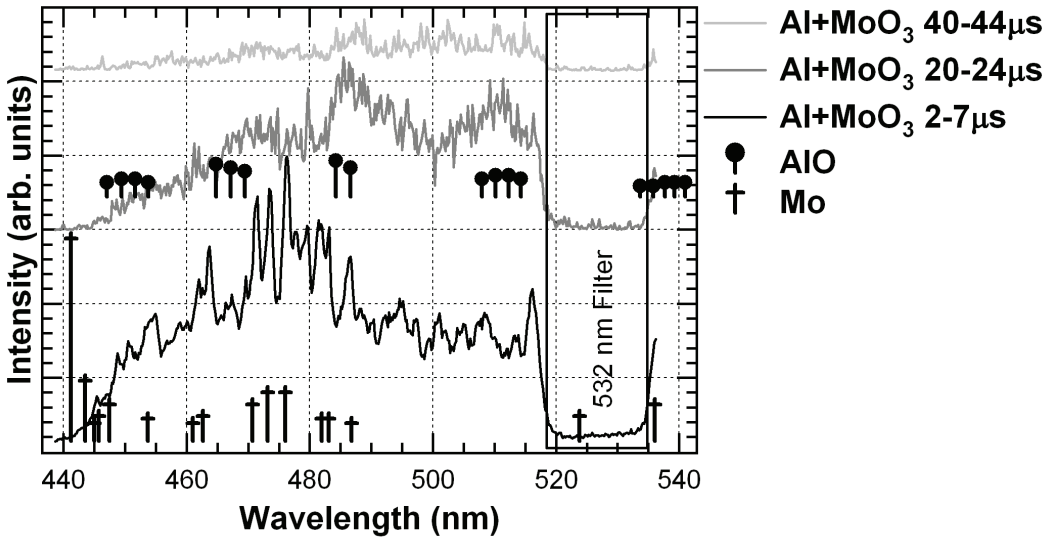

Figure 4 *Representative spectra for reaction of Dreizin's Al + MoO_3. Each Al + MoO_3 line spectrum is an average over the time range shown.*

Al + B_2O_3

Al + B_2O_3 samples were prepared at the South Dakota School of Mines by Jan Puszynski's group.[9] The laser initiation of Al + B_2O_3 produces a more complicated set of spectra with time. For the previous samples, the dominant spectral features visible in this wavelength regime could be attributed to one species or two species that were reasonably well separated in either time or wavelength. In the case of Al + B_2O_3 it is possible that three species are emitting within the same time window. As can be seen in Figure 5, during the first 8 μs there is evidence for AlO emission, but there are other peaks unaccounted for by AlO. In fact, by the 9–13 μs range, the AlO peaks become less intense relative to the rest of the spectrum. The most plausible candidates for the extra spectral features seem to be the oxides of boron. During the 4–8 μs time range evidence for BO is apparent. There is also evidence for

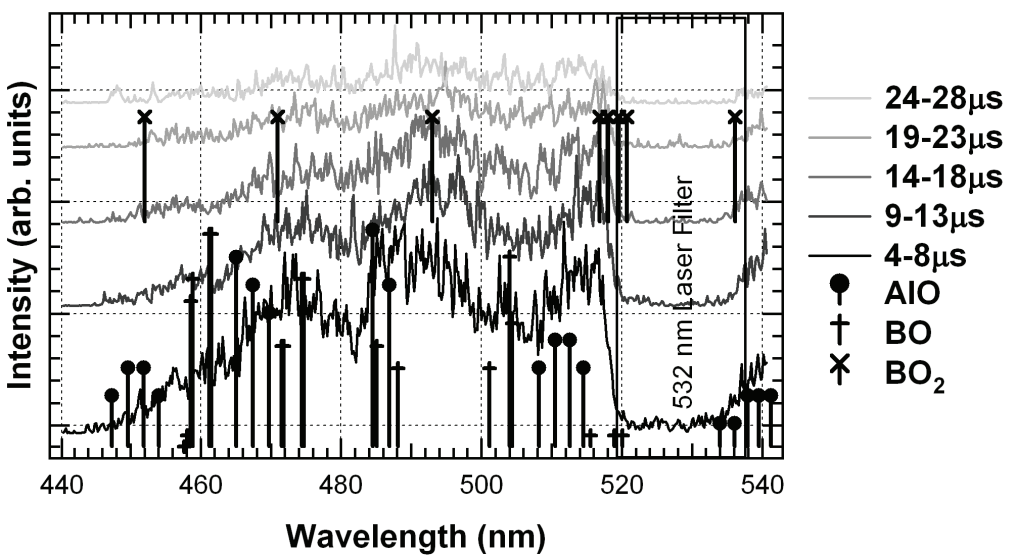

Figure 5 *Results of the laser initiation of Al + B_2O_3*

Table 1 *AlO appearance and persistence data from four of the samples studied.*

Sample	1st appearance of AlO (μs)	Final appearance of AlO (μs)
120.5 nm Al	1	41
Al+Fe_2O_3 (Zachariah)	4	37
Al+Fe_2O_3 (Dreizin)	25	38
Al+MoO_3 (Dreizin)	7	41

peaks of BO_2. The BO_2 peaks appear to increase in intensity and the BO peaks decrease in intensity with time. This suggests that B_2O_3 is not reduced all the way to B, but rather, starts to oxide again after the initial formation of BO. Apparently the oxidation process for boron is competing with that of aluminum.

Discussion

Table 1 shows a comparison of the AlO appearance and persistence for four of the samples from this study. The Al + B_2O_3 sample is not included because the competing boron oxide signals make it difficult to extract information on the AlO signal by itself. It is important to note that all of these experiments were performed in air. Emission lifetimes would therefore not be limited due to a lack of available oxygen. The significance of the first column relates to the time required for the given material to begin releasing energy from the reaction of aluminum with oxygen. A smaller time in the first column means that the energy will be available earlier. The second column corresponds to the end of energy release due to the formation of AlO. The Al + Fe_2O_3 sample of Zachariah's group showed a slightly delayed AlO emission time as compared to the bare nano Al sample. Most likely there is some time required to break apart the constituents, which contributes to the delay. However, the Dreizin Al + Fe_2O_3 sample shows a significantly different behavior. The time to first appearance of AlO is over 20 μs longer for Dreizin's material. The probable cause for this change comes from the difference in Fe_2O_3 content. It is evident even from visible inspection that the Fe_2O_3 content in Dreizin's sample is much higher than that for Zachariah's. Dreizin's sample has an orange-brown color resulting from excess iron oxide, whereas Zachariah's sample is gray (indicative of the aluminum). The higher Fe_2O_3 content is also illustrated in the persistence of neutral Fe emission in the spectra. For Zachariah's sample the Fe emission is significantly weakened relative to the AlO emission by 9 μs, while for Dreizin's sample some Fe emission persists beyond 30 μs. Such a strong Fe emission may also mask the original appearance of AlO in the spectra, allowing for the possibility that the AlO emission begins at the same time for both samples but the emission intensity for Dreizin's iron signal overwhelms the weaker AlO signal early in the experiment. For both Al + Fe_2O_3 samples it is clear that the Fe_2O_3 breaks apart early in the reaction. This suggests that this oxide can provide a source of oxygen to the aluminum for reaction.

The Al + MoO_3 sample shows an initial appearance time for AlO similar to that of Zachariah's Al + Fe_2O_3 sample. The initial background is higher for the Al + MoO_3 sample, which may mask any possible earlier detection of AlO. Elemental molybdenum appears above the background, which verifies the release of oxygen.

For the Al + B_2O_3 sample, the AlO signal is convoluted with signals arising from the oxidation of boron. While the original B_2O_3 is most likely breaking apart initially, any released boron appears to be oxidizing at a rate comparable to that of aluminum. The various oxide spectral features begin to appear around 4 μs and last until about 30 μs.

Similar experiments have been performed on RDX with this same experimental method, except a backlight was used to track changes in absorption because the reaction products of RDX do not emit in the visible range available in these experiments. A two-stage process was evident in the RDX reactions. The first stage was the formation of dark intermediate products (evidenced by an increase in absorbance). The second stage was the formation of clear gaseous products (evidenced by

a decrease in absorbance). The time to maximum absorbance for reacting RDX should correspond to the end of the primary reaction zone. The time to maximum absorption for RDX is typically only 3 μs. The time for the entire reaction of RDX to reach completion is about 13 μs. Comparing RDX reaction times with those of the samples in Table 1 reveals that only the nano aluminum by itself shows evidence of AlO formation within the time frame of the primary reaction zone of RDX. Zachariah's $Al + Fe_2O_3$ is close to being within this zone at 4 μs, followed by Dreizin's $Al + MoO_3$ (7 μs). However all of the samples in Table 1, with the exception of Dreizin's $Al+Fe_2O_3$, would be able to contribute energy from AlO formation to the late time (gaseous) reaction of RDX.

Conclusion

This study reports on the kinetic and chemical processes occurring after the laser initiation in air of 120.5 nm Al, $Al + Fe_2O_3$, $Al + MoO_3$, and $Al + B_2O_3$. All of the samples display spectral features resulting from the combustion of aluminum. AlO emission appears earliest and persists the longest for the nano aluminum sample. The $Al + Fe_2O_3$ and $Al + MoO_3$ samples both show emission from the neutral metals of the original oxide (Fe and Mo, respectively) first, followed by the appearance of AlO. This suggests that the metal oxide is breaking down, which provides oxygen for resulting aluminum combustion. However, in these experiments excess oxygen was available from the surrounding air as well. The $Al + B_2O_3$ showed some evidence for AlO emission, but the AlO spectral features were overlapping and competing with those of BO and BO_2.

Acknowledgements

The authors would like to thank Michael Zachariah, Edward Dreizin and Jan Puszynski for preparing the samples used in this study.

References

1 P. Brousseau and C. J. Anderson, "Nanometric Aluminum", *Propellants, Explosives, Pyrotechnics*, vol. 27, 2002, p. 300.

2 R. W. Armstrong, B. Baschung, D. W. Booth and M. Samirant, "Enhanced Propellant Combustion with Nanoparticles", *Nano Letters*, vol. 3, 2003, p. 253.

3 D. S. Moore, S. F. Son, and B. W. Asay, "Time-Resolved Spectral Emission of Deflagrating Nano-Al and Nano-MoO_3 Metastable Interstitial Composites", *Propellants, Explosives, Pyrotechnics*, vol. 29, 2004, p. 106.

4 S. Wang, Y. Yang, Z. Sun, and D. D. Dlott, "Fast Spectroscopy of Energy Release in Nanometric Explosives", *Chemical Physics Letters*, vol. 368, 2003, p. 189.

5 NIST Atomic Spectra Database (http://physics.nist.gov/cgi-bin/AtData/main_asd)

6 R. W. B. Pearse and A. G Gaydon, *The Identification of Molecular Spectra*, University Printing House, Cambridge 1976.

7 M. Schoenitz, T. Ward and E. L. Dreizin, "Preparation of Energetic Metastable Nano-Composite Materials by Arrested Reactive Milling", *Materials Research Society Proceedings*, vol. 800, 2004, pp. AA2.6.1–AA2.6.6.

8 A. Prakash, A. V. McCormick and M. R. Zachariah, "Aero-Sol-Gel Synthesis of Nanoporous Iron-Oxide Particles: A Potential Oxidizer for Nanoenergetic Materials", *Chemistry of Materials*, vol. 16, 2004, p. 1466.

9 J. A. Puszynski, "Advances in the Formation of Metal and Ceramic Nanopowders", in *Powder Materials: Current Research and Industrial Practices*, Eds. E. V. Barrera, F. D. S Marquis and N. N. Thadhani, TMS Current Research and Industrial Practices, TMS, 2001.

New Approaches to Model Pyrotechnic Reactions

Stefan Kelzenberg, Norbert Eisenreich and Volker Weiser
Fraunhofer Institut für Chemische Technologie, Joseph-von-Fraunhofer-Str. 7, D-76327 Pfinztal, Germany

Abstract: *In most cases pyrotechnic mixtures are constituted from granular components. A theoretical study of such a granular system describes the temperature and concentration evolution in the energetic material by using hot spots as source terms for temperature and particles. The progress of the reaction is mainly influenced by particle properties which are size, melting and evaporation, gasification and surface reactions. In a first step the influence of the particle size ratio between fuel and oxidizer particles is investigated.*

Keywords: *hot-spot model, combustion, ignition, pyrotechnics, Green's method*

Introduction

The work presented in this paper is part of some ongoing efforts to model combustion and ignition processes of propellants and pyrotechnics.[2–7] The aim of this work is not a perfect simulation of a certain process but to investigate single effects and their consequences on a system and the method applied is to make parameter studies resulting in a better understanding of the principal combustion mechanism. For a parameter study it is necessary to perform a greater number of calculations. Therefore models and codes are needed which are fast enough to do this in a reasonable time. As a consequence the models have a reduced complexity but high performance. This paper concentrates on a model, which is called Hot-Spot Model.

Model Description

From a physical point of view combustion processes are mainly dealing with heat transfer: it means heat is generated and consumed by different processes at different locations. Pyrotechnics are usually solid materials. Therefore the model description starts with the partial differential equation of heat transfer in a solid, where convective effects can be neglected (equation 1, below).

$$\frac{\partial T\left[\vec{x},t\right]}{\partial t}-\frac{\lambda}{\rho\, c_p}\cdot\Delta T\left[\vec{x},t\right]=\frac{\dot{Q}\left[\vec{x},t\right]}{\rho\, c_p} \qquad (1)$$

There are several analytical and numerical methods to solve the differential equation. Here Green's method[1] is chosen because, if the appropriate Green's function for the homogeneous problem is known, it only has to be integrated with the source term of the differential (equation 2, below).

$$T\left[\vec{x},t\right]=\int G_U\left[\vec{x}-\vec{x}',t-t'\right]\cdot\frac{\dot{Q}\left[\vec{x},t\right]}{\rho\, c_p}\cdot d\vec{x}'\cdot dt'$$

The Green's function for the above differential equation in three dimensions is a Gaussian-like function (equation 3, below).

$$G_U\left[\vec{x}-\vec{x}',t-t'\right]=\left(\frac{\rho\, c_p}{4\pi\lambda\left(t-t'\right)}\right)^{3/2}\cdot e^{-\frac{\rho c_p(\vec{x}-\vec{x}')^2}{4\lambda(t-t')}}$$

The great advantage of this method is that numerical integration is a much faster and a much more stable process than differentiation.

The next step is to choose the source terms. Two types of heat sources may be considered. One is the combustion enthalpy of the chemical reaction of the material. The simplest reaction is of 0th order described by an Arrhenius term.

$$\dot{Q}_{reac}=q_{reac}Z\cdot e^{-\frac{E}{RT}} \qquad (4)$$

The other one is the ignition energy which is introduced in the system at a certain moment to start a reaction. This is the hot spot and it can be described by a Gaussian function or a Dirac delta function (equation 5, overleaf).

If there are only hot spots, integration can be done analytically. But this is not possible with the Arrhenius term for the chemical reaction. Therefore numerical integration is needed. The algorithm used for this purpose mainly consists of three steps. The first step is to generate an initial temperature profile resulting from the initially

$$\dot{Q}_{hs}[\vec{x},t] = \frac{Q_0}{(2\pi)^{3/2}\sigma_x\sigma_y\sigma_z} \cdot e^{-\left(\frac{(x-x_0)^2}{2\sigma_x^2}+\frac{(y-y_0)^2}{2\sigma_y^2}+\frac{(z-z_0)^2}{2\sigma_z^2}\right)} \cdot \delta[t-t_0] \tag{5}$$

$$T_1[\vec{x},t] = \sum_{i=1}^{n}\left(\frac{Q_0}{\rho c_p (2\pi)^{3/2}\sigma_x\sigma_y\sigma_z} \cdot e^{-\left(\frac{(x'-x_i)^2}{2\sigma_x^2}+\frac{(y'-y_i)^2}{2\sigma_y^2}+\frac{(z'-z_i)^2}{2\sigma_z^2}\right)}\right) \cdot \delta[t'-t] \tag{6}$$

$$T_2[\vec{x},t] = T_1[\vec{x},t] + \frac{q_{reac} \cdot Z}{\rho c_p} \cdot e^{-\frac{E}{R(T_1[\vec{x},t]+T_0)}} \cdot \Delta t \tag{7}$$

$$T_3[\vec{x},t] = \int\left(\frac{\rho c_p}{4\pi\lambda\Delta t}\right)^{3/2} \cdot e^{-\frac{\rho c_p(\vec{x}-\vec{x}')^2}{4\lambda\Delta t}} \cdot T_2[\vec{x},t] \cdot dx'dy'dz' \tag{8}$$

given hot spots (equation 6).

In the second step the progress of the chemical reaction for a small time step Δt is calculated (equation 7). The third step is to calculate the heat diffusion for the same time step Δt by integrating the convolution of the temperature profile and the Green's function (equation 8).

Steps 2 and 3 are repeated for every time step. Step 1 can be included as often as new hot spots occur.

From the above description the following features can be mentioned: the model is a transient one and it describes the heat generation by a chemical

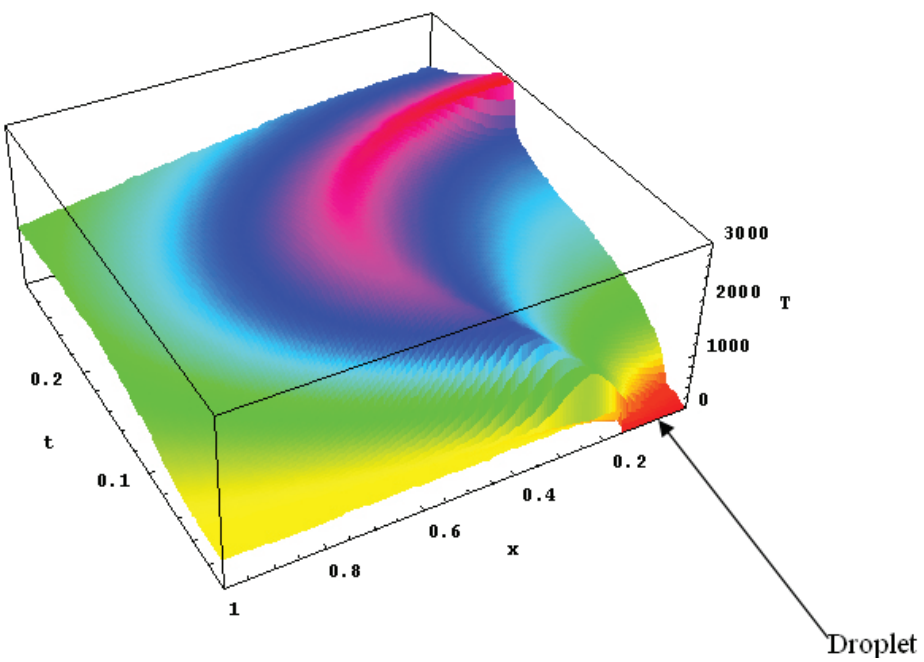

Figure 1 *Temperature profile for a burning particle at the right corner.*

reaction and the heat transport by conduction.

Fuel and oxidizer particles as sources of matter can also be described as hot spots. Including diffusion they can react as soon as gaseous fuel and oxidizer come into contact. The model does not include any convection or radiation. Implementing the model into computer code, we developed several versions of the model for different purposes. One version includes phase transition.

To run the program three types of parameters are necessary:

- Different spatial and temporal distributions of hot spots: energy, size and number of hot spots
- Material parameters: density, heat capacity, heat conductivity, diffusion coefficient
- Reaction parameters: maximum temperature, Arrhenius-parameters (frequency factor and activation energy)

The calculations result in two-dimensional temperature and concentration profiles for every time step, and in heat output, pressure and chemical rate over time.

Results

Single particle combustion

First implementation is a one-dimensional version of the model. It describes a single particle in a reactive atmosphere. As spherical symmetry is assumed one spatial dimension is enough to describe evaporation or gasification of the particle and succeeding combustion. The phase transition at the particle surface is implemented as an artificial high concentration. No heat transfer to the interior of the particle is included. Although these are very strong simplifications there are some interesting results.

Figure 1 gives the temperature profiles in a 3 D plot. The front edge is the spatial axis and the left side is the time axis. The evaporating particle is placed at the lower right corner. As no heat transfer into the particle is included its temperature is set to zero. The surrounding gaseous oxidizer has a temperature of 500 K that is enough to evaporate a small portion of the particle and to start the reaction. In this Figure the evaporation ends when temperature reaches the time axis on the right side. The flame is marked by the region of the highest

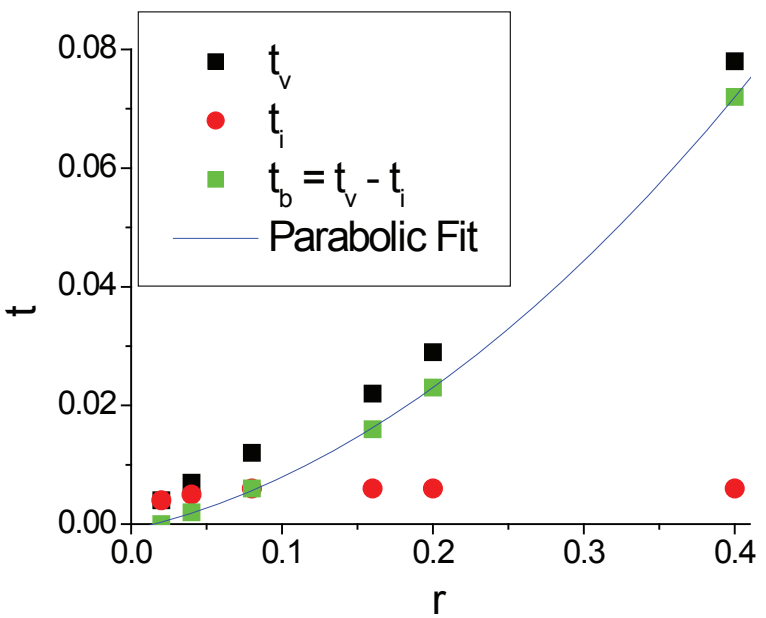

Figure 2 *Burning time $t_b = t_v - t_i$ vs. initial radius and parabolic fit.*

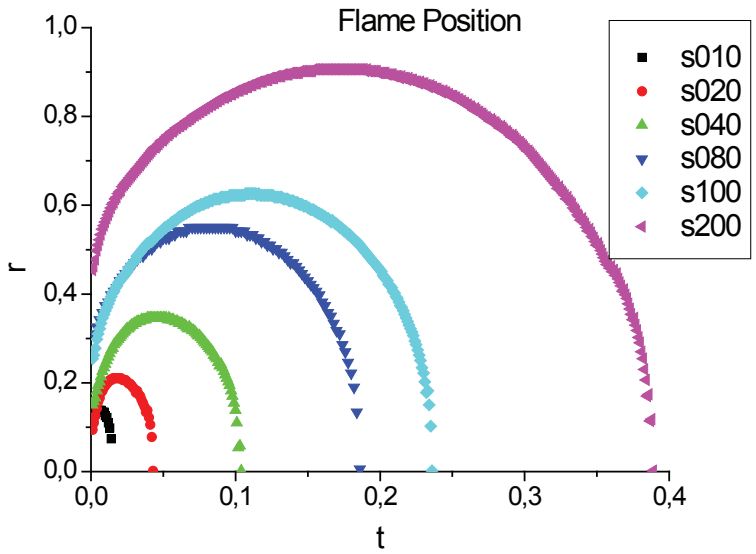

Figure 3 *Flame position as location of the highest temperature vs. time.*

temperature.

Calculations with different initial radii leads to corresponding evaporation times t_v for the particles. If ignition time t_i is defined as the time to reach the flame temperature then the burning time $t_b = t_v - t_i$ can be fitted by a parabolic function (Figure 2). This is well known as the r^2-law from theory[8] as expressed in equation 9, overleaf.

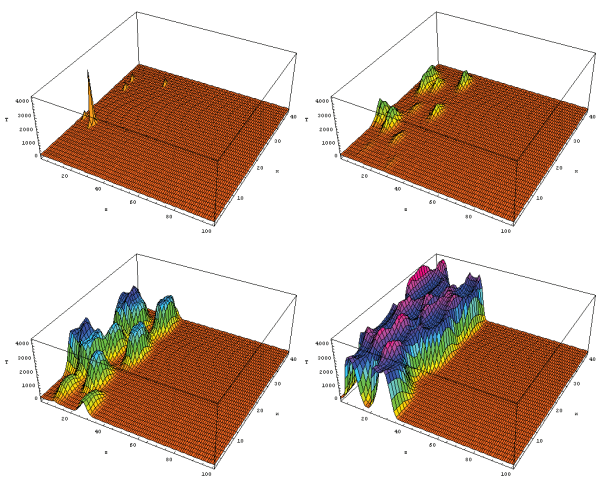

Figure 4 *Series of temperature profiles for ignition with hot particles.*

$$t_b = \frac{\rho_l \cdot c_{pg} \cdot r^2}{2 \cdot \lambda_g \cdot \ln(B+1)} \qquad (9)$$

On the other hand if the flame position as the location of the highest temperature is taken from the same calculations Figure 3 results. As can be seen the flame moves with time. There is no constant distance to the particle surface and the flame exists much longer than the particle. Simple expressions to describe these findings like the r^2-law can not be found in theory, but measurements on burning droplets show a similar behavior.[9]

Ignition with hot particles

For the investigation of ignition processes with hot particles a full three-dimensional version was developed. A reactive material is hit by hot particles which are used as heat sources to start the chemical reaction of the reactive material. Figure 4 displays a short series of temperature profiles. From left to right it shows the initial state when the particles hit the reactive material. Then the heat spread and chemical reaction of the material produces additional heat. Finally a closed reaction front is formed.

The amount of heat produced and the resulting temperature can be used as a measure for the

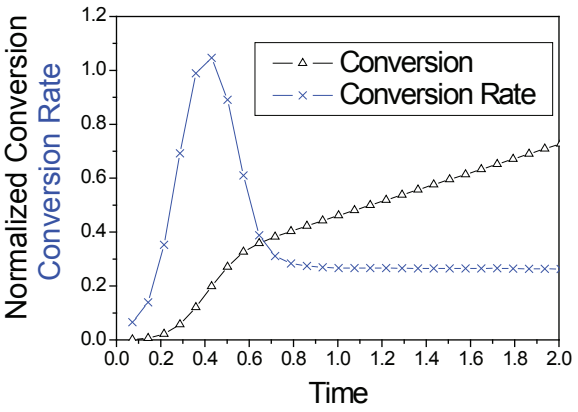

Figure 5 *Normalized conversion and conversion rate during ignition with hot particles.*

progress of the reaction. In Figure 5 it is called normalized conversion. The time derivation of this quantity is the conversion rate. The peak at the beginning of the curve of the conversion rate results from the fact that at the beginning every particle has its own reactive sphere. Later these spheres overlap and the total reactive area reduces (see Figure 4). Then the reaction of the material goes to a steady state burning.

Reacting particles

In most cases pyrotechnic mixtures are constituted from granular components, *i.e.* fuel and oxidizer are reactive particles. In the framework of this model they can be described as sources of material which then react and produce heat. In addition to the temperature concentration profiles are

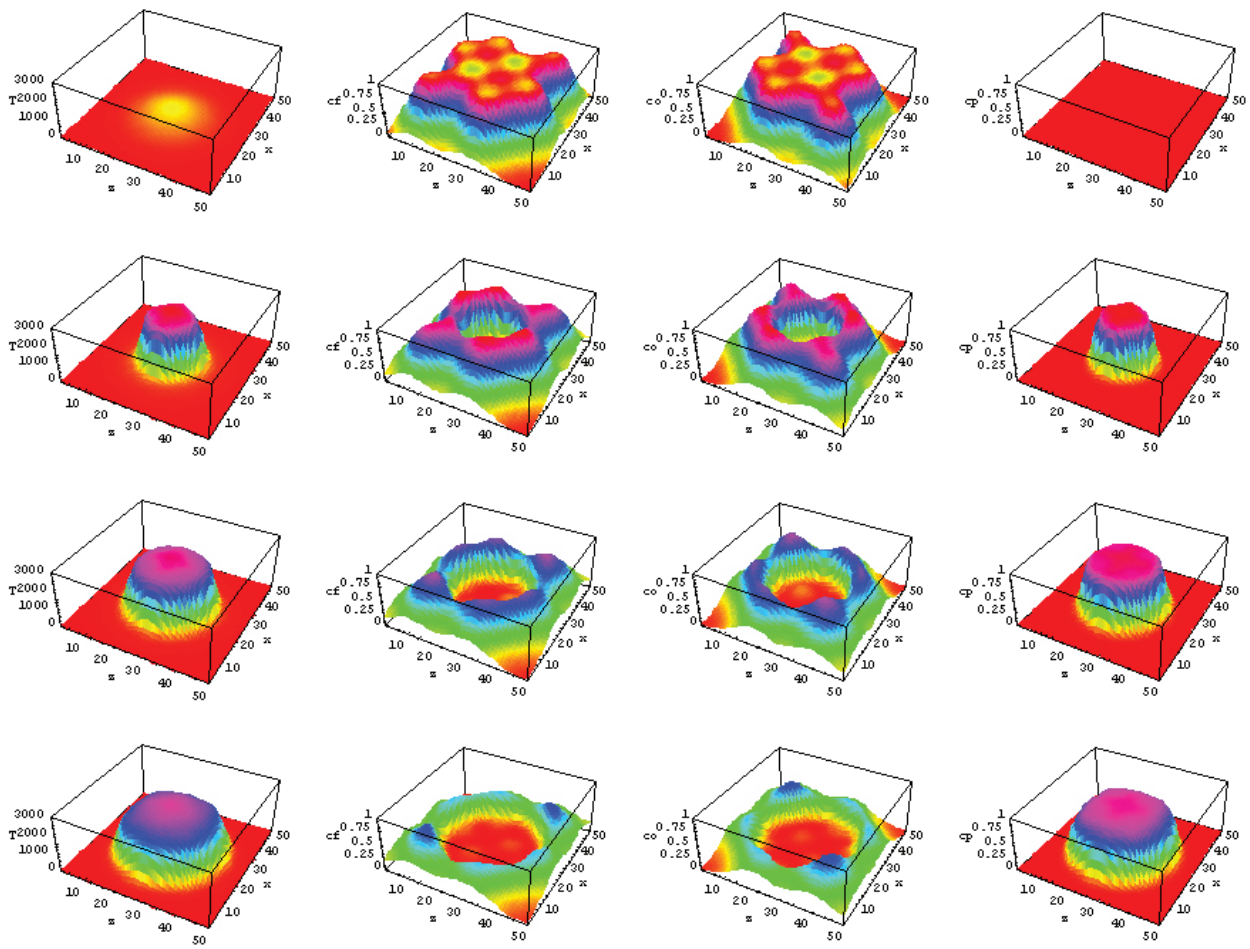

Figure 6 *Temperature and concentration profiles for eight fuel and eight oxidiser particles of same size. A thermal hot spot at the center ignites the material. From left to right: temperature, fuel concentration, oxidiser concentration, product concentration.*

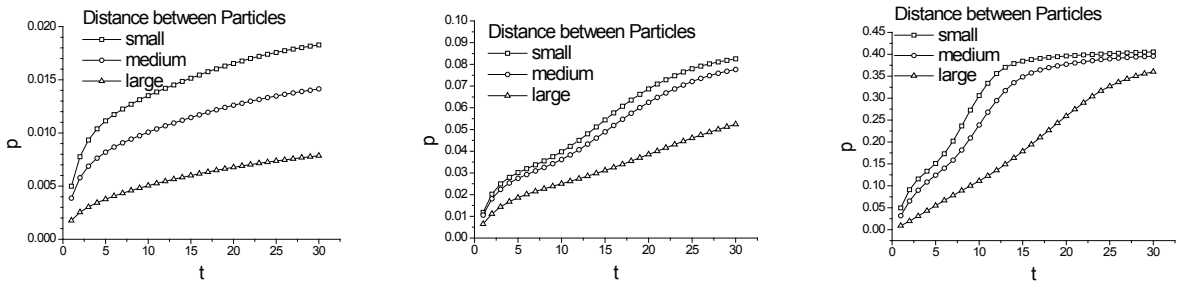

Figure 7 *Conversion for 1, 2 and 8 particles of fuel and oxidizer of same size (from left to right) and different distances between the particles.*

calculated. Figure 6 gives a short series of profiles for temperature, fuel concentration, oxidizer concentration and product concen-tration. The reaction of the particles is started by a thermal hot spot in the center.

For the results displayed in Figure 7 the number of particles and the distance between the particles were varied. The size was the same for all particles. As expected the best burn out is achieved for the smallest distance between the particles. For more than one particle there is a step in the curve.

Usually the particles of the oxidizer and the fuel are

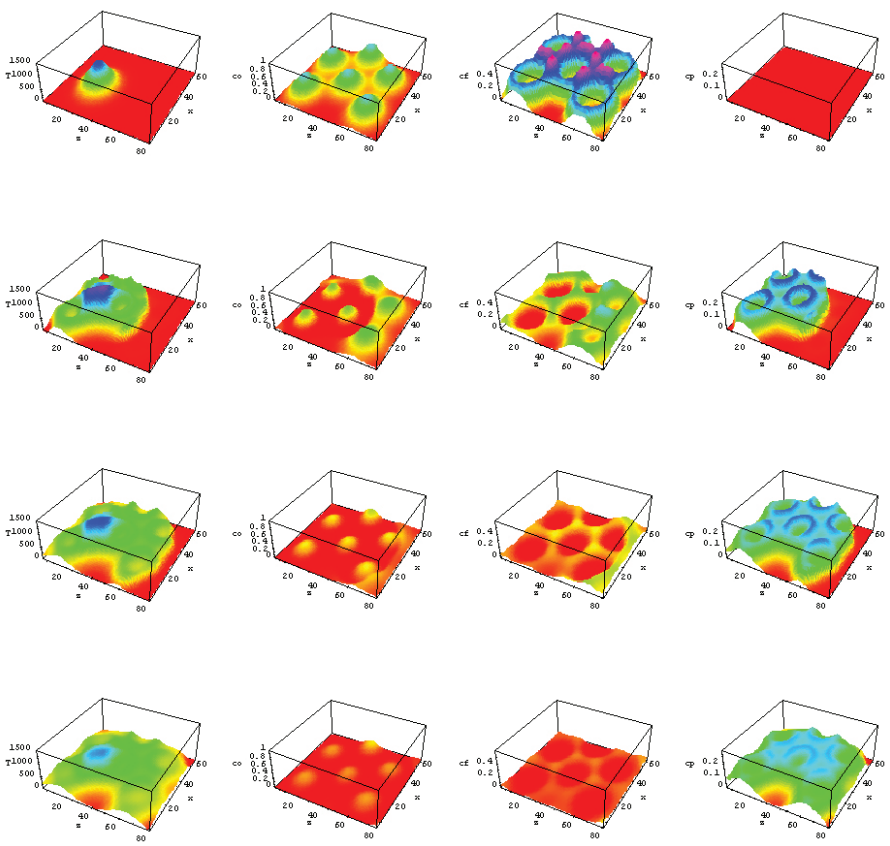

Figure 8 *Temperature and concentration profiles for fuel and oxidizer particles of different size. A thermal hot spot ignites the particles. From left to right: temperature, oxidizer concentration, fuel concentration, product concentration.*

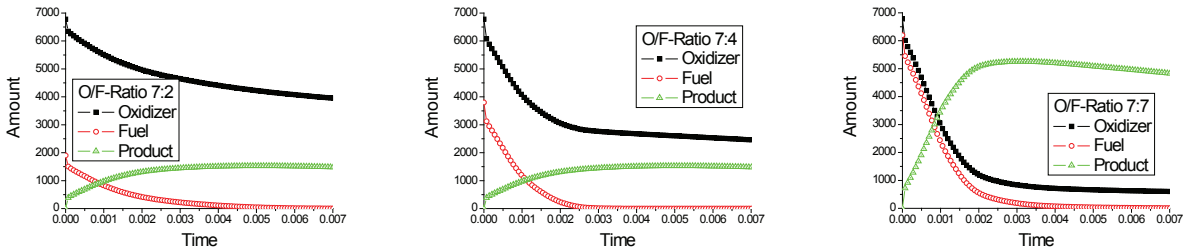

Figure 9 *Amount of oxidizer, fuel and product for different O/F-ratios vs. time (from left to right: 7:2, 7:4. 7:7)*

of different size. Figure 8 shows an example with a series of temperature and concentration profiles where large oxidizer particles are surrounded by smaller fuel particles.

Varying the initial amount of fuel leads to different oxidizer-fuel ratios. Figure 9 gives the curves of the total amount of oxidizer, fuel and product *vs*. time for three different O/F ratios. The best O/F ratio depends on the type of the chemical reaction.

In Figure 10 the heat output of the reaction is given dependent on the energy of the initial thermal hot spot. As can be seen the influence of this parameter is less important if the energy is high enough to start the reaction.

Conclusion

As the examples show the hot-spot model is a useful tool to make parameter studies. Parameters that can be varied are number, size and distribution of particles and some material properties (c_p, λ, ρ, D). Simple chemistry is included. The computer code runs fast and is very stable because there is no need to calculate derivations numerically. Further steps will be to include phase change also in the 3 D version and more complex chemistry. After validation a lot of calculations have to be done studying the influence of the different parameters.

References

1 H. S. Carslaw and J. C. Jaeger, *Conduction of Heat in Solids*, Clarendon Press, Oxford, 1973.

2 S. Kelzenberg, N. Eisenreich, T. Fischer and

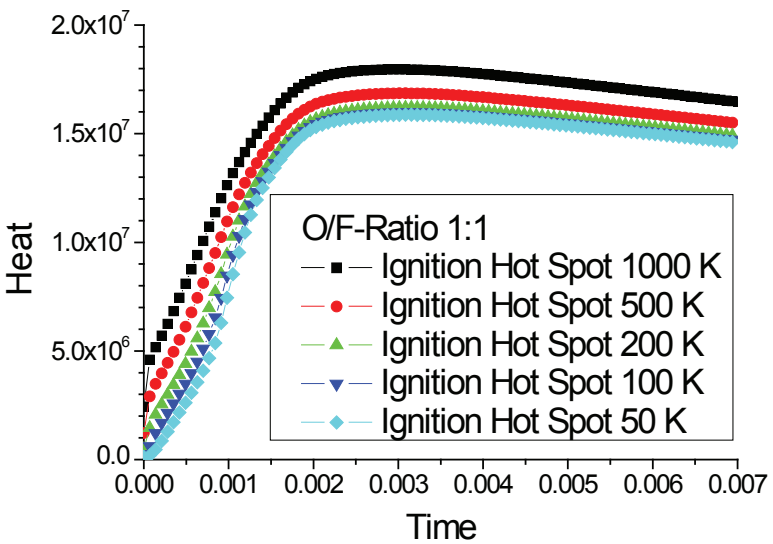

Figure 10 *Heat output for varying ignition energy.*

A. Kolezcko, “Verbrennungsmodellierung mit Hot Spots”, 32nd International Annual Conference of ICT, Karlsruhe, Germany, July 3–6, 2001, P165.

3 V. Weiser, S. Kelzenberg and N. Eisenreich, “Influence of the Metal Particle Size on the Ignition of Energetic Materials”, *Propellants, Explosives, Pyrotechnics*, vol. 28, 2001, p. 284.

4 T. Fischer, G. Langer and N. Eisenreich, “Burning Rate Models of Gun Propellants”, European Forum on Ballistics of Projectiles, EFBP’2000, Saint-Louis, France, April 11–14, 2000, pp. 117-127.

5 F. Schedlbauer, A. Meßmer, U. Steffens and I. Reuter, “Combustible Cases for RMK 30”, 29th International Annual Conference of ICT, Karlsruhe, Germany, June 30–July 3, 1998, P103.

6 C. A. van Driel, J. Kobes and R. Broekhuis, “Characterisation of Porous Single Base Propellant”, 34th International Annual Conference of ICT, Karlsruhe, Germany, June 24−27, 1998, P112.

7 S. Kelzenberg, N. Eisenreich and V. Weiser, “Fast Methods on Modelling of Multidimensional Distributions of Evaporating and Burning Droplets”, 34th International Annual Conference of ICT, Karlsruhe, Germany, June 24–27, 2003, V26.

8 A. Williams, *The Combustion of Liquid Fuel Sprays*, Butterworth & Co Ltd, London, 1990.

9 V. Weiser, S. Gläser, S. Kelzenberg, N. Eisenreich and E. Roth, “Investigations on the Droplet Combustion of Gelled Mono- and Bipropellants”, 41st AIAA/ASME/ SAE/ASEE Joint Propulsion Conference & Exhibit, 10−13 July 2005; Tucson, Arizona; AIAA-2005-4474, pp. 1−9

10 M. E. Brown, S. J. Taylor and M. J. Tribelhorn, “Fuel-Oxidant Particle Contact in Binary Pyrotechnic Reactions”, *Propellants, Explosives, Pyrotechnics*, vol. 23, 1998, p. 320.

Errata

The following errors in previous editions of the Journal of Pyrotechnics have been communicated to us. We apologise for any inconvenience or confusion caused.

Issue and Page	Incorrect text	Corrected text
Issue 22 - Sponsors details - PyroShows	email and web address	email: info@pyroshowsusa.com web: www.pyroshowsusa.com
Issue 22 - Page 40, right column, 2nd paragraph 4th line	Mis-spelling of “hydrrogen”	Correct spelling to “hydrogen”

Events Calendar

Pyrotechnics and Fireworks

33rd International Pyrotechnics Seminar
July 16 - 21 2006, Fort Collins. CO, USA
Contact: Linda Reese, Appl. Res. Assoc. Inc.
10720 Bradford Road., Ste 110
Littleton, CO 80127, USA
Phone: +1-303-795-8106
Fax: +1-303-795-8159
email: lreese@ara.com
web: http://www.ips.org http://www.ipsusa.org

Pyrotechnics Guild Int'l Convention
August, 2006, Appleton, WI, USA
Contact: Frank Kuberry, Sec. Treas.
304 W Main St
Titusville, PA 16354, USA
Phone: +1-814-827-6804
email: kuberry@earthlink.net
web: http://www.pgi.org

Listing of Fireworks Events - Worldwide
web: http://fireworksguide.com

Pyrotechnic Chemistry Lecture Course
18/19/20 September 2006
Huntingdon, Cambs. UK
For more information please see
web: http://www.pyrochemistry.net

Propulsion

42nd AIAA/ASME/SAE/ASEE Joint Propulsion Conference
9 - 12 Jul 2006
Sacramento, California
Contact:
Phone: +1-703-264-7500
web: http://www.aiaa.org

High Power Rocketry

LDRS 2006
Contact: see web site
web: http://www.tripoli.org/calendar.htm

Model Rocketry

NARAM 2006
Contact:
web: http://www.naram.org
For other launch information visit the NAR Web site: http://www.nar.org

Energetic Materials

Fourth International Disposal Conference
13 - 14 November 2006 Katrineholm, Sweden
Contact: Klas Nyberg, KCEM,
Gammelbackavagen 6 SE-691 51 Karlskoga, Sweden
Phone: +46 586 847 45
Fax: +46 586 847 49
E-mail: klas.nyberg@kcem.se

Future Events Information

If you have information concerning future explosive, pyrotechnics or rocketry meetings, training courses or other events that you would like to have published in the Journal of Pyrotechnics and on the website http://www.jpyro.com - please provide the following information: Name of event, Date and place (City, State, Country), Contact information - including, if possible, name of contact person, postal address, telephone and fax numbers, email address and website

Journal of Pyrotechnics - Sponsors

Journal of Pyrotechnics wishes to thank the following sponsors for their continuing support

Individual Sponsors

Ed Brown
PO Box 177
Rockvale, CO, 81244, USA
phone: 719-784-4226
email: edwinde@cs.com

Gerald Laib
17611 Longview Lane
Olney, MD 20832, USA
phone: 301-744-4358
fax: 301-744-4784

Corporate Sponsors

Aerotech & Industrial Solid Propulsion Inc.
Gary Rosenfield
2113 W 850 N St
Cedr City, UT 84720, USA
phone: 435-867-9998
fax: 435-865-7120
email: garyr@powernet.net
web: http://www.aerotech-rocketry.com

Allied Speciality Insurance
Rick D'Aprile
10451 Gulf Blvd.
Treasure Island, FL 33706, USA
phone: 800-237-3355
fax: 727-367-1407
email: info@alliedspeiality.com
web: http://www.alliedspeciality.com

American Fireworks News
Jack Drewes
HC 67 Box 30
Dingmans Ferry, PA 18328, USA
phone: 570-828-8417
fax: 570-828-8695
email: afn@fireworksnews.com
web: http://www.fireworksnews.com

American Pyrotechnics Association
Julie Heckman
4808 Moorland Lane - Ste 109
Bethusda, MD 20814, USA
phone: 301-907-8181
fax: 301-907-9148
email: jheckman@americanpyro.com
web: http://www.americanpyro.com

Astro Pyrotechnics
Leo Autote
2298 W Stonehurst
Rialto, CA 92377, USA
phone: 909-822-6389
fax: 909-854-4747
web: http://www.astropyro.com

Black Cat Fireworks
Martin Guest
Crossland Hill, Huddersfield, W Yorkshire
HD7 7AD, UK
phone: +44-1484-640640
fax: +44-1484-485943
email: marting@blackcatfireworks.ltd.uk
web: http://www.blackcatfireworks.ltd.uk

Brooke * Mawhorr, PC
Douglass K Mawhorr
112 East Gilbert St., PO Box 1071
Muncie, IN 47305, USA
phone: 765-741-1375
fax: 765-288-7763
email: dimmawhorr@aol.com

Canadian Explosives Research Laboratory
Dr Phil Lightfoot, Manager
CANMET - 555 Booth St.
Ottawa, ON K1A 0G1, Canada
phone: 613-947-7533
fax: 613-995-1230
email: plightfo@nrcan.gc.ca
web: http://www.nrcan.gc.ca/mms/cerl

Combined Specialities International Inc.
John & Alice Allen
8362 Tamarack Village, Ste. 119
Woodbury, MN 55125, USA
phone: 651-855-0091
fax: 651-855-0088
email: jallen@combinedspecialities.com

Davas Ltd
Tom Smith
8 Aragon Place, Kimbolton, Huntingdon
Cambs. UK. PE28 0JD
phone: +44 1480 860124
fax: +44 1480 861125
email: toms@davas.co.uk
web: http://www.davas.co.uk

Delcor Industries Inc
Sam Bases
19 Standish Ave.
Yonkers, NY 10710, USA
phone: 914-779-6425
fax: 914-779-6463
email: delcor@hotmail.com
web: http://www.delcor.com

European Pyrotechnic Arts Newsletter
Rob Driessen
Grenadierweg 55
Riemst, B 3770, Belgium
phone: +32-12-210-630
fax: +32-12-210-630
email: epan@pandora.be
web: htp://users.pandora.be/epan

Fawkes Fireworks
Tony Cardell & David Watts
89 Lingfield Road
Edenbridge, Kent TN8 5DY, UK
phone: +44-1732-862-862
fax: +44-1342-317-818
email: tony@fawkes.co.uk
web: http://www.fawkes.co.uk

Fire One
Dan Barker
863 benner Pike
State College, PA 16801, USA
phone: 814-238-5334
fax: 814-231-0799
email: info@fireone.com
web: http://www.fireone.com

Firefox Enterprises Inc.
Gary Purrington
11612 N Nelson
Pocatello, ID 83202, USA
phone: 208-237-1976
fax: 208-237-1976
email: custserv@firefox-fx.com
web: http://www.firefox-fx.com

Firework Professionals
Anthony Leyland
PO Box 19-912
Christchurch, 8030, New Zealand
phone: +64-3-982-3473
fax: +64-3-982-3474
email: firework@firework.co.nz
web: http://firework.co.nz

Fireworks
PO Box 40
Bexhill, Sussex TN40 1GX, UK
phone: +44-1424-733-050
fax: +44-1424-733-050
email: editor@fireworks-mag.org
web: http://www.fireworks-mag.org

Fireworks and Stage FX America
Kevin Brueckner
PO Box 488
Lakeside, CA 92040, USA
phone: 619-938-8277
fax: 619-938-8273
email: info@fireworksamerica.com
web: http://www.fireworksamerica.com

Fireworks Business
Jack Drewes
HC 67 Box 30
Dingmans Ferry, PA 18328, USA
phone: 717-828-8417
fax: 717-828-8695
email: afn@fireworksnews.com
web: http://www.fireworksnews.com

Fireworks by Grucci
Phil Grucci
1 Grucci Lane
Brookhaven, NY 11719, USA
phone: 631-286-0088
fax: 631-286-9036
email: philgrucci@aol.com
web: http://grucci.com

Fullam's Fireworks Inc
Rick Fullam
PO Box 1808 CVSR
Moab, UT 84532, USA
phone: 435-259-2666
email: rfullam_3@yahoo.com

Goex Inc.
Mick Fahringer
PO Box 659
Doyline, LA 71023, USA
phone: 318-382-9300
fax: 318-382-9303
email: email@goexpowder.com
web: http://www.goexpowder.com

High Power Rocketry
Bruce Kelly
PO Box 970009
Orem, UT 84097, USA
phone: 801-225-3250
fax: 801-225-9307
email: tra00015@aol.com
web: http://tripoli.org

IPON srl
Pagano Benito
Via Trofa
Ottavino, Napoli 80044, Italy
phone: +39-81-827-0934
fax: +39-81-827-0026
email: info@ipon.it
web: http://www.ipon.it

Island Fireworks Co. Inc.
Charles Gardas
N735 825th St
Hager City, WI 54014, USA
phone: 715-792-2283
fax: 715-7922640
email: islndfwk@pressenter.com
web: http://www.island-fireworks.com

Lantis Fireworks & Lasers
Ken Lantis
PO Box 491
Draper, UT 84020, USA
phone: 801-768-2255
fax: 801-768-2433
email: info@fireworks-lasers.com
web: http://www.fiireworks-lasers.com

MagicFire Inc
Paul McKinley
PO Box 896
Natick, MA 01760, USA
phone: 508-647-9645
fax: 508-647-9646
email: pyrotech@magicfire.com
web: http://www.magicfire.com

Martin-Baker Aircraft Ltd
David Chapman
Lower Rd, Higher Denham
Uxbridge, Middlesex UB9 5AJ
Great Britain
Phone: 44-1895-836-644
FAX: 44-1985-836-686
email: dchapman@martin-baker.co.uk
web: www.martin-baker.com

Martinez Specialities
Phil Martinez
208 Bossard Rd
Groton, NY 13073, USA
phone: 607-898-3053
fax: 607-898-3952
email: mr.squib@clarityconnect.com

Maratamaya Ogatsu Fireworks Co. Ltd.
1-35-35 Oshitate Fuchu
Tokyo, 183-0012, Japan
phone: +81 42-363-6251
fax: +81-42-363-6252
email: hanabi@mof.co.jp
web: http://www.mof.co.jp

Mighty Mite Marketing
Charlie Weeth
122 S 17th St
LaCrosse, WI 54601, USA
phone: 608-784-3212
fax: 608-782-2822
email: czweeth@pyro-pages.com
web: http://www.pyro-pages.com

MP Associates Inc.
PO Box 546
Ione, CA 94640, USA
phone: 209-274-4715
fax: 209-274-4843

Nilsson & Lee Pyrotechnics
Hans Nillson
Box 130
SE-372 22 Ronneby, Sweden
phone: +46-457-15600
email: info@pyrokits.com
web: http://www.pyrokits.com

Nitrotech Australia Pty. Ltd.
Chris Larkin
PO Box 349
Mount Isa, QLD 4825, Australia
phone: 617-47-44-2290
fax: 617-47-44-3998
email: nitrotech@smartchat.net.au

Precocious Pyrotechnics Inc.
Garry Hanson
4420 278th Ave NW
Belgrade, MN 56312, USA
phone: 320-346-2201
fax: 320-346-2403
email: ppinc@tds.net
web: http://www.pyro-pro.com

Pyro Shows Inc.
Lansden Hill
PO Box 1406
LaFollette, TN 37766, USA
phone: 800-662-1331
fax: 423-562-9171
email: info@pyroshowsusa.com
web: http://pyroshowsusa.com

Pyrodigital Consultants
Ken Nixon
1074 Wranglers Trail
Pebble Beach, CA 93953, USA
phone: 831-375-9489
fax: 831-375-5255
email: purodig@aol.com
web: http://www.infinityvisions.com/pyrodigital

PyroLabs Inc.
Ken Kosanke
1775 Blair Road
Whitewater, CO 81527, USA
phone: 970-245-0692
fax: 970-245-0692
email: ken@jpyro.com

RCS Rocket Motor Components Inc.
Gary Rosenfield
2113 W 850 N St
Cedar City, UT 84720, USA
phone: 435-865-7100
fax: 435-865-7120
email: garyr@powernet.net
web: http://www.rocketmotorparts.com

RES Speciality Pyrotechnics
Steve Coman
21595 286th St
Belle Plaine, MN 56011, USA
phone: 952-873-3113
fax: 952-873-2859
email: respyro@earthlink.net
web: http://www.respyro.com

Rozzi Famous Fireworks
Arthur Rozzi
PO Box 5
Loveland, OH 45140, USA
phone: 513-683-0620
fax: 513-683-2043
email: art@rozzifireworks.com
web: http://www.rozzifireworks.com

Service Chemical Inc.
Ben Cutler
2651 Penn Avenue
Hatfield, PA 19440, USA
phone: 215-362-0411
fax: 215-362-2578
email: ben@servicechemical.com
web: http://www.servicechemical.com

Spirit of 76 Fireworks
John Bechtold
6401 West Highway 40
Columbia, MO 65202, USA
phone: 573-477-1776
fax: 573-477-1786
email: marketing@76wholesale.com
web: http://www.76wholesale.com

Starburst Pyrotechnics & Fireworks Displays Ltd
Bonnie Pon
2nd Fl-Sui Hing Hong Bldg-17, Commissioner St
Johannesburg, Gauteng 2000, South Africa
phone: +27-11-838-7705
fax: +27-11-836-6836
email: info@starburstpyro.co.za
web: http://www.starburstpyro.co.za

Western Pyrotechnics Inc.
Rudy Schaffner
PO Box 176, Holtville, CA 92250, USA
phone: 760-356-5679
fax: 760-356-2155
email: rudys@holtville.net

Information for Readers

Editorial Policy

Articles accepted for publication in the *Journal of Pyrotechnics* can be on any technical subject in pyrotechnics. However, a strong preference will be given to articles reporting on research (conducted by professional or serious individual experimenters) and to review articles (either at an advanced or tutorial level). Both long and short articles will be gladly accepted. Also, responsible letters commenting on past Journal articles will be published along with responses by the authors.

Publication Frequency

The *Journal of Pyrotechnics* appears approximately twice annually, typically in mid-summer and mid-winter.

Subscriptions

Anyone purchasing a copy of the Journal will be given the opportunity to receive future issues on an approval basis. Any issue not desired may be returned in good condition and nothing will be owed. So long as issues are paid for, future issues will automatically be sent. In the event that no future issues are desired this arrangement can be terminated at any time by informing the publisher. Additional discounts are available for payment in advance for issues of the *Journal of Pyrotechnics*. Please contact the publisher for more information.

Back issues

Back issues of the Journal will be kept in print permanently as reference material. Shortly, these will also be available online by subscription at http://www.jpyro.com

Caution

The experimentation with, and the use of, pyrotechnic materials can be dangerous and may require licences or permits in certain countries; it is felt to be important for the reader to be duly cautioned. Without the proper training and experience no one should ever experiment with or use pyrotechnic materials. Also, the amount of information presented in this Journal is not a substitute for necessary training and experience, nor does it remove the relevant application of national or local laws and regulations.

A major effort has been undertaken to review all articles for correctness. However it is possible that errors remain. It is the responsibility of the reader to verify any information herein before applying that information in situations where death, injury or property damage could result.

Sponsorships

No advertising as such is printed in the *Journal of Pyrotechnics*. However a limited number of sponsors have been sought so that the selling price of the Journal can be reduced from the listed cover price. The costs of being a sponsor for an issue of the *Journal of Pyrotechnics* is $70 per issue for businesses and organisations and $35 for individuals. In addition to a listing in the sponsors section of the Journal, full sponsors receive two free copies of the sponsored journal [one copy for individual sponsors]. Additionally, if you so desire, we will provide a link from the *Journal of Pyrotechnics* website (www.jpyro.com) to the sponsor's website or email address - or simply a company name and contact details. Additionally it is possible to insert a "flyer" for distribution with the Journal on payment of a modest fee. Please contact the publisher or managing editor for more details.